# Petrology and U–Pb geochronology of high-grade meta-volcano-sedimentary rocks from central Xolapa Complex, southern Mexico

Roberto Maldonado, Pedro Corona-Chávez, Luigi Solari, Carlos Ortega-Obregón, Stefano Poli

## Abstract

The Xolapa Complex (XC) is a high-grade metamorphic belt exposed along the southern margin of the North American plate in Mexico. Its evolution includes an episode of widespread anatexis related to crustal thickening and uplift from middle to lower crustal levels during the Paleocene. On the basis of field and petrographic work, this study integrates a petrological modelling approach with zircon and monazite LA-ICP-MS U–Pb geochronology to elucidate the tectonothermal evolution of the central region of this belt. The study area includes a sequence of alternating migmatitic paragneiss and garnet-bearing mafic schist, which is interpreted to represent an Early-Cretaceous (Valanginian–Hauterivian) meta-volcano-sedimentary succession. Petrographic evidence and phase equilibria calculations demonstrate that a staurolite–kyanite grade metamorphism occurred at ~640–670 °C and 8–9 kbar before to widespread migmatization took place. Differential anatexis of fertile and refractory layers occurred progressively via biotite and amphibole dehydration-melting reactions, and continued during peak metamorphism at granulite-facies conditions of ~800–820 °C and ~5–7 kbar. Melt generation/mobilization progressed during cooling until crystallize at ~700 °C, according to Ti-in zircon-thermometry. In order to link U–Pb ages to metamorphic stages, zircon and monazite from different migmatite components were analyzed and chemical fingerprints were used. The age of prograde metamorphism is poorly constrained due to limited preservation of zircon and monazite, but likely occurred during the mid- to Late Cretaceous. Cooling and melt crystallization recorded by leucosome zircon occurred at 61.8±0.6 Ma. Both zircon and low-Y monazite from whole rock and melanosome portions, respectively, are consistent with an episode of growth around 60.9±0.5 Ma, but monazite continued to grow/recrystallize for a period of ca. 10 Ma. Thin Oligocene (~34–26 Ma) zircon and high-Y monazite rims are interpreted to reflect a stage of reheating by magmatic advection related to arc plutonism in the region. The results suggest the affinity of the central XC with other Early-Cretaceous volcano-sedimentary basins of central-southern Mexico. A period of crustal thickening would have buried the sequence at depths of ~30 km, causing Barrovian-type metamorphism during mid- to Late Cretaceous time and, eventually, anatexis that evolved at granulite-facies conditions during orogenic collapse in the Paleocene (≥62 Ma). The time span from leucosome crystallization to late-stage reheating in central XC would imply a protracted high-temperature evolution indicating middle- to upper crust residence time of at least ca. 30 Ma.

**Keywords:** Xolapa Complex; metamorphism–anatexis; migmatite; phase equilibria modelling; U–Pb geochronology

## 1. Introduction

High-temperature (H*T*) metamorphism and anatexis are intimately linked during the evolution of orogenic belts (e.g. Patiño-Douce et al., 1990; Harris and Massey, 1994). Anatexis may occur during crustal thickening and subsequent thermal relaxation or during decompression related to orogenic collapse (e.g. Fitzsimons, 1996; Teyssier and Whitney, 2002; Brown, 2005; Searle et al., 2009). Therefore, understanding the pressure–temperature (*P*–*T*) path of migmatitic terranes, and its relationships in space and time to magmatism and deformation, is crucial for deciphering the implications of partial melting during orogenesis.

Studies in migmatite terranes over the last decade have shown that linking quantitative *P*–*T* estimates (e.g. petrological modelling) with high-spatial resolution geochronology and chemical microanalysis (e.g. LA-ICP-MS) can provide critical insights into the orogenic processes (e.g. Stowell et al., 2010; Regis et al., 2014; Yakymchuk et al., 2015; Rocha et al., 2017). However, this approach has been challenged by the petrological nature of migmatites that makes difficult to relate the obtained isotopic ages (e.g. Taylor et al., 2016) to each specific stage of a commonly complex reaction history (e.g. White et al., 2003; Kriegsman and Álvarez-Valero, 2010; White and Powell, 2010).

The Xolapa Complex (XC) (in the Xolapa Terrane; Campa and Coney, 1983) is a high-grade metamorphic belt that extends along the Pacific coast of southern Mexico and provides a suitable field area to evaluate the timescales of metamorphism, partial melting and crustal residence in the context of an active convergent margin. It has been shown that this belt records process of H*T* metamorphism and partial melting related to crustal thickening and uplift from middle to lower crustal levels (e.g. Herrmann *et al*., 1994; Corona-Chávez et al., 2006). Although a widespread anatectic episode is widely recognized at the Paleocene, recent studies have provided gechronological evidence for not one but likely two further partial melting episodes (e.g. Pérez-Gutiérrez *et al*., 2009; Estrada-Carmona *et al*., 2016; Talavera-Mendoza *et al*., 2013). A long-standing magmatic history with punctuated pulses between Late Jurassic and Miocene (e.g. Solari et al., 2007; Talavera-Mendoza *et al*., 2018) would suggest, in principle, an equally episodic metamorphic evolution. However, the paucity of petrological studies has resulted in a very limited understanding of its metamorphism, and has led, after decades of study, to regional-scale generalizations seeking to reconcile in a ~600 km long belt. Faced with a growing geochronological database, geological mapping and acquisition of *P*–*T*–time (*t*) data in XC has lagged.

In this contribution, we present geological and petrochronological data from the central XC, a region of the belt largely unknown so far. We used a petrological method to identify that metamorphism in this transect includes a staurolite–kyanite grade stage, followed by granulite-facies migmatization and subsequent thermal overprint. Then we integrate these data with zircon and monazite U–Pb dates by LA-ICP-MS to derive a *P*–*T*–*t* path for the central XC. The results demonstrate how this approach can help to understand the timescales and nature of exhumation of thickened continental crust that has undergone anatexis.

## 2. Geological background

The XC represents a portion of middle to lower crust that has been exhumed since the Paleogene along the southern margin of the North American plate in Mexico (Ratschbacher et al., 1991; Herrmann *et al*., 1994). This belt is disposed in a roughly E–W trend (Fig. 1) and is tectonically juxtaposed against the Guerrero, Mixteca and Oaxaquia terranes, of Jurassic–Cretaceous, Paleozoic and Mesoproterozoic ages, respectively (Ortega-Gutiérrez et al., 2018). The boundaries with these terranes are mostly occupied by post-tectonic Cenozoic granitoids, but regional-scale shear zones have been identified at La Venta and Chacalapa regions (Riller *et al*., 1992; Tolson *et al*., 2007; Solari *et al*., 2007). The tectonic trend of the XC is likely controlled by the dynamic of the Acapulco trench, a plate-tectonic boundary governed by processes of crustal detachment and subduction erosion that confer it a truncated margin character (Schaaf *et al*., 1995; Morán-Zenteno *et al*., 1996; Morán-Zenteno *et al*., 2018).

The metamorphic belt consists of variably deformed and migmatized granitoid orthogneiss, amphibolite and aluminous schist, with minor marble, mafic schist, metagabbro and calc-silicate rock bodies (e.g. Corona-Chávez *et al*., 2006). Previous geochronological studies suggest that protoliths of the XC would have constituted a Mesozoic assemblage of igneous and sedimentary rocks (e.g. Talavera-Mendoza *et al*., 2013; Fig. 1). However, evidence for pre-Mesozoic magmatic precursors has also been locally reported (Herrmann *et al*., 1994; Ducea *et al*., 2004; Peña-Alonso *et al*., 2018). According to the available data, the XC has recorded pulses of arc plutonism of Permian (ca. 270 Ma), Jurassic (178–158 Ma) and Early Cretaceous (ca. 130 Ma) age (Morán-Zenteno, 1992; Ducea *et al*., 2004; Solari *et al*., 2007; Pérez-Gutiérrez *et al*., 2009), as well as periods of sedimentation during the Early Jurassic (199–179 Ma) and Late Cretaceous (≤101 Ma) times (Pérez-Gutiérrez *et al*., 2009; Talavera-Mendoza *et al*., 2013).

Metamorphic assemblages in the XC mostly correspond to the upper-amphibolite facies, with local occurrences of granulite-facies rocks (c.f. appendix in Talavera-Mendoza *et al*., 2013). The Acapulco transect (Fig. 1) is dominated by amphibole-bearing orthogneiss, amphibolite (± clinopyroxene), and garnet–sillimanite metapelite, with local occurrences of corundum + cordierite + hercynite assemblages in residual portions (Pérez-Gutiérrez *et al*., 2009). During our reconnaissance fieldwork in that region, we additionally identified non-migmatized metapelites with staurolite + garnet + rutile ± kyanite. Mineral assemblages in the Puerto Ángel transect are instead rather homogeneous, forming garnet–sillimanite metapelite (± hercynite), and amphibolite (± clinopyroxene) with some orthopyroxene ± garnet relics (Corona-Chávez *et al*., 2006). Phase equilibrium modelling and thermobarometry performed on Puerto Ángel migmatites (Corona-Chávez *et al*., 2006) has produced peak *P*–*T* conditions of ~8–10 kbar and ~830–900 ºC. These estimates have been attributed to a single event of H*T* metamorphism and anatexis associated with crustal thickening by contractional deformation. According to Corona-Chávez *et al.* (2006), partial melting in XC initiated along a prograde *P*–*T* path and further progressed during decompression. Nevertheless, this interpretation differs with recent geodynamic models, which ascribe the anatexis merely to a process of orogenic collapse (Peña-Alonso *et al*., 2017) and associated asthenospheric upwelling (Talavera-Mendoza *et al*., 2018).

Previous studies have constrained the age of metamorphism and migmatization of the XC between 64 and 54 Ma (e.g. Talavera-Mendoza *et al*., 2013). However, U–Pb zircon ages obtained from some migmatites have provided evidence for distinct zircon growth episodes at 136–122 Ma and ca. 35 Ma (Herrmann *et al*., 1994; Solari *et al*., 2007; Pérez-Gutiérrez *et al*., 2009; Talavera-Mendoza *et al*., 2013; Estrada-Carmona *et al*., 2016), which suggest a more complicated thermal history than previously thought. Despite these findings, nothing is known concerning the metamorphic framework of these ages and, in consequence, its tectonic significance is widely speculative. A major question remains as to whether these ages record a process of localized heating around plutons, or a regional metamorphic imprint, as it seems to be the case of the tectonothermal event dated at ca. 60 Ma. Eocene migmatite ages overlap in time with the initiation of extension-related magmatism recorded in the Acapulco transect (Talavera-Mendoza *et al*., 2018). According to Talavera-Mendoza *et al*. (2018), this period included at least three pulses of bimodal magmatism and lasted ca. 20 Ma (ca. 60–40 Ma). However, no evidence of such magmatism is known to date in other areas of the terrane, where arc-related granitoids ranging in age from 34 to 25 Ma (U–Pb zircon) are well known instead (e.g. Herrmann *et al*., 1994; Ducea *et al*., 2004).

## 3. Central Xolapa Complex

The study area is located ~30 km north of Pinotepa Nacional in the central region of the XC (~98° W longitude; Fig. 1). The metamorphic sequence cropping out in this area can be described in terms of a predominating metasedimentary unit dominated by migmatitic paragneiss (with variable composition) and garnet-bearing mafic schist, and a metaigneous unit comprising migmatitic quartzofeldspathic orthogneiss and amphibolite (Fig. 2). This sequence is cross-cut by granitic aplite-pegmatite dikes (syn- and post-anatectic) and undeformed granitoids belonging to the Ometepec–Jamiltepec batholith dated at ca. 30 Ma (Herrmann *et al*., 1994; Morán-Zenteno *et al*., 2018). Although the area preserves evidence for complex polyphase deformation (see Corona-Chávez *et al*., 2006 for a structural framework), the regionally dominant foliation is controlled by late-stage anatectic structures ($S_3$) developing a system of E–SE-verging overturned folds, which affect a pre-anatectic (H*T*) gneissic ($S_1$) to early-stage anatectic foliation ($S_2$). This configuration is disrupted by post-anatectic ductile-brittle structures associated with an asymmetrical N-plunging anticlinorium macrostructure ($S_4$) and left-lateral, E–W trending shear zones ($S_5$), whose extension is largely accommodated by NE–SW trending normal faults.

### 3.1. Metasedimentary unit

The metasedimentary unit represents ~40 % of the studied area and possess a considerably variable lithic character. Representative outcrops are exposed within the bed of the Camarón River, south of Amuzgos (Fig. 2). The sequence comprises migmatitic paragneiss interlayered with garnet-bearing mafic schist, marble, graphite quartzite and minor calc-silicate rock bodies.

Migmatitic paragneiss is mostly characterized by outcrop- to hand sample-scale stromatic layering, which is generally parallel to alternating metapelite and metapsammite layers of variable thickness. At the outcrop scale, leucosome is observed to comprise 20–40 vol.%. However, the sequence can be quite variable in terms of leucosome volume and thus in morphology, ranging from dilation- and net-structured metatexite to schollen and schlieren diatexite (according to nomenclature by Sawyer, 2008). Areas dominated by diatexitic morphologies are commonly related to meter-scale anatectic granite bodies.

Stromatic paragneiss contains leucosome bands between 0.1 and 30 cm thick (Fig. 3a), which consist of medium- to coarse-grained aggregates of quartz, alkali feldspar, and plagioclase, plus traces of garnet, biotite, monazite, zircon, and apatite. Melanosome and mesosome portions consist of biotite-rich domains of variable grain size that display a closely spaced, anastomosing foliation. In metapelite layers, they typically comprise sillimanite, garnet, plagioclase, K-feldspar, ilmenite, monazite, zircon, and apatite, with variable contents of quartz, cordierite, hercynite, and corundum. Common secondary phases include chlorite and muscovite.

Migmatitic paragneiss commonly alternates at outcrop scale (≤10–40 vol.%) with centimeter- to meter-thick layers of garnet-bearing mafic schist. This rock type occurs as laterally semi-continuous bodies with only minor macroscopic evidence for partial melting (Fig. 3b), and thus mostly represents refractory components within the unit. Mineral assemblages generally contain porphyroblastic garnet (up to 5 cm in diameter) set in a matrix of aligned amphibole, biotite, plagioclase and quartz. Accessory phases comprise K-feldspar, ilmenite, apatite, allanite-piemontite, zircon, and locally orthopyroxene. Leucosome (≤5 vol.%) forms millimeter-thick bands, as well as irregular patches or films around garnet porphyroblasts. Even though garnet-bearing mafic schist shows features that suggest a magmatic origin, it is included within this unit because its conspicuous association with psammo-pelitic metasediments. Quartzite and calc-silicate rock intercalations typically occur as centimeter-thick refractory layers, whereas marble bodies are found as massive, coarse-grained blocks up to tens of meters thick.

### 3.2. Metaigneous unit

This unit is essentially composed by quartzofeldspathic orthogneiss with variable amount of neosome (≤30 vol.%) and interlayered amphibolite bodies (Fig. 3c). A typical section can be observed along the road connecting Cacahuatepec with Huajintepec village (Fig. 2). Quartzofeldspathic orthogneiss range from granitic to tonalitic in composition and display pronounced outcrop-scale layering defined by concentration of biotite and amphibole. Common mineral assemblages comprise plagioclase, quartz, K-feldspar, biotite and amphibole, with accessory Fe-Ti oxide, apatite, zircon, titanite and garnet. Stromatic to schollen structures are common, where coarse-grained, plagioclase-rich leucosomes include peritectic clinopyroxene (up to 30 cm in size) and amphibole (Fig. 3d). Amphibolite is widely distributed within orthogneiss, occurring as meter-scale layers and blocks of refractory character. Melting degree is typically low (<5 vol.%) as deduced from sparse centimeter-scale patches of tonalitic leucosome. This rock type is composed by polygonal aggregates of amphibole, plagioclase, clinopyroxene and Fe-Ti oxide, with minor content of biotite, epidote, titanite, quartz, apatite and zircon.

## 4. Petrography and mineral compositions

To constrain the metamorphic evolution at central XC, further study was performed on migmatitic paragneiss and alternating garnet-bearing mafic schist from the metasedimentary unit. Methods and analytical procedures of the study are described in the Supplemental material. Two migmatitic pelitic paragneisses (A37 and A57) and one garnet-bearing mafic schist (A64) were chosen for detailed petrographic and mineral chemical study. Representative mineral compositions from each sample are given in Table 1.

### 4.1. Migmatitic pelitic paragneiss

The migmatitic pelitic paragneiss (hereafter metapelite) A37 contains relatively thin (0.1–3 cm thick; Fig. 4a) stromatic leucosome segregations (≤20 vol.%). The mineral assemblage in the cleavage domains comprises biotite, sillimanite, garnet, plagioclase, K-feldspar, quartz, hercynite, ilmenite, monazite, zircon, and apatite (Fig. 4b). A well-developed foliation is defined by aligned biotite and elongated aggregates of fibrous to prismatic (up to 2 cm length) sillimanite. Some lenticular to sub-rectangular bundles of sillimanite suggest pseudomorphic replacement of former kyanite. Sillimanite is also present as fine-grained needles inside hercynite, and locally associated with retrograde garnet replacement. Garnet (10–12 vol.%) is present as anhedral to subhedral porphyroblasts (up to 1 cm in diameter) with inclusions of quartz, biotite, ilmenite, rutile, staurolite ($X_{Mg}$=0.21–0.24), and kyanite (Fig. 4c, d). In some cases, they are partially replaced by fine-grained aggregates of plagioclase, biotite, quartz, and rare sillimanite. Garnet has a compositional range of $Alm_{68–73}Prp_{11–20}Grs_{3–5}Sps_{4–18}$, displaying weak compositional zoning from core (relatively Fe- and Mg-rich) to rim (relatively Mn-rich), typical of diffusional re-equilibration (Fig. 5a). A distinct garnet generation, commonly associated with leucosome domains, is chemically indistinguishable but differs in the nature of its inclusions, which mainly include biotite, sillimanite and quartz. Biotite (~40 vol.%) exhibits a restricted range in composition with $X_{Mg}$ [Mg/(Mg+$Fe^{2+}$)] of 0.33–0.37 and Ti contents of 0.13–0.20 pfu (Fig. 5b), although is slightly more magnesian (0.38–0.39) and Ti-poor (≤0.11 pfu) where is a product of garnet replacement. Hercynite (<1 vol.%) has $X_{Mg}$ ranging from 0.12 to 0.13 and maximum ZnO contents of 1.1 wt%. It generally forms poikiloblasts overgrowing foliation planes, with abundant inclusions of sillimanite, plagioclase, and biotite, but symplectitic intergrowth among these minerals is also common. Plagioclase shows systematic chemical variation between leucosome and cleavage domains (Fig. 5c) with $X_{An}$ [Ca/(Ca+Na+K)] of 0.14–0.17 and 0.32–0.38, respectively. Relatively high $X_{An}$ values of 0.40–046, moreover, are found in both plagioclase intergrown with hercynite and the one replacing garnet.

Metapelite A57 is a corundum-bearing migmatite with relatively thick (up to 30 cm thick) leucosome layers (≥30 vol.%), which are spatially connected to semi-discordant (meter-scale) neosome accumulations. Cleavage domains are quartz-free and consist of biotite, sillimanite, garnet, plagioclase, K-feldspar, hercynite, corundum, ilmenite, monazite, zircon, and apatite. Garnet (8–10 vol.%) occurs as ellipsoidal porphyroblasts (up to 1 cm in diameter) containing inclusions of sillimanite, biotite, plagioclase, quartz, and ilmenite (some grains include mostly sillimanite). It is worth noting that no inclusions of staurolite, kyanite, or rutile were found in this sample. These porphyroblasts are in some cases surrounded by plagioclase-rich coronas, with or without minor biotite or sillimanite. Garnet has a compositional range of $Alm_{67–75}Prp_{10–21}Grs_{4–5}Sps_{5–15}$ and, like A37, shows compositional profiles modified by diffusional re-equilibration (Fig. 5a). Biotite (40–45 vol.%) tends to be homogeneous in composition, with $X_{Mg}$ of 0.34–0.40 and Ti contents of 0.16–0.21 pfu, but some tiny flakes occurring as embayments in garnet may have Ti contents as low as 0.06 pfu (Fig. 5b). Subhedral corundum porphyroblasts (<2 vol.%), up to 2 cm in length, contain inclusions of biotite and K-feldspar, and exhibit both simple and lamellar twinning. Corundum may additionally occur as fine-grained (<1 mm) subhedral to anhedral grains spatially related, but rarely in contact, with hercynite (Fig. 4e). Hercynite (~2 vol.%) exhibits grain shapes ranging form equant to dendritic, and is generally observed as either fine-grained aggregates replacing aligned biotite (Fig. 4f) or in vermicular intergrowth with plagioclase, but it also occur as individual poikiloblasts with inclusions of sillimanite, plagioclase and biotite. The composition of hercynite is however relatively homogeneous, with $X_{Mg}$ of 0.13–0.16, and ZnO contents between 1.5 and 2.4 wt%. Plagioclase composition is considerably variable according its textural setting (Fig. 5c), having $X_{An}$ of 0.30–0.35 and ~0.65 in leucosome and cleavage domains, respectively. Again, appreciably higher $X_{An}$ values of 0.74–0.90 are typical of both plagioclase coronas around garnet and grains intergrown with hercynite. The latter is commonly replaced by radial aggregates of margarite.

### 4.1. Garnet-bearing mafic schist

Mafic schist A64 occurs as a ~1 m thick layer intercalated within a stromatic garnet-sillimanite metapelite. This rock is composed by garnet porphyroblasts in a medium-grained matrix of aligned amphibole, biotite, plagioclase and quartz (Fig. 6a, b). Leucosome (≤3 vol.%) mostly occur at the millimeter scale, ranging from irregular patches to elongated pods, typically along garnet grain boundaries. These domains contain K-feldspar ($X_{Or}$~0.98) forming cuspate boundaries between rounded quartz and plagioclase ($X_{An}$~0.45) grains (Fig. 6c), and hence represent *in situ* neosome (e.g. Sawyer, 2001). Garnet (12–14 vol.%) forms subhedral poikiloblasts (0.5–3 cm in diameter) with inclusions of quartz, biotite, amphibole, ilmenite, and apatite. It shows complex compositional profiles (Fig. 5a), containing apparent relic cores delineated by near-to-core Fe annular maxima. A progressive zonation with increasing Mn and decreasing Mg and Ca is observed rimward. Amphibole (~20 vol.%) displays optically visible zoning, with brownish ferro-pargasite cores and greenish ferro-hornblende rims (according to Hawthorne *et al*., 2012; Fig 5d). This mineral is in contact with all other phases and is interpreted as part of the prograde assemblage. Some amphibole grains adjacent to garnet show both rounded and corroded boundaries, which are typically related to leucosome and orthopyroxene generation (Fig. 6c, d). Biotite (~18 vol.%) is present as reddish brown oriented laths, commonly intergrown with amphibole, and display a range in composition with $X_{Mg}$ of 0.35–0.40 and Ti contents of 0.10–0.25 pfu (Fig. 5b). Like amphibole, corroded biotite grains occur along garnet boundaries, and are spatially related to the presence of leucosome, orthopyroxene, and ilmenite. Some matrix biotite crystals display incipient replacement by late-stage chlorite. Orthopyroxene (<2 vol.%) occur as anhedral grains with $X_{Mg}$ ranging from 0.44 to 0.48 and $Al_2O_3$ contents up to 1.4 wt%. Matrix plagioclase is anhedral to subhedral and is typically more calcic than that in leucosome, with $X_{An}$ of 0.52–0.66 (Fig. 5c). Plagioclase and quartz together represent about 40–50 vol.% of the sample. In addition to ilmenite, accessory phases comprise apatite, allanite-piemontite, and zircon.

## 5. Phase equilibria modelling

Phase equilibria modelling was undertaken in order to provide constraints on the *P*–*T* evolution at central XC. Calculations were performed using the Theriak-Domino package (de Capitani and Petrakakis, 2010) and the internally consistent thermodynamic data set of Holland and Powell (2011) (update ds62). Metapelite A57 and mafic schist A64 were modelled in the NCKFMASHTO ($Na_2O$–CaO–$K_2O$–FeO–MgO–$Al_2O_3$–$SiO_2$–$H_2O$–$TiO_2$–$O_2$) system employing the following *a*–*x* relations: (A57) garnet, chlorite, biotite, staurolite, chloritoid, cordierite, orthopyroxene, white mica, ilmenite and melt (White *et al*., 2014a); plagioclase and K-feldspar (Holland and Powell, 2003); spinel–magnetite (White *et al*., 2002); sapphirine (Wheller and Powell, 2014); (A64) melt, augite and hornblende (Green *et al*., 2016); garnet, chlorite, biotite, orthopyroxene, white mica and ilmenite (White *et al*., 2014a); epidote and olivine (Holland and Powell, 2011); plagioclase and K-feldspar (Holland and Powell, 2003); spinel–magnetite (White *et al*., 2002). Metapelite A37 was modelled at subsolidus conditions adding MnO to the model system, and using the extended *a*–*x* relations of White *et al.* (2014b) and the order–disorder model of magnetite of White *et al.* (2000). Pure phases comprised quartz, rutile, titanite, corundum, aluminosilicate polymorphs and aqueous fluid ($H_2O$). Calculations use compositions based on bulk-rock analyses (Table 2). The loss on ignition (LOI) in samples A57 and A64 was taken as a proxy for the bulk $H_2O$ content present during metamorphism, whereas sample A37 was modeled with variable $H_2O$ values. For bulk-rock $X_{Fe3+}$ ratios [$Fe^{3+}/(Fe^{3+}+Fe^{2+})$], values of 0.05 (metapelite) and 0.1 (mafic schist) were assumed, which are close to the QFM oxygen buffer at the modelled conditions (Diener and Powell, 2010) and therefore favor the prediction of ilmenite instead of magnetite and hematite. Compositions were also adjusted for the presence of accessory apatite in each sample, which resulted in minor reductions in CaO content.

### 5.1. Metapelites A37 and A57

Metapelite A37 preserves relics of a prograde, amphibolite-facies assemblage and exhibits thin stromatic layers; with leucosome representing in-source melt segregation. The bulk composition of the sample is therefore considered approximate to protolith composition, and was used to investigate the subsolidus *P–T* evolution. Given the presence of hydrous minerals like biotite and staurolite, it is likely the measured LOI value does not record the actual $H_2O$ content in the rock during metamorphism, so phase equilibria were initially investigated at $H_2O$-saturated conditions. The calculated *P–T* phase diagram (Fig. 7a) exhibits relatively low-variance assemblage fields and a fluid-saturated solidus between 650 and 680 °C. Minimum pressures of prograde metamorphism are given by the predicted stabilization of rutile at 8–9 kbar. The observed prograde assemblage containing Grt–Ky–St–Rt is not completely reproduced (bold text at ~640–670 °C, 8–9 kbar in Fig. 7a) because this water-saturated model does not predict kyanite over the entire *P–T* range. However, kyanite stabilization in metapelites is known to be sensitive to minor changes in the $H_2O$ content (e.g. Maldonado *et al*., 2016), hence a *P–*$H_2O$ phase diagram at 660 °C (Fig. 7b) was constructed to evaluate its influence on the calculated assemblages. Figure 7b shows that kyanite is predicted to be stable at relatively high-pressure conditions (>7 kbar) and low $H_2O$ content. The interpreted prograde assemblage of Grt–Ky–St–Rt–Pl–Bt–Ms–Ilm–Qz is calculated to occur at 8–9 kbar, just below the curve of $H_2O$ saturation (bold text at 7–8 mol. % $H_2O$). The upper pressure limit for crystallization of the observed relic assemblage is deduced from both models by the predicted disappearance of staurolite at ~9 kbar. These results suggest a stage of equilibration at ~640–670 °C and 8–9 kbar during prograde metamorphism of metapelite A37. In the absence of other features that allow further constraint on *P–T* conditions, this model based on nature of mineral inclusions and assumption of partial preservation of protolith composition is considered a simple but reasonable approach to outline part of the subsolidus evolution of this sample.

Modelling of the highly segregated, corundum-bearing metapelite A57 was undertaken using the bulk composition of a meter-scale residual layer. Figures 7c, d show the calculated *P*–*T* phase diagram, where a fluid-undersaturated solidus is predicted to occur between ~750 and 810 °C. The assemblage Grt–Hc–Sil–Crn–Bt–Pl–Kfs–Ilm–L observed in this sample is predicted to be stable over a narrow field at *P*–*T* conditions of ~800–860 °C and 6–7 kbar (bold text in Fig. 7c), which likely represent conditions of peak metamorphism following any melt loss during prograde metamorphism and migmatization. The *P*–*T* range of interest is constrained by the hercynite and garnet stability limits. According to the model, corundum tends to be stable at relatively high-pressure conditions, in contrast to hercynite-bearing assemblages that are restricted to lower pressures. In fact, a corundum–hercynite boundary can be virtually traced, which is consistent with the equilibrium Alm + 5Crn = 3Hc + 3Sil investigated experimentally by Shulters and Bohlen (1989). Reaction textures among these phases are however absent in metapelite A57. Conditions of peak metamorphism can be further constrained by correlating observed and predicted proportions of temperature-dependent phases (Powell and Holland, 2008; Palin *et al*., 2018) like biotite and hercynite (Fig. 7d). The modal proportion of hercynite is predicted to be highly temperature sensitive, increasing directly as biotite decreases across the *P*–*T* range of interest, an estimate that is consistent with the observed textural relations between these phases (e.g. Fig 4e). The best match is provided at the lowermost limit of the peak assemblage field (~820 °C, 6.5 kbar), just above the calculated solidus, with only ~2 vol.% hercynite and 40–45 vol.% biotite observed in thin section. However, the preserved assemblage is likely to be that at the solidus during cooling, rather than the one developed at the maximum temperature (Kriegsman, 2001; White and Powell, 2002), so this result would provide conditions of near-peak metamorphism attained by metapelite A57.

### 5.2. Garnet-bearing mafic schist A64

As mafic schist A64 represents a refractory layer intercalated within a stromatic metapelite similar to A57, both rocks must have experienced the same tectonothermal evolution. This fact allows evaluation of *P–T* conditions of metamorphism recorded by a peak mineral assemblage developed just upon reaching suprasolidus conditions. The *P–T* phase diagram performed for A64 (Fig. 7e, f) displays a fluid-undersaturated solidus between ~730 and 810 °C. Destabilization of amphibole is predicted to occur at considerable lower temperature (up to ~100 °C) with regard to the biotite breakdown. The interpreted peak assemblage of Grt–Bt–Amp–Opx–Ilm–Pl–Qz plus melt occur as a narrow, positive-slope field up to *P–T* conditions of ~850–900 °C and ~8–9 kbar. Minimum pressure conditions are given by the predicted destabilization of garnet at ~5 kbar (at solidus temperature). According to the model, the modal proportions of biotite and melt vary directly with temperature, with biotite being consumed as melt increases from 0 to 16 vol.% across the assemblage field of interest (Fig. 7f). The observed abundances of biotite (~18 vol.%) and leucosome (≤3 vol.%) have a good match within the predicted peak assemblage field suggesting equilibration at *P–T* conditions of ~800–820 °C and ~5–7 kbar, just above the calculated solidus. This result provides a close correlation to the *P–T* conditions derived from metapelite A57, and likely constrains the metamorphic conditions at which mafic schist A64 preserved its final (peak) mineral assemblage upon crossing the solidus.

## 6. U–Pb geochronology and Ti-in-zircon thermometry

Monazite and zircon from the studied metapelites (A37 and A57), as well as zircon from the garnet-bearing mafic schist A64 and one additional (analogous) sample (A63b), were used for LA-ICP-MS U–Pb dating. Additionally, temperature of metamorphic zircon crystallization was estimated using Ti-in-zircon thermometry. The U–Pb results, plotted in Wetherill concordia diagrams, together with scanning electron microscope (SEM) images of representative analyzed crystals are shown in Figures 8 and 9. The analytical results are presented in Table 1 of the Supplemental material.

### 6.1. Monazite U–Pb results

Monazite in metapelite A37 occurs mainly in biotite-rich domains as anhedral grains up to ~150 μm in size. Backscattered electron (BSE) imaging reveals a gradual core-to-rim zoning, with rims displaying relatively low-BSE emission (Y rich). Eight crystals were analyzed for a total of 21 laser spots that yield concordant to slightly discordant (up to 16 %) results (Fig. 8a). A cluster of 18 analyses ranges in $^{206}Pb/^{238}U$ ages from 67 to 54 Ma, giving a weighted mean age of 61.4±0.3 Ma (MSWD=12.8). The remainder 3 analyses give both concordant and discordant U–Pb dates of 47 and 33–31 Ma, respectively, which may reflect partial Pb loss during a subsequent reheating.

Nineteen monazite grains from sample A57 were analyzed. Some crystals contain irregular cores with overgrowths displaying either concentric or patchy zoning. A total of 48 laser spots were performed, most of which give results that spread along concordia (Fig. 8b). Forty-four analyses from the overgrowths give $^{206}Pb/^{238}U$ ages between 68 and 25 Ma, with only one only analysis at ca. 83 Ma. These ages systematically get younger towards crystal rims, roughly defining two clusters at ≥50 and ≤40 Ma. In addition, a group of 6 concordant core analyses yields $^{206}Pb/^{238}U$ dates between 125 and 101 Ma, which likely represent ages of a detrital component or, alternatively, the timing of an early stage of metamorphic growth.

Definition of three main age populations at 125–101, ca. 60 Ma and ca. 33 Ma can be more evident by plotting together data from both metapelites on a kernel density estimate (KDE) diagram (Fig. 8c). Dates between the two younger populations may represent mixed dates with no geological significance. These age groups correlate well with textural/chemical setting, with older dates being restricted to monazite cores, the ca. 60 Ma population associated with internal, relatively Y-poor zones, and the ca. 33 Ma group characteristic of Y-rich rim domains (Fig. 8d).

### 6.2. Zircon U–Pb results

#### 6.2.1. Metapelite

Zircon (whole rock separates) from metapelite A37 forms equant to elongate (aspect ratios up to 1:5) euhedral prisms, composed by relic (detrital) cores, internal low-cathodoluminescence (CL) zones, and bright homogeneous overgrowths. From a total of 37 laser-spots performed in this sample, 13 analyses of the internal domains (Th/U=0.19–0.01) give $^{206}Pb/^{238}U$ ages between 73 and 58 Ma (Fig. 9a). Excluding the oldest analysis, this relatively low-Th/U zircon gives a weighted mean age of 60.9±0.5 Ma (MSWD=5.9). Additionally, 24 analyses of the overgrowth domains (Th/U=0.39–0.17) yield $^{206}Pb/^{238}U$ ages of 29–25 Ma, with a weighted mean age of 26.5±0.2 Ma (MSWD=1.0; one datum discarded). No detrital ages were obtained for this sample.

Zircon from metapelite A57 comes from a garnet-bearing leucosome layer and occurs as prismatic crystals (elongation ratios up to 1:5) displaying low-CL detrital cores and bright homogeneous overgrowths. Twenty-six analyses of overgrowths (Th/U=0.30–0.01) result in $^{206}Pb/^{238}U$ ages that spread between 79 and 36 Ma (Fig. 9b), from which a cluster of 18 laser spots yields a weighted mean age of 61.8±0.6 Ma (MSWD=4.8). This leucosome zircon age is thus consistent with the age obtained for low-Th/U zircon from whole metapelite A37. The younger data (<54 Ma, n=6) are concordant to slightly discordant and likely result from recrystallization or partial Pb loss during a later thermal disturbance. The analyzed detrital cores (not shown in Fig. 9b) yield concordant $^{206}Pb/^{238}U$ dates of 2600, 1023, 600 and 155 Ma that suggest post-Jurassic deposition of the sedimentary protolith.

### 6.2.2. Garnet-bearing mafic schist

Zircon grains from A63b and A64 are similar regarding morphology and zoning patterns. They mostly occur as elongated prisms with high aspect ratios of up to 1:6, typical of rapidly crystallized rocks (e.g. Corfu et al., 2003). Internal textures are complex and reflect intensive modification of primary structures by recrystallization or dissolution/precipitation processes. Secondary zircon occurs as unzoned patches and embayments, with relatively high-CL emission, replacing oscillatory zoned zircon. Some grains display ghost textures, common in partially erased growth zoning by annealing (e.g. Schaltegger et al., 1999).

From a total of 29 laser spots performed in sample A63b, a cluster of 26 analyses from both oscillatory and unzoned domains (Th/U=1.27–0.05) yield $^{206}Pb/^{238}U$ ages between 37 and 31 Ma (Fig. 9c), with a weighted mean age of 33.8±0.3 Ma (MSWD=5.1). Two more spots give concordant ages of ca. 74 and 62 Ma (Th/U=0.35–0.33), respectively, and only one analysis from oscillatory domains result in a slightly discordant date of ca. 94 Ma (Th/U=0.53), which likely represents an isotopically disturbed magmatic relic.

In sample A64, 26 out of 36 analyzed laser spots spread almost continuously along concordia between 63 and 31 Ma (Th/U=1.05–0.03; Fig. 9d). However, these dates does not exhibit any systematic correspondence with morphological features or zoning patterns, and such an age distribution probably reflect partial resetting of the U–Pb isotope system by a thermal perturbation at ca. 31 Ma. A cluster of 7 analyses performed on either oscillatory or overgrowth domains gives a weighted $^{206}Pb/^{238}U$ mean age of 32.8±0.7 Ma (MSWD=0.3). The remaining 10 analyses, performed on oscillatory zoning domains (Th/U=0.62–0.05), yield concordant to slightly discordant results between 132–123 (n=5) and 119–95 (n=5) Ma. The older ages likely represent the crystallization age range (after any isotopic disturbance) for the magmatic protolith, whereas the younger interval may reflect variable Pb loss during the later isotopic disturbance.

### 6.3. Ti-in-zircon thermometry

The Ti-in-zircon thermometer of Ferry and Watson (2007) was applied to metamorphic zircons from metapelite (A37, A57) and mafic schist (A63b, A64) samples. Calculations of temperatures were performed using a range of Ti activities of 0.6–1.0. The Ti content of zircon in metapelite A37 ranges from 1.4–12.0 (Paleocene ages) to 1.5–7.9 (Oligocene ages), whereas in A57 is of 0.7–6.8 (Paleocene). Calculated average temperatures for Paleocene zircon range from 656–689 ($a_{Ti}$=1) to 734–773 ($a_{Ti}$=0.6) °C, and from 664 ($a_{Ti}$=1) to 743 ($a_{Ti}$=0.6) °C in Oligocene zircon. No clear correlation between temperature and U–Pb age is observed. In mafic schists A63b and A64, the Ti contents range from 2.5–13.9 to 4.1–17.8, respectively, and show no correspondence with age. Calculated average temperatures tend to be higher than obtained from metapelite samples, ranging between 714–715 ($a_{Ti}$=1) and 802–805 ($a_{Ti}$=0.6) °C.

## 7. Discussion and conclusions

### 7.1. Peak metamorphism and partial melting conditions

Metamorphic rocks exposed in central XC show extensive petrographic evidence for having experienced very H*T* (granulite-facies) metamorphism and anatexis. A distinguish feature in the area is the occurrence of pervasive migmatization that resulted from a feedback relation between differential melting of interlayered fertile–refractory rocks, and syn-anatectic heterogeneous deformation (Brown and Solar, 1998; Corona-Chávez et al., 2006). Partial melting of metapelite form the metasedimentary unit led to formation of both silica-saturated (e.g. A37) and silica-deficient (e.g. A57) peak mineral assemblages. Petrographic evidence suggests that neosome generation (20–40 vol.% melt) was coeval with garnet crystallization, indicating fluid-absent melting reaction of biotite at medium pressure (M*P)*–H*T* conditions (Patiño-Douce and Johnston, 1991; Spear et al., 1999; Vielzeuf and Schmidt, 2001, White et al., 2007). Biotite, sillimanite and quartz inclusions in leucosome garnet from metapelite A37 (silica-saturated) suggest a simplified dehydration-melting reaction of the type: Bt + Sil + Pl + Qz = Grt + L ± Kfs, which represent the earliest recognizable stage of partial melting in the study area. Meanwhile, anatexis of metapelite A57 (silica-deficient) likely occurred via biotite breakdown to produce melt together with peritectic garnet and corundum. This association instead suggests an advanced stage of anatexis with higher volumes of melt extraction, and could imply a progressive reaction of the type: Bt + Sil = Grt + Crn + L ± Kfs. Hercynite (Zn ≤2.4 wt%.) have clearly formed after biotite breakdown in metapelite residuum (Fig. 4). This observation agrees with conclusion by Montel et al. (1986), who interpreted Zn-poor hercynite in H*T* metapelites as indicative of advanced, silica-deficient conditions of anatexis. Although the assemblage garnet + corundum + hercynite is considered to have been equilibrated during near-peak metamorphism, porphyroblast–matrix relations suggest that hercynite might have grown relatively late during partial melting. This scenario is consistent with the virtual corundum–hercynite boundary delineated in Figure 7c, which shows that hercynite tends to be stable towards relatively L*P* conditions. Replacement microstructures and inclusions within hercynite denote indeed a distinct reaction balance like: Bt + Pl + Sil = Hc + L ± Crn. All these features together, imply that hercynite growth would likely have prolonged until a late melting stage, as pressure progressively decreased.

The silica-deficient melanosome of metapelite A57 was used to estimate peak *P*–*T* conditions. We assume that this part represents a biotite-rich residue concentrated (and equilibrated at peak conditions) after volume loss by melt extraction. Phase equilibria modelling suggests that this metapelite underwent conditions of ~820 °C, 6–7 kbar, which are interpreted to reflect near-peak *P*–*T* conditions attained after considerable melt loss (Fig. 10). These values are slightly lower in temperature, but in general agree with the *P*–*T* estimates by Corona-Chávez et al. (2006). Our modelling focuses on mineral assemblages fields and modal contents rather than on mineral compositions, because of the probability of down-*T* reequilibration from peak conditions (Frost and Chacko, 1989; Fitzsimons and Harley, 1994; Kohn and Spear, 2000). The observed textures (e.g. coronas between garnet and leucosome) and mineral compositions (e.g. An content in plagioclase) in this particular metapelite reflect only local melt-consuming reaction during subsequent residue–melt interaction (e.g. Kriegsman and Álvarez-Valero, 2010). Although this *P*–*T* determination is reasonable and in accordance with many other studies on granulite-facies migmatites (e.g. Chacko et al., 1987; Jones and Brown, 1990; Fitzsimons, 1996), the early association of garnet + corundum implies that peak metamorphism at higher pressure conditions cannot be ruled out (dashed segment in Fig. 10), as have been documented in some other M*P*–(ultra)H*T* belts (e.g. Sengupta et al., 1999; Ouzegane et al., 2003; Kelsey et al., 2006).

Garnet-bearing mafic schist (e.g. A64) from the metasedimentary unit allows evaluation of metamorphism in co-metamorphic refractory layers, and thus provides additional constraints on H*T* metamorphism in central XC. The most relevant feature of this rock type is the association of orthopyroxene, ilmenite and K-feldspar-bearing leucosome pockets around engulfed garnet poikiloblasts (Fig. 6). Leucosome is also texturally associated with corroded biotite and amphibole, which suggests simultaneous dehydration-melting reaction of both phases according to a balance like: Bt + Amp + Grt + Qz = Opx + Ilm + L. Petrological modelling performed on mafic schist A64 support that growth of orthopyroxene within the observed peak assemblage was related to a stage of incipient melt production and associated biotite–amphibole consumption (Fig. 7e, f). Calculated *P*–*T* conditions of ~800–820 °C and ~5–7 kbar are in good agreement with values derived from associated metapelites. This consistency between samples with contrasting whole-rock compositions (and melting degrees) leads us to conclude, on the one hand, that the used thermobarometric approach provides an accurate estimate of peak metamorphic conditions recorded in central XC, and on the other, that the investigated samples experienced the same tectonothermal history.

### 7.2. Evidence of crustal thickening during the XC evolution

Although H*T* metamorphism erased most of the prograde features in central XC, relic mineral assemblages provide some relevant clues to its early metamorphic evolution. The occurrence of polyphase inclusions of staurolite, kyanite, and rutile in garnet from migmatitic paragneiss indicates a stage of M*P*–medium temperature (M*T*) metamorphism prior to granulite-facies migmatization took place at ≥62 Ma (Fig. 10; see below). Our reconnaissance fieldwork allowed us to confirm that similar mineral assemblages are also preserved at the Acapulco transect (see also appendix in Talavera-Mendoza et al., 2013). Phase equilibria modelling suggests that this stage of crystallization occurred at *P*–*T* conditions of ~640–670 °C and 8–9 kbar, which imply burial to depths of ~30 km. These results contrast with previous interpretations that metamorphism and partial melting in the XC were caused only by increasing thermal input associated with late Cretaceous–early Paleogene extensional tectonics (Ratschbacher et al., 1991; Riller et al., 1992; Herrmann et al., 1994; Peña-Alonso et al., 2017).

Many H*T* metamorphic belts preserve evidence for an earlier, higher pressure stage, which indicates an initial period of crustal thickening (e.g. Jones and Brown, 1990; Soto and Platt, 1999; Harris et al., 2004; Hallet and Spear, 2014), and points to a setting in a collisional or accretionary orogen. The geodynamic context of Barrovian-type metamorphism in some of the best-known terranes remains, nevertheless, a topic of continued debate today (e.g. Ryan and Dewey, 2019). A number of recent studies have demonstrated that orogenic metamorphism can occur over considerably short timescales (≤10 Ma; e.g. Ague and Baxter, 2007; Smye et al., 2011), which are inconsistent with the periods (>20 Ma) required by the thermal relaxation models (e.g. England and Thompson, 1984). Short-lived orogens typically occur in association with episodic magmatism (e.g. Viete et al., 2013 and references cited therein), so heat advection from the lower crust and/or mantle has been regarded as a plausible mechanism capable to supply large amounts of heat for Barrovian-type metamorphism quickly (Ryan and Dewey, 2019). The Xolapa terrane lacks of Late Cretaceous magmatism, whereas Paleocene granitoids are apparently rare and restricted to the Acapulco transect (Solari et al., 2007; Talavera-Mendoza et al., 2018). In consequence, M*P*–M*T* metamorphism recorded in the XC would not be related to magmatic advection, either by magmatic arc activity or lithospheric thinning. We interpret, therefore, that this metamorphic stage must reflect crustal thickening occurred during an orogenic episode sometime in the latest Cretaceous (see below). Subsequent H*T* metamorphism and progressive anatexis would occur during the late stage of orogen building. In the tectonic setting of southern Mexico, thickening of XC coincide in time with the Mexican orogen that spans approximately 60 Ma from the Early Cretaceous through the Eocene (Fitz-Díaz et al., 2018), but additional study is required to argue a possible correlation.

### 7.3. Timing of metamorphism and partial melting

The timing of anatexis in the XC has been addressed by several authors, and remains a matter of current controversy (e.g. Estrada-Carmona et al., 2016). While most of the interest to date has focused on dating the migmatization (one or more), other metamorphic stages have received no attention. In this work, we have obtained U–Pb age data from co-metamorphic rocks with different compositions and melting degrees, and used both zircon and monazite in order to assess two potentially different isotopic records of a presumably long-lasting metamorphic history.

The age of M*P*–M*T* metamorphism in the central XC is poorly constrained by the data because of limited preservation of prograde zircon and monazite after subsequent H*T* evolution.

However, a few concordant dates (n=9) between 125 and 70 Ma were obtained from metapelite samples (Fig. 8, 9). This age range is significantly younger than the maximum depositional ages (Upper Triassic) reported for metapelites from the region, but older than their migmatization ages (Talavera-Mendoza et al., 2013). The older data, particularly a cluster at 112–101 Ma (n=4), were obtained from monazite cores from the metapelite A57 (inset in Fig. 8b). Since monazite commonly grow at conditions around the staurolite–kyanite isograd (e.g. Smith and Barreiro, 1990; Corrie and Kohn, 2008) and tends to dissolve during partial melting (e.g. Williams, 2001; Yakymchuk and Brown, 2014), these ages might represent an early generation of metamorphic monazite that survived the pervasive migmatization of XC (Fig. 10, 11). A potential limitation of such an interpretation is that it is not possible to ascertain if these data are geologically meaningful and unequivocally attributable to that specific M*P*–M*T* stage, or instead reflect a detrital component with or without later isotopic disturbance. For this reason, we conclude that prograde, Barrovian-type metamorphism in the central XC occurred sometime in the mid- to Late Cretaceous, but further study is required to precise its age and duration.

The time of leucosome crystallization provide a minimum age limit for the anatectic process in the XC (Fig. 11). Leucosome zircon from metapelite A57 give a mean age of ca. 62 Ma, which is interpreted as the time of melt crystallization during cooling (e.g. Kelsey et al., 2008; Kelsey and Powell, 2011; Kohn et al., 2015), being consistent with the obtained Ti-in-zircon temperatures of ~656–773 °C. This conclusion disagree with previous interpretation that Paleocene ages date the tectonothermal event that produced metamorphism and migmatization in the XC (e.g. Herrmann et al., 1994; Talavera-Mendoza et al., 2018; Estrada-Carmona et al., 2016) because, in our view, this age range represents only one stage (neosome crystallization) of a long-lasting metamorphic evolution. All other zircon and monazite data from metapelites also show age populations around ca. 60 Ma. For instance, a cluster at ca. 61 Ma was obtained from whole-rock zircon of metapelite A37, while ages of melanosome monazite in both metapelites has greater dispersion, but shows age density peaks at ca. 60–54 Ma (Fig. 11). X-ray compositional maps reveal, moreover, that this generation of monazite has relatively low Y concentrations, suggesting simultaneous growth with or immediately after garnet (e.g. Foster et al., 2000; Gibson et al., 2004). In fact, monazite ages spreading to ca. 50 Ma may indicate that (unlike zircon) its growth within melanosomes may have continued for a period of at least ca. 10 Ma, which corroborates that protracted monazite crystallization is a common phenomenon in migmatite terranes (e.g. Harley and Nandakumar, 2014; Regis et al., 2014; Hallet and Spear, 2015; Johnson et al., 2015; Yakymchuk et al., 2015; Weinberg, 2016). Zircon from intercalated mafic schist (A63b–A64) has been strongly modified by later thermal events and does not provide any significant insight into the prograde–peak metamorphic stage (Fig. 11).

### 7.4. Oligocene reheating and upper crust residence

Evidence for a late-stage reheating in central XC is provided by Oligocene U–Pb mineral ages from the metasedimentary unit and coeval magmatism. In metapelites, zircon and monazite rim ages of ca. 26 and 33 Ma, respectively, suggest that these phases experienced a process of asynchronous late-stage crystallization (Fig. 11). This episode of mineral formation was not recorded by zircon from the anhydrous leucosome of metapelite A57; so, hydrous (biotite-rich) matrix domains probably favored zircon- and monazite-forming processes. X-ray compositional maps show that monazite rims contain considerably higher Y concentrations than cores, which suggest growth at expense of garnet (e.g. Hallet and Spear, 2015; Yakymchuk et al., 2015). Similar high-Y monazite rims from other migmatites have been interpreted to grow during melt crystallization, after garnet breakdown by residue-melt reaction (e.g. Pyle and Spear, 2003; Kohn et al., 2005; Kelly et al., 2006). However, on the basis of leucosome crystallization ages of ca. 62

Ma, our preferred interpretation is that Oligocene high-Y monazite grew after garnet breakdown during subsolidus late-stage metamorphism. Internal textures on zircon from mafic schist layers, including blurred oscillatory zoning, bleaching patches and embayments, are consistent with intensive modification of pre-existing crystals by recrystallization, replacement or annealing processes (e.g. Pidgeon, 1992; Schaltegger et al., 1999). Age clusters at ca. 34–33 Ma lack any systematic correlation with textural features and thus are interpreted as indicating the time of almost complete resetting of the U–Pb isotope system (Fig. 11).

Oligocene ages largely coincide with the emplacement of continental-arc granitic batholiths in the region (ca. 30 Ma; Herrmann et al., 1994). Therefore, zircon/monazite formation and resetting processes are considered to reflect a late-stage reaction related to reheating by magmatic advection. Recalculation of the Al-in-hornblende barometry presented by Morán-Zenteno et al. (1996), using the formulation by Mutch et al. (2016), suggest emplacement depths of about 15 km (~4 kbar) for the Jamiltepec–Río Verde batholith. On the other hand, the Ti-in-zircon thermometry performed in Oligocene zircon from metapelites suggest growth/recrystallization at temperatures below ~740 °C (Fig. 10). Therefore, the time span from neosome crystallization to late-stage reheating in central XC would imply a protracted H*T* evolution and middle- to upper crust residence time of at least ca. 30 Ma. This period of probable crustal incubation, however, should not have been stationary due to the changing tectonic regime along the Pacific margin of southern Mexico (Boschman et al., 2014; Morán-Zenteno et al. 2018; Peña-Alonso *et al*., 2018; Talavera-Mendoza *et al*. 2018), so further study is required to elucidate the timing and style of the late-stage exhumation of the belt.

### 7.5. Protolith interpretation and regional implications

The metasedimentary unit in central XC is dominated by a sequence of alternating psammo-pelitic and mafic layers. Field, petrological and geochronological data lead us to interpret that this lithological association represents a meta-volcano-sedimentary succession. Detrital zircon U–Pb geochronology of metapelites from this region indicates Late-Triassic (226–203 Ma) maximum depositional ages (Talavera-Mendoza et al., 2013). Besides, zircon U–Pb ages from metapelite A57 suggest post-Jurassic (≤155 Ma) deposition of the sedimentary protolith, whereas the magmatic precursor of interlayered garnet-bearing mafic schist likely crystallized at ca. 132 Ma. Zircon from mafic schists occurs as elongated prisms typical of rapidly crystallized rocks (e.g. Hoskin and Schaltegger, 2003; Corfu et al., 2003), which support a volcanic origin of this rock type. These data are the first evidence for an Early-Cretaceous (Valanginian–Hauterivian) volcano-sedimentary sequence in XC and, even when our database must be still expanded, it provides critical insights into the geological evolution of this metamorphic belt.

Volcano-sedimentary successions similar in age and nature are found in the Arperos basin, as well as at Tolimán, Taxco and Tierra Colorada regions of central-southern Mexico (e.g. Mortensen et al., 2008; Martini et al., 2011; Campa-Uranga et al., 2012; Ortega-Flores et al., 2014; Campa-Uranga et al., 2017). Volcanic and metavolcanic rocks from the last three localities are identical in age (137–130 Ma) to mafic schist A64, but have andesitic to rhyolitic compositions. Mafic schist in central XC tend to be basic to andesitic in composition, therefore an affinity with the Arperos basin, where sedimentation evolved from continentally to oceanic floored during the Early Cretaceous (Martini et al., 2014), may be plausible. Talavera-Mendoza et al. (2013) concluded that the XC recorded two sedimentation cycles of Early Jurassic (199 – 179 Ma) and Late Cretaceous (101–64 Ma) age, which were separated in time by pulses of Middle Jurassic (178–158 Ma) and Early Cretaceous (ca. 130 Ma) magmatism. Our results instead imply that volcanism and sedimentation in the study area were active during the Early

Cretaceous (ca. 132 Ma), being in part coeval with granitic arc magmatism documented in the Acapulco transect (e.g. Solari et al., 2007). In consequence, this period of sedimentation should have continued at least until middle Cretaceous (ca. 101 Ma), but it is unlikely that it has extended far into the Late Cretaceous–Paleocene (ca. 64 Ma) as Talavera-Mendoza et al. (2013) suggest. It must have ceased considerably before ca. 64 Ma because our petrological data demonstrate that the XC underwent a process of crustal thickening and subsequent M*P* anatexis before leucosome crystallized during cooling at ca. 62 Ma, as discussed above. On the other hand, we presume that the Xolapa orogenic process should be contemporary to the deposition of Mexcala-type (Turonian–Maastrichtian) turbidite sequences in southern Mexico.

## References


Ague JJ, Baxter EF (2007) Brief thermal pulses during mountain building recorded by Sr diffusion in apatite and multicomponent diffusion in garnet. Earth and Planetary Science Letters 261:500–516.

Boschman LM, van Hinsbergen DJJ, Torsvik TH, et al (2014) Kinematic reconstruction of the Caribbean region since the Early Jurassic. Earth-Science Reviews 138:102–136.

Brown M (2005) Synergistic effects of melting and deformation: an example from the Variscan belt, western France. Geological Society, London, Special Publications 243:205–226.

Brown M, Solar GS (1998) Shear-zone systems and melts: feedback relations and self-organization in orogenic belts. Journal of Structural Geology 20:211–227.

Campa MF, Coney PJ (1983) Tectono-stratigraphic terranes and mineral resource distributions in Mexico. Can J Earth Sci 20:1040–1051.

Campa-Uranga MF, Torres de León R, Iriondo A, Premo WR (2012) Caracterización geológica de los ensambles metamórficos de Taxco y Taxco el Viejo, Guerrero, México. Boletín de la Sociedad Geológica Mexicana 64:369–385.

Campa-Uranga MF, García-Hernández CU, Buitrón-Sánchez B, et al (2017) Formación Chapolapa: El triásico que no era. Paleontología Mexicana 6(1): 8.

Chacko T, Kumar GRR, Newton RC (1987) Metamorphic P-T Conditions of the Kerala (South India) Khondalite Belt, a Granulite Facies Supracrustal Terrain. The Journal of

Clemens JD, Vielzeuf D (1987) Constraints on melting and magma production in the crust. Earth and Planetary Science Letters 86:287–306.

Corfu F (2003) Atlas of Zircon Textures. Reviews in Mineralogy and Geochemistry 53:469–500.

Corona-Chavez P, Poli S, Bigioggero B (2006) Syn-deformational migmatites and magmatic-arc metamorphism in the Xolapa Complex, southern Mexico. Journal of Metamorphic Geology 24:169–191.

Corrie SL, Kohn MJ (2008) Trace-element distributions in silicates during prograde metamorphic reactions: implications for monazite formation. Journal of Metamorphic Geology 26:451–464.

de Capitani C, Petrakakis K (2010) The computation of equilibrium assemblage diagrams with Theriak/Domino software. American Mineralogist 95:1006–1016.

Diener JFA, Powell R (2010) Influence of ferric iron on the stability of mineral assemblages. Journal of Metamorphic Geology 28:599–613.

Ducea MN, Gehrels GE, Shoemaker S, et al (2004) Geologic evolution of the Xolapa Complex, southern Mexico: Evidence from U-Pb zircon geochronology. Geological Society of America Bulletin 116:1016.

England PC, Thompson AB (1984) Pressure-Temperature-Time Paths of Regional Metamorphism I. Heat Transfer during the Evolution of Regions of Thickened Continental Crust. Journal of Petrology 25:894–928.

Estrada-Carmona J, Solari LA, Ortega-Obregón C (2016) Petrochronology of the migmatization event of the Xolapa Complex, Mexico, microchemistry and equilibrium growth of zircon and garnet. International Geology Review 58:1382–1397.

Ferry JM, Watson EB (2007). New thermodynamic models and revised calibrations for the Ti-in-zircon and Zr-in- rutile thermometers. Contributions to Mineralogy and Petrology 154(4): 429–437.

Fitz-Díaz E, Lawton TF, Juárez-Arriaga E, Chávez-Cabello G (2018) The Cretaceous-Paleogene Mexican orogen: Structure, basin development, magmatism and tectonics. Earth-Science Reviews 183:56–84.
Fitzsimons ICW (1996) Metapelitic Migmatites from Brattstrand Bluffs, East Antarctica–Metamorphism, Melting and Exhumation of the Mid Crust. Journal of Petrology 37:395–414.
Fitzsimons ICW, Harley SL (1994) The Influence of Retrograde Cation Exchange on Granulite P-T Estimates and a Convergence Technique for the Recovery of Peak Metamorphic Conditions. Journal of Petrology 35:543–576.
Foster G, Kinny P, Vance D, et al (2000) The significance of monazite U–Th–Pb age data in metamorphic assemblages; a combined study of monazite and garnet chronometry. Earth and Planetary Science Letters 181:327–340.
Freydier C, Lapierre H, Ruiz J, et al (2000) The Early Cretaceous Arperos basin: an oceanic domain dividing the Guerrero arc from nuclear Mexico evidenced by the geochemistry of the lavas and sediments. Journal of South American Earth Sciences 13:325–336.
Frost BR, Chacko T (1989) The Granulite Uncertainty Principle: Limitations on Thermobarometry in Granulites. The Journal of Geology 97:435–450.
Gibson HD, Carr SD, Brown RL, Hamilton MA (2004) Correlations between chemical and age domains in monazite, and metamorphic reactions involving major pelitic phases: an integration of ID-TIMS and SHRIMP geochronology with Y–Th–U X-ray mapping. Chemical Geology 211:237–260.
Green ECR, White RW, Diener JFA, et al (2016) Activity-composition relations for the calculation of partial melting equilibria in metabasic rocks. Journal of Metamorphic Geology 34:845–869.
Hallett BW, Spear FS (2015) Monazite, zircon, and garnet growth in migmatitic pelites as a record of metamorphism and partial melting in the East Humboldt Range, Nevada. American Mineralogist 100:951–972.
Hallett BW, Spear FS (2014) The P–T History of Anatectic Pelites of the Northern East Humboldt Range, Nevada: Evidence for Tectonic Loading, Decompression, and Anatexis. Journal of Petrology 55:3–36.
Harley SL, Nandakumar V (2014) Accessory Mineral Behaviour in Granulite Migmatites: a Case Study from the Kerala Khondalite Belt, India. Journal of Petrology 55:1965–2002.
Harris N, Massey J (1994) Decompression and anatexis of Himalayan metapelites. Tectonics 13:1537–1546.
Harris NBW, Caddick M, Kosler J, et al (2004) The pressure-temperature-time path of migmatites from the Sikkim Himalaya: P-T-t path of migmatites, Sikkim Himalaya. Journal of Metamorphic Geology 22:249–264.
Hawthorne FC, Oberti R, Harlow GE, et al (2012) Nomenclature of the amphibole supergroup. American Mineralogist 97:2031–2048.
Herrmann UR, Nelson BK, Ratschbacher L (1994) The origin of a terrane: U/Pb zircon geochronology and tectonic evolution of the Xolapa complex (southern Mexico). Tectonics 13:455–474.
Holland T, Powell R (2003) Activity-composition relations for phases in petrological calculations: an asymmetric multicomponent formulation. Contributions to Mineralogy and Petrology 145:492–501.

Holland TJB, Powell R (2011) An improved and extended internally consistent thermodynamic dataset for phases of petrological interest, involving a new equation of state for solids. Journal of Metamorphic Geology 29:333–383.
Hollister LS (1993) The role of melt in the uplift and exhumation of orogenic belts. Chemical Geology 108:31–48.
Hoskin PWO, Black LP (2002) Metamorphic zircon formation by solid-state recrystallization of protolith igneous zircon. Journal of Metamorphic Geology 18:423–439.
Hoskin PWO, Schaltegger U (2003) The Composition of Zircon and Igneous and Metamorphic Petrogenesis. Reviews in Mineralogy and Geochemistry 53:27–62.
Johnson TE, Clark C, Taylor RJM, et al (2015) Prograde and retrograde growth of monazite in migmatites: An example from the Nagercoil Block, southern India. Geoscience Frontiers 6:373–387.
Jones KA, Brown M (1990) High-temperature "clockwise" P-T paths and melting in the development of regional migmatites: an example from southern Brittany, France. Journal of Metamorphic Geology 8:551–578.
Kelly NM, Clarke GL, Harley SL (2006) Monazite behaviour and age significance in poly-metamorphic high-grade terrains: A case study from the western Musgrave Block, central Australia. Lithos 88:100–134.
Kelsey DE, Clark C, Hand M (2008) Thermobarometric modelling of zircon and monazite growth in melt-bearing systems: examples using model metapelitic and metapsammitic granulites. Journal of Metamorphic Geology 26:199–212.
Kelsey DE, Clark C, Hand M, Collins AS (2006) Comment on "First report of garnet–corundum rocks from southern India: Implications for prograde high-pressure (eclogite-facies?) metamorphism." Earth and Planetary Science Letters 249:529–534.
Kelsey DE, Powell R (2011) Progress in linking accessory mineral growth and breakdown to major mineral evolution in metamorphic rocks: a thermodynamic approach in the Na2O-CaO-K2O-FeO-MgO-Al2O3-SiO2-H2O-TiO2-ZrO2 system. Journal of Metamorphic Geology 29:151–166.
Kohn MJ, Corrie SL, Markley C (2015) The fall and rise of metamorphic zircon. American Mineralogist 100:897–908.
Kohn MJ, Wieland MS, Parkinson CD, Upreti BN (2005) Five generations of monazite in Langtang gneisses: implications for chronology of the Himalayan metamorphic core. Journal of Metamorphic Geology 23:399–406.
Kohn MJ, Spear F (2000) Retrograde net transfer reaction insurance for pressure-temperature estimates. Geology 28(12): 1127–1130.
Kriegsman LM (2001) Partial melting, partial melt extraction and partial back reaction in anatectic migmatites. Lithos 56:75–96.
Kriegsman LM, Álvarez-Valero AM (2010) Melt-producing versus melt-consuming reactions in pelitic xenoliths and migmatites. Lithos 116:310–320.
Maldonado R, Ortega-Gutiérrez F, Hernández-Uribe D (2016) Garnet–chloritoid–paragonite metapelite from the Chuac us Complex (Central Guatemala): new evidence for continental subduction in the North America–Caribbean plate boundary. European Journal of Mineralogy 28:1169–1186.
Martini M, Mori L, Solari L, Centeno-García E (2011) Sandstone Provenance of the Arperos Basin (Sierra de Guanajuato, Central Mexico): Late Jurassic–Early Cretaceous Back-Arc Spreading as the Foundation of the Guerrero Terrane. The Journal of Geology.

Martini M, Solari L, Camprubí A (2013) Kinematics of the Guerrero terrane accretion in the Sierra de Guanajuato, central Mexico: new insights for the structural evolution of arc–continent collisional zones. International Geology Review 55:574–589.

Martini M, Solari L, López-Martínez M (2014) Correlating the Arperos Basin from Guanajuato, central Mexico, to Santo Tomás, southern Mexico: Implications for the paleogeography and origin of the Guerrero terrane. Geosphere 10:1385–1401.

Montel J-M, Weber C, Pichavant M (1986) Biotite-sillimanite-spinel assemblages in high-grade metamorphic rocks : occurrences, chemographic analysis and thermobarometric interest. Bulletin de Minéralogie 109:555–573.

Morán-Zenteno D (1992) Investigaciones isotópicas de Rb-Sr y Sm-Nd en rocas cristalinas de la región de Tierra Colorada- Acapulco-Cruz-Grande, Estado de Guerrero. PhD thesis. Universidad Nacional Autónoma de México.

Morán-Zenteno DJ, Corona-Chavez P, Tolson G (1996) Uplift and subduction erosion in southwestern Mexico since the Oligocene: pluton geobarometry constraints. Earth and Planetary Science Letters 141:51–65.

Morán-Zenteno DJ, Martiny BM, Solari L, et al (2018) Cenozoic magmatism of the Sierra Madre del Sur and tectonic truncation of the Pacific margin of southern Mexico. Earth-Science Reviews 183:85–114.

Mortensen JK, Hall BV, Bissig T, et al (2008) Age and Paleotectonic Setting of Volcanogenic Massive Sulfide Deposits in the Guerrero Terrane of Central Mexico: Constraints from U-Pb Age and Pb Isotope Studies. Economic Geology 103:117–140.

Mutch EJF, Blundy JD, Tattitch BC, et al (2016) An experimental study of amphibole stability in low-pressure granitic magmas and a revised Al-in-hornblende geobarometer. Contrib Mineral Petrol 171:85.

Ortega-Flores B, Solari L, Lawton TF, Ortega-Obregón C (2014) Detrital-zircon record of major Middle Triassic–Early Cretaceous provenance shift, central Mexico: demise of Gondwanan continental fluvial systems and onset of back-arc volcanism and sedimentation. International Geology Review 56:237–261.

Ortega-Gutiérrez F (1981) Metamorphic belts of southern Mexico and their tectonic significance. Geofísica Internacional 20(3).

Ortega-Gutiérrez F, Elías-Herrera M, Morán-Zenteno DJ, et al (2018) The pre-Mesozoic metamorphic basement of Mexico, 1.5 billion years of crustal evolution. Earth-Science Reviews 183:2–37.

Ouzegane K (2003) Prograde and Retrograde Evolution in High-temperature Corundum Granulites (FMAS and KFMASH Systems) from In Ouzzal Terrane (NW Hoggar, Algeria). Journal of Petrology 44:517–545.

Palin RM, Sayed AB, White RW, Mertz-Kraus R (2018) Origin, age, and significance of deep-seated granulite-facies migmatites in the Barrow zones of Scotland, Cairn Leuchan, Glen Muick area. Journal of Metamorphic Geology 36:1071–1096.

Patiño-Douce AE, Humphreys ED, Dana Johnston A (1990) Anatexis and metamorphism in tectonically thickened continental crust exemplified by the Sevier hinterland, western North America. Earth and Planetary Science Letters 97:290–315.

Patiño-Douce AE, Johnston AD (1991) Phase equilibria and melt productivity in the pelitic system: implications for the origin of peraluminous granitoids and aluminous granulites. Contributions to Mineralogy and Petrology 107:202–218.

Peña-Alonso TA, Estrada-Carmona J, Molina-Garza RS, et al (2017) Lateral spreading of the middle to lower crust inferred from Paleocene migmatites in the Xolapa Complex

(Puerto Escondido, Mexico): Gravitational collapse of a Laramide orogen? Tectonophysics 706–707:143–163.
Peña-Alonso TA, Molina-Garza RS, Villalobos-Escobar G, et al (2018) The opening and closure of the Jurassic-Cretaceous Xolapa basin, southern Mexico. Journal of South American Earth Sciences 88:599–620.
Pérez-Gutiérrez R, Solari LA, Gómez-Tuena A, et al (2009) Mesozoic geologic evolution of the Xolapa migmatitic complex north of Acapulco, southern Mexico: implications for paleogeographic reconstructions. Revista Mexicana de Ciencias Geológicas 26(1): 201–221.
Pidgeon RT (1992) Recrystallisation of oscillatory zoned zircon: some geochronological and petrological implications. Contributions to Mineralogy and Petrology 110:463–472. https://doi.org/10.1007/BF00344081
Pindell JL, Cande SC, Pitman WC, et al (1988) A plate-kinematic framework for models of Caribbean evolution. Tectonophysics 155:121–138.
Powell R, Holland TJB (2008) On thermobarometry. Journal of Metamorphic Geology 26:155–179.
Pyle JM, Spear FS (2003) Four generations of accessory-phase growth in low-pressure migmatites from SW New Hampshire. American Mineralogist 88:338–351.
Ratschbacher L, Riller U, Meschede M, et al (1991) Second look at suspect terranes in southern Mexico. Geology 19(12): 1233–1236.
Ratschbacher L, Franz L, Min M, et al (2009) The North American-Caribbean Plate boundary in Mexico-Guatemala-Honduras. Geological Society, London, Special Publications 328:219–293.
Regis D, Warren CJ, Young D, Roberts NMW (2014) Tectono-metamorphic evolution of the Jomolhari massif: Variations in timing of syn-collisional metamorphism across western Bhutan. Lithos 190–191:449–466.
Riller U, Ratschbacher L, Frisch W (1992) Left-lateral transtension along the Tierra Colorada deformation zone, northern margin of the Xolapa magmatic arc of southern Mexico. Journal of South American Earth Sciences 5:237–249.
Rocha BC, Moraes R, Möller A, et al (2017) Timing of anatexis and melt crystallization in the Socorro–Guaxupé Nappe, SE Brazil: Insights from trace element composition of zircon, monazite and garnet coupled to U Pb geochronology. Lithos 277:337–355.
Rosenberg CL, Handy MR (2005) Experimental deformation of partially melted granite revisited: implications for the continental crust. J Metamorph Geol 23:19–28.
Rushmer T (2001) Volume change during partial melting reactions: implications for melt extraction, melt geochemistry and crustal rheology. Tectonophysics 342:389–405.
Ryan PD, Dewey JF (2019) The sources of metamorphic heat during collisional orogeny: the Barrovian enigma. Can J Earth Sci 56:1309–1317.
Sawyer EW (2001) Melt segregation in the continental crust: distribution and movement of melt in anatectic rocks. Journal of Metamorphic Geology 19:291–309.
Sawyer EW (2008) Atlas of Migmatites. Canadian Science Publishing
Schaaf P, Morán-Zenteno D, Hernández-Bernal M del S, et al (1995) Paleogene continental margin truncation in southwestern Mexico: Geochronological evidence. Tectonics 14:1339–1350.
Schaltegger U, Fanning CM, Günther D, et al (1999) Growth, annealing and recrystallization of zircon and preservation of monazite in high-grade metamorphism: conventional and

in-situ U-Pb isotope, cathodoluminescence and microchemical evidence. Contrib Mineral Petrol 134:186–201.
Searle MP, Cottle JM, Streule MJ, Waters DJ (2009) Crustal melt granites and migmatites along the Himalaya: melt source, segregation, transport and granite emplacement mechanisms. Earth and Environmental Science Transactions of the Royal Society of Edinburgh 100:219–233.
Sengupta P, Sen J, Dasgupta S, et al (1999) Ultra-high Temperature Metamorphism of Metapelitic Granulites from Kondapalle, Eastern Ghats Belt: Implications for the Indo-Antarctic Correlation. Journal of Petrology 40:1065–1087.
Shulters JC, Bohlen SR (1989) The Stability of Hercynite and Hercynite-Gahnite Spinels in Corundum- or Quartz-Bearing Assemblages. Journal of Petrology 30:1017–1031.
Smith HA, Barreiro B (1990) Monazite U-Pb dating of staurolite grade metamorphism in pelitic schists. Contr Mineral and Petrol 105:602–615.
Smye AJ, Bickle MJ, Holland TJB, et al (2011) Rapid formation and exhumation of the youngest Alpine eclogites: A thermal conundrum to Barrovian metamorphism. Earth and Planetary Science Letters 306:193–204.
Solari LA, de Leon RT, Hernandez Pineda G, et al (2007) Tectonic significance of Cretaceous-Tertiary magmatic and structural evolution of the northern margin of the Xolapa Complex, Tierra Colorada area, southern Mexico. Geological Society of America Bulletin 119:1265–1279.
Soto JI, Platt JP (1999) Petrological and Structural Evolution of High-Grade Metamorphic Rocks from the Floor of the Alboran Sea Basin, Western Mediterranean. Journal of Petrology 40:21–60.
Spear FS, Kohn MJ, Cheney JT (1999) P - T paths from anatectic pelites. Contributions to Mineralogy and Petrology 134:17–32.
Stowell H, Tulloch A, Zuluaga C, Koenig A (2010) Timing and duration of garnet granulite metamorphism in magmatic arc crust, Fiordland, New Zealand. Chemical Geology 273:91–110.
Talavera-Mendoza O, Ruiz J, Corona-Chavez P, et al (2013) Origin and provenance of basement metasedimentary rocks from the Xolapa Complex: New constraints on the Chortis–southern Mexico connection. Earth and Planetary Science Letters 369–370:188–199.
Talavera-Mendoza O, Ruiz J, Díaz Duque LR, et al (2018) Early Tertiary extensional magmatism in southern Mexico and its relationship to exhumation of the Xolapa complex and detachment of the Chortis block. GSA Bulletin 130:796–810.
Tardy M, Lapierre H, Freydier C, et al (1994) The Guerrero suspect terrane (western Mexico) and coeval arc terranes (the Greater Antilles and the Western Cordillera of Colombia): a late Mesozoic intra-oceanic arc accreted to cratonal America during the Cretaceous. Tectonophysics 230:49–73.
Taylor RJM, Kirkland CL, Clark C (2016) Accessories after the facts: Constraining the timing, duration and conditions of high-temperature metamorphic processes. Lithos 264:239–257.
Teyssier C, Whitney DL (2002) Gneiss domes and orogeny. Geology 30(12):1139–1142.
Tolson G (2007) The Chacalapa fault, southern Oaxaca, México. In: Geology of México: Celebrating the Centenary of the Geological Society of México. Geological Society of America.

Vielzeuf D (2001) Melting relations in hydrous systems revisited: application to metapelites, metagreywackes and metabasalts. Contrib Mineral Petrol 141:251–267.

Vielzeuf D, Vidal P (1990) Granulites and Crustal Evolution. Springer Netherlands, Dordrecht

Viete DR, Oliver GJH, Fraser GL, et al (2013) Timing and heat sources for the Barrovian metamorphism, Scotland. Lithos 177:148–163.

Weinberg RF (2016) Himalayan leucogranites and migmatites: nature, timing and duration of anatexis. J Metamorph Geol 34:821–843.

Wheller CJ, Powell R (2014) A new thermodynamic model for sapphirine: calculated phase equilibria in K 2 O-FeO-MgO-Al 2 O 3 -SiO 2 -H 2 O-TiO 2 -Fe 2 O 3. J Meta Geol 32:287–299.

White, Powell, Holland, Worley (2000) The effect of TiO2 and Fe2O3 on metapelitic assemblages at greenschist and amphibolite facies conditions: mineral equilibria calculations in the system K2O-FeO-MgO-Al2O3-SiO2-H2O-TiO2-Fe2O3. J Metamorph Geol 18:497–511.

White RW (2003) Prograde Metamorphic Assemblage Evolution during Partial Melting of Metasedimentary Rocks at Low Pressures: Migmatites from Mt Stafford, Central Australia. Journal of Petrology 44:1937–1960.

White RW, Powell R (2002) Melt loss and the preservation of granulite facies mineral assemblages. J Metamorph Geol 20:621–632.

White RW, Powell R (2010) Retrograde melt-residue interaction and the formation of near-anhydrous leucosomes in migmatites. Journal of Metamorphic Geology 28:579–597.

White RW, Powell R, Clarke GL (2002) The interpretation of reaction textures in Fe-rich metapelitic granulites of the Musgrave Block, central Australia: constraints from mineral equilibria calculations in the system K2O-FeO-MgO-Al2O3-SiO2-H2O-TiO2-Fe2O3. Journal of Metamorphic Geology 20:41–55.

White RW, Powell R, Holland TJB, et al (2014a) New mineral activity-composition relations for thermodynamic calculations in metapelitic systems. Journal of Metamorphic Geology 32:261–286.

White RW, Powell R, Holland TJB (2007) Progress relating to calculation of partial melting equilibria for metapelites. J Metamorph Geol 25:511–527.

White RW, Powell R, Johnson TE (2014b) The effect of Mn on mineral stability in metapelites revisited: new a - x relations for manganese-bearing minerals. Journal of Metamorphic Geology 32:809–828.

Williams IS (2001) Response of detrital zircon and monazite, and their U–Pb isotopic systems, to regional metamorphism and host-rock partial melting, Cooma Complex, southeastern Australia. Australian Journal of Earth Sciences 48:557–580.

Yakymchuk C, Brown M (2014) Behaviour of zircon and monazite during crustal melting. Journal of the Geological Society 171:465–479.

Yakymchuk C, Brown M, Clark C, et al (2015) Decoding polyphase migmatites using geochronology and phase equilibria modelling. J Meta Geol 33:203–230.

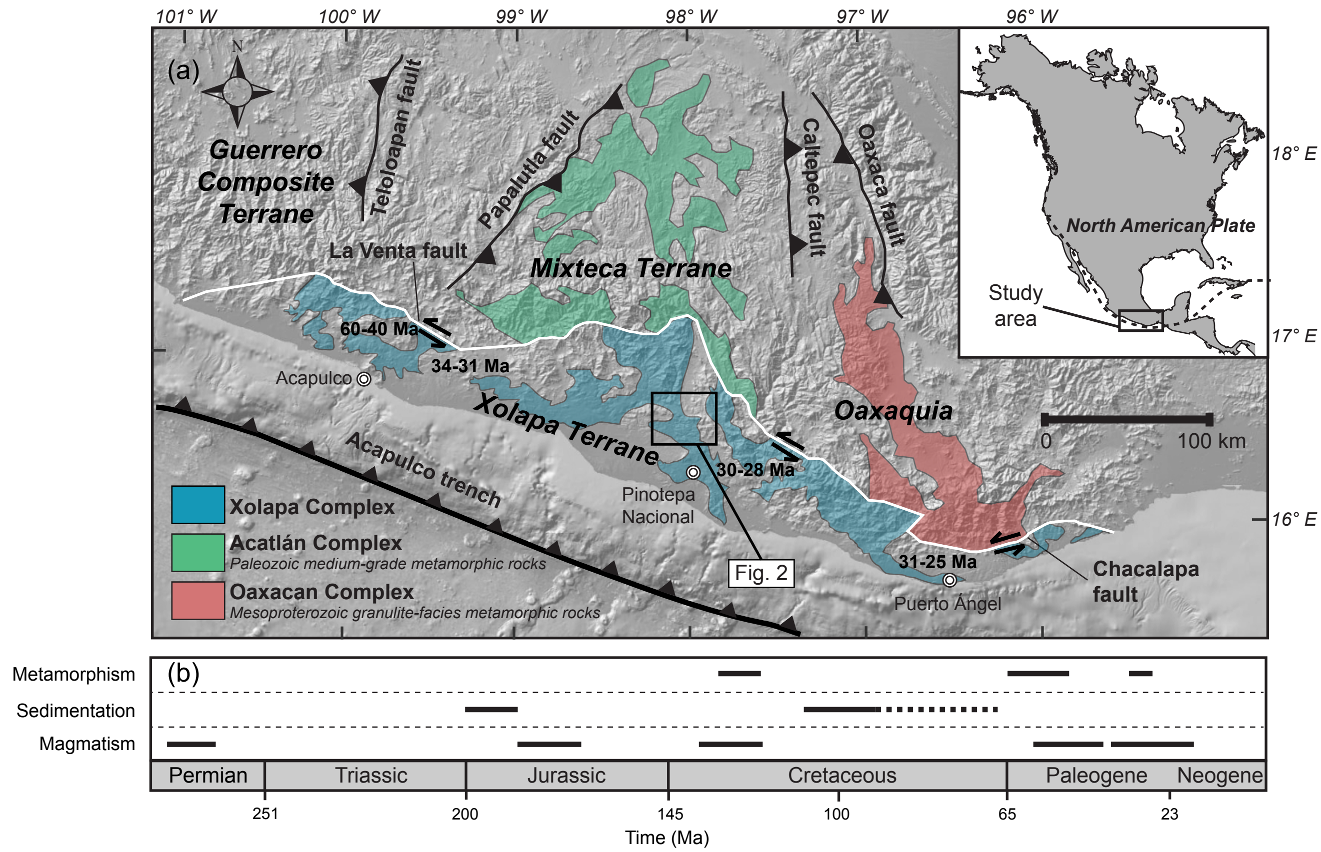


Figure 1. (a) Tectonic configuration of the North America plate boundary in southern Mexico showing the location of the Xolapa Complex and its relationship with other relevant basement units (after Ortega-Gutiérrez et al., 1999; Ortega-Gutiérrez et al., 2018). Age ranges (U–Pb zircon) indicate occurrence of Paleogene extension-related and Oligocene arc-related plutonic rocks intruding the complex (Herrmann et al., 1994; Ducea et al., 2004; Talavera-Mendoza et al., 2018). (b) Temporal framework of major geological events interpreted in the Xolapa Complex (after Herrmann et al., 1994; Morán et al., 1996; Ducea et al., 2004; Solari et al., 2007; Pérez-Gutiérrez et al., 2009; Talavera-Mendoza et al., 2013, Estrada-Carmona et al., 2016; Talavera-Mendoza et al., 2018; Peña-Alonso et al., 2018).

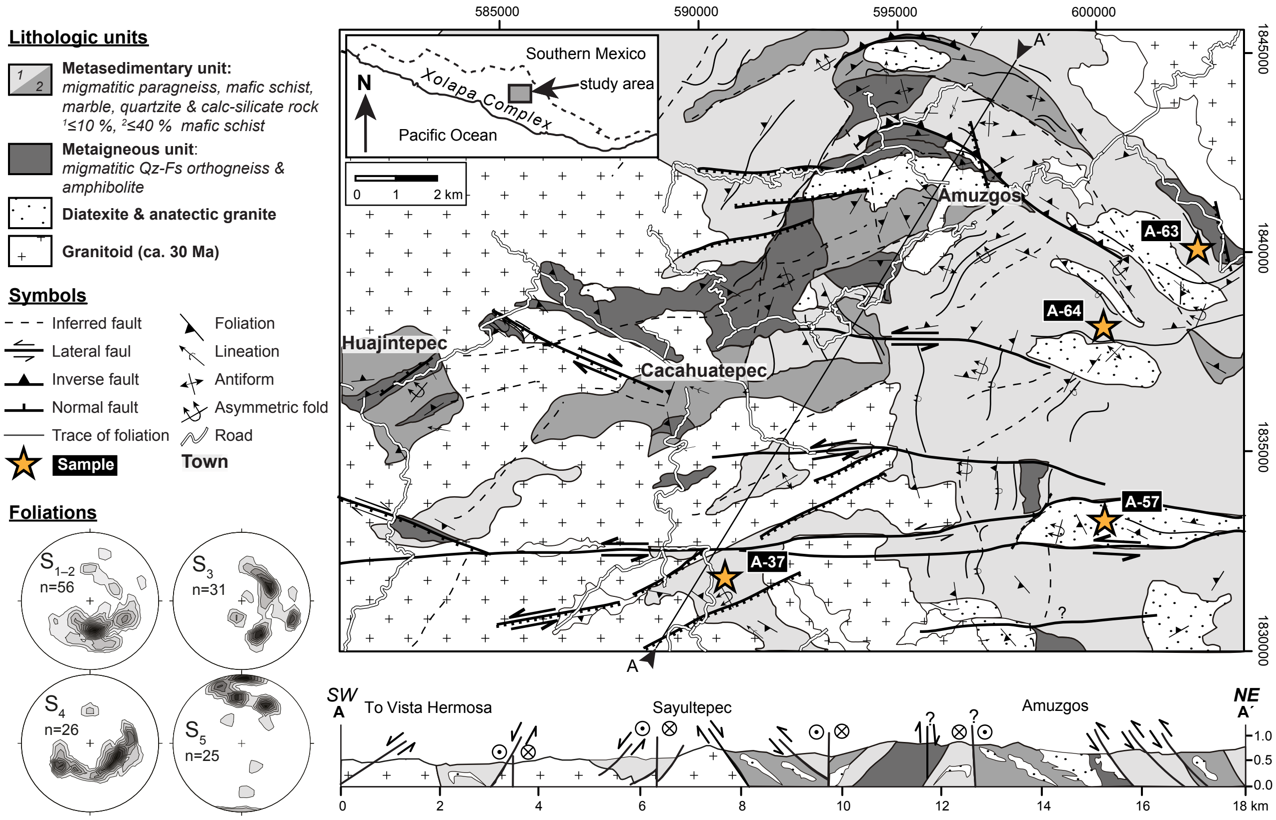


Figure 2. Geological map and cross section of the study area showing the distribution of the metasedimentary and metaigneous units. Study sample locations are indicated by stars. Stereographic projections show the orientation of S1 to S5 planar structures following criteria proposed by Corona-Chávez et al. (2006). S1–S2: metamorphic to early-stage anatectic foliation; S3: late-stage anatectic (diatexitic) foliation; S4–S5: post-anatectic axial and mylonitic planes.

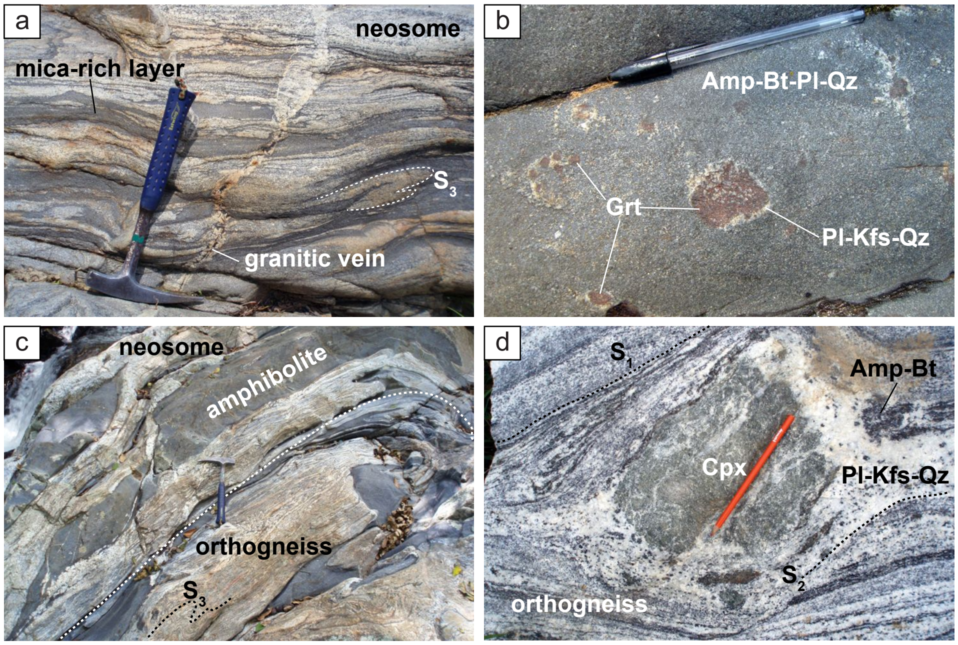


Figure 3. Outcrop features of the main rock types belonging to the metasedimentary (a–b) and metaigneous (c–d) units of central Xolapa Complex. (a) Typical outcrop-scale stromatic layering in migmatitic paragneiss. Note neosome folding (center right), and granitic vein crosscutting the layering. (b) Garnet-bearing mafic schist showing centimeter-sized garnet porphyroblasts with leucocratic coronae (leucosome). (c) Folded migmatitic quartzofeldspathic orthogneiss hosting dismembered amphibolite layers. (d) Centimeter-sized leucosome pod including a clinopyroxene megacryst in a migmatitic quartzofeldspathic orthogneiss. Hammer and pen/pencil length are 30 and 15 cm, respectively.

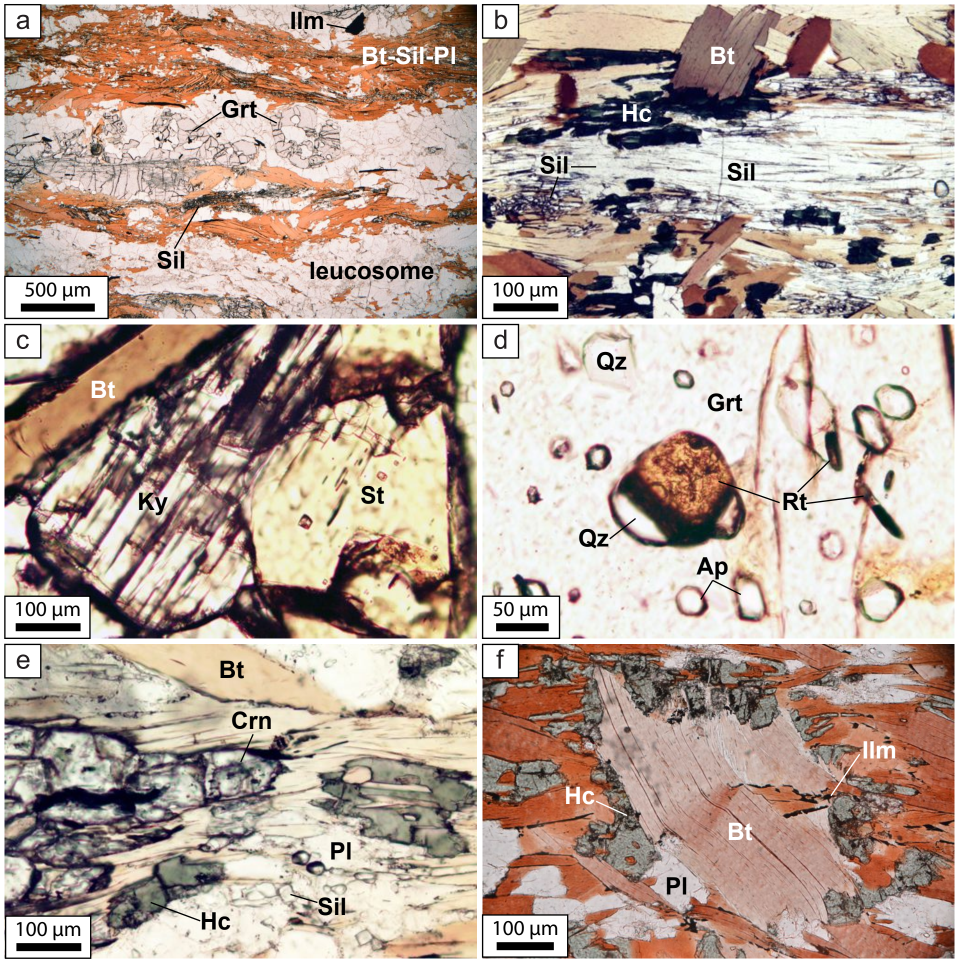


Figure 4. Petrographic features of studied migmatitic paragneisses (A37 and A57). (a) Stromatic layering at thin-section scale. Garnet can occur both in leucosome and cleavage domain. (b) Detail showing typical microstructures and mineral assemblages in cleavage domains. (c-d) Relic inclusions of biotite, kyanite, staurolite and rutile in garnet porphyroblast. (e) Subhedral poikiloblastic corundum associated with biotite, plagioclase, and hercynite. (f) Late-melting-stage hercynite replacing crenulated biotite porphyroblast.

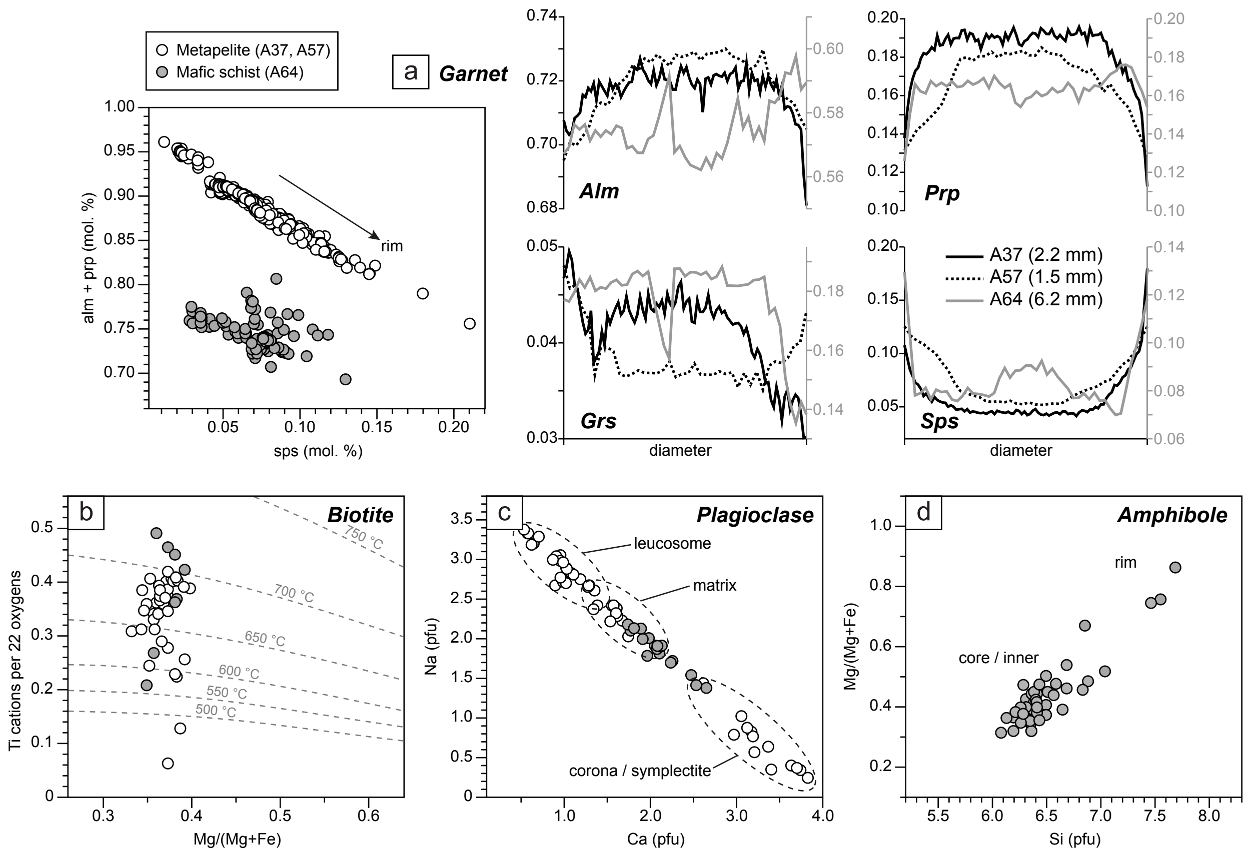


Figure 5. Composition of garnet (a), biotite (b), plagioclase (c), and amphibole (d) from the studied samples. Garnet plots include rim-to-rim compositional (mole fraction) profiles of representative grains (with diameters indicated in the legend) from the studied samples. Biotite is plotted on the *X*Mg versus Ti cations pfu (for 22 oxygen) diagram of Henry *et al*. (2005). Dashed ellipses in (c) refer to the textural setting of plagioclase from metapelite samples.

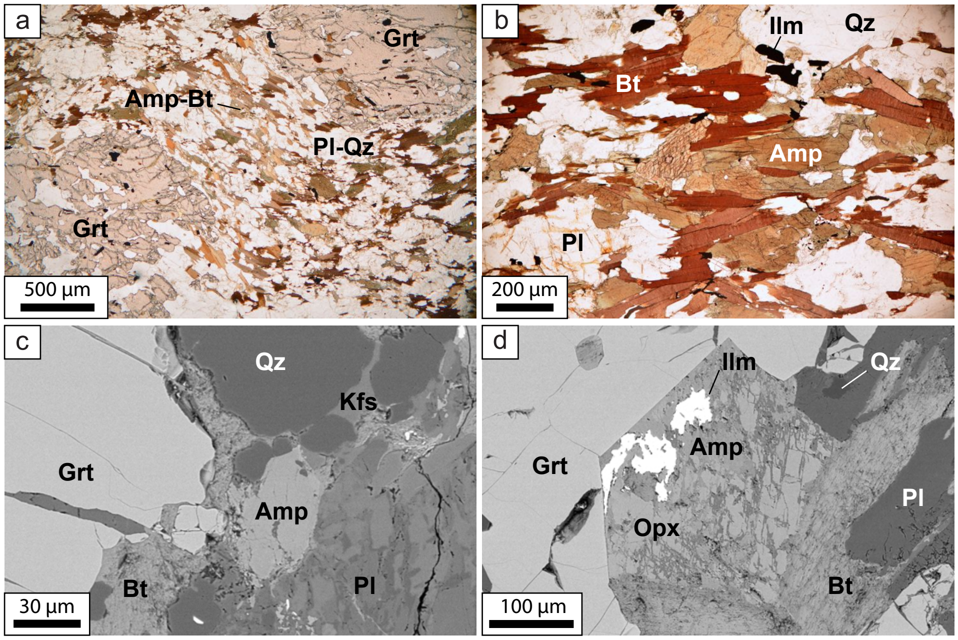


Figure 6. Petrographic features of garnet-bearing mafic schist intercalated within migmatitic paragneiss. (a) Garnet porphyroblasts set in a matrix of aligned amphibole, biotite, plagioclase and quartz. (b) Detail of matrix microstructures and assemblages. (c) Backscattered electron image (BSE) showing a in-situ leucosome patch with K-feldspar forming cuspate boundaries between rounded quartz and plagioclase. (d) Embayment of orthopyroxene and ilmenite, associated with corroded grains of amphibole and biotite, in a garnet porphyroblast.

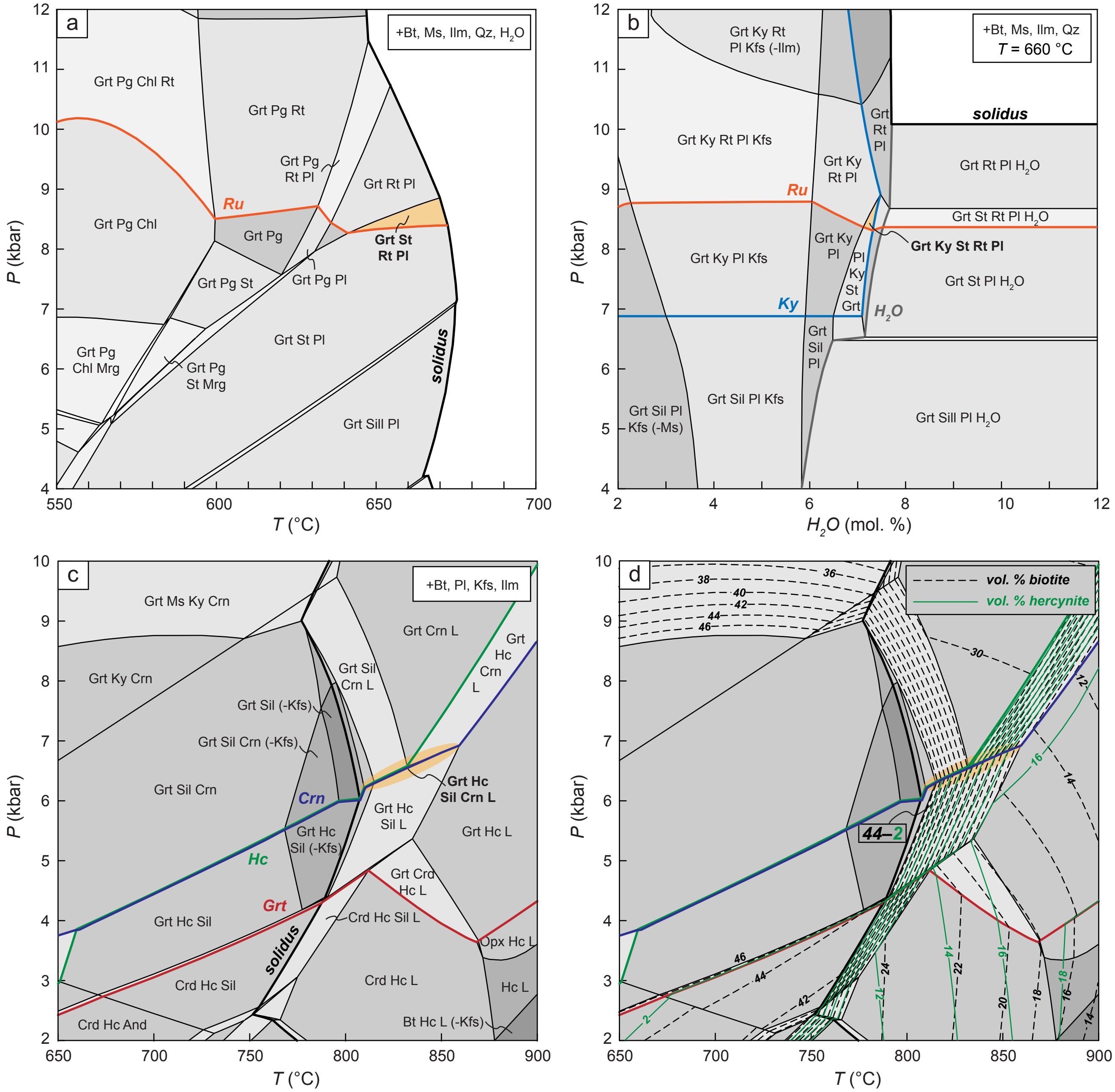


Figure 7. Equilibrium phase diagrams calculated for the studied metapelite (A37, A57) and mafic schist (A64) samples. Stability boundaries of relevant phases are indicated in each case by thick lines and bold-italic text. (a, b) Calculations for the metapelite A37 at subsolidus conditions. Assemblage fields labeled with bold text (orange shading) constrain the likely P–T conditions of equilibration of the relic assemblage preserved within garnet porphyroblasts. (c, d) P–T phase diagrams calculated for the corundum-bearing metapelite A57. Highlighted field (orange ellipse and bold text) indicate the likely P–T conditions over which the sample equilibrated during peak metamorphism. Black-dashed and green lines represent the calculated modal proportions of biotite and hercynite, respectively. (e, f) Calculations for the garnet-bearing mafic schist A64 showing the likely P–T conditions at which the sample attained peak metamorphism upon crossing the solidus. Variation of biotite and melt modal abundances are indicated by black-dashed and white lines, respectively.

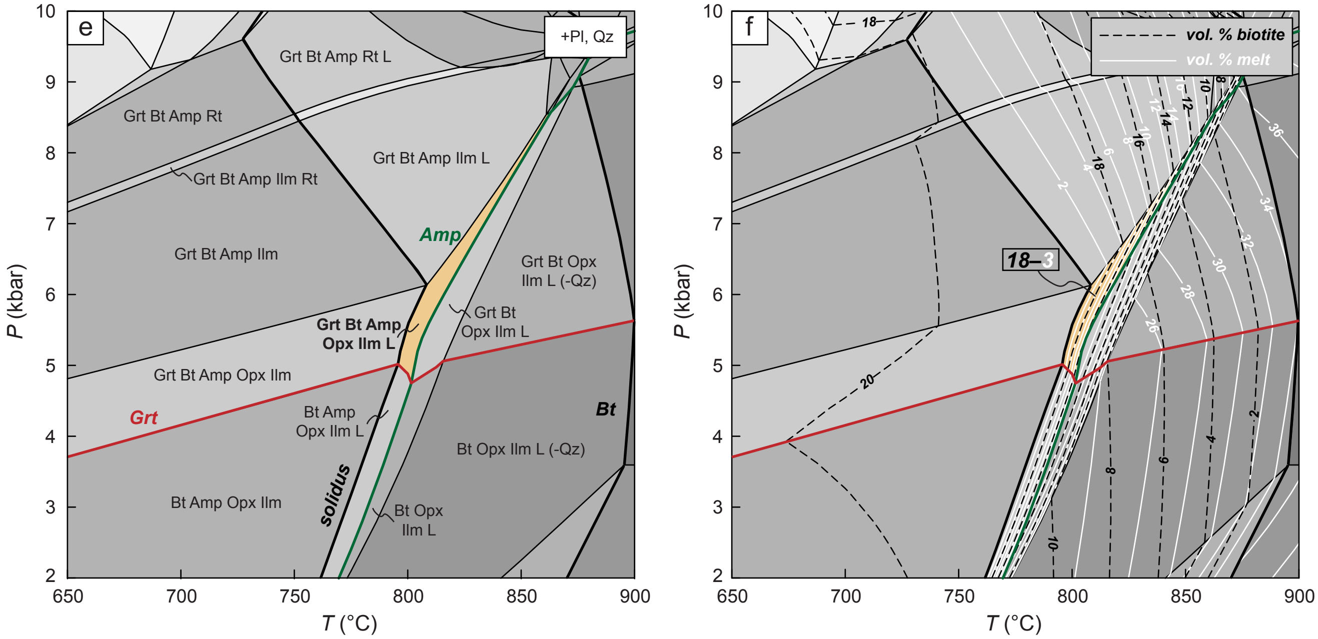
e
+Pl, Qz
Grt Bt Amp Rt L
Grt Bt Amp Rt
Grt Bt Amp Ilm Rt
Grt Bt Amp Ilm L
Grt Bt Amp Ilm
Amp
Grt Bt Opx
Ilm L (-Qz)
Grt Bt Amp
Opx Ilm L
Grt Bt
Opx Ilm L
Grt Bt Amp Opx Ilm
Grt
Bt Amp
Opx Ilm L
Bt
Bt Opx Ilm L (-Qz)
Bt Amp Opx Ilm
solidus
Bt Opx
Ilm L
P (kbar)
T (°C)
f
vol. % biotite
vol. % melt
18–3

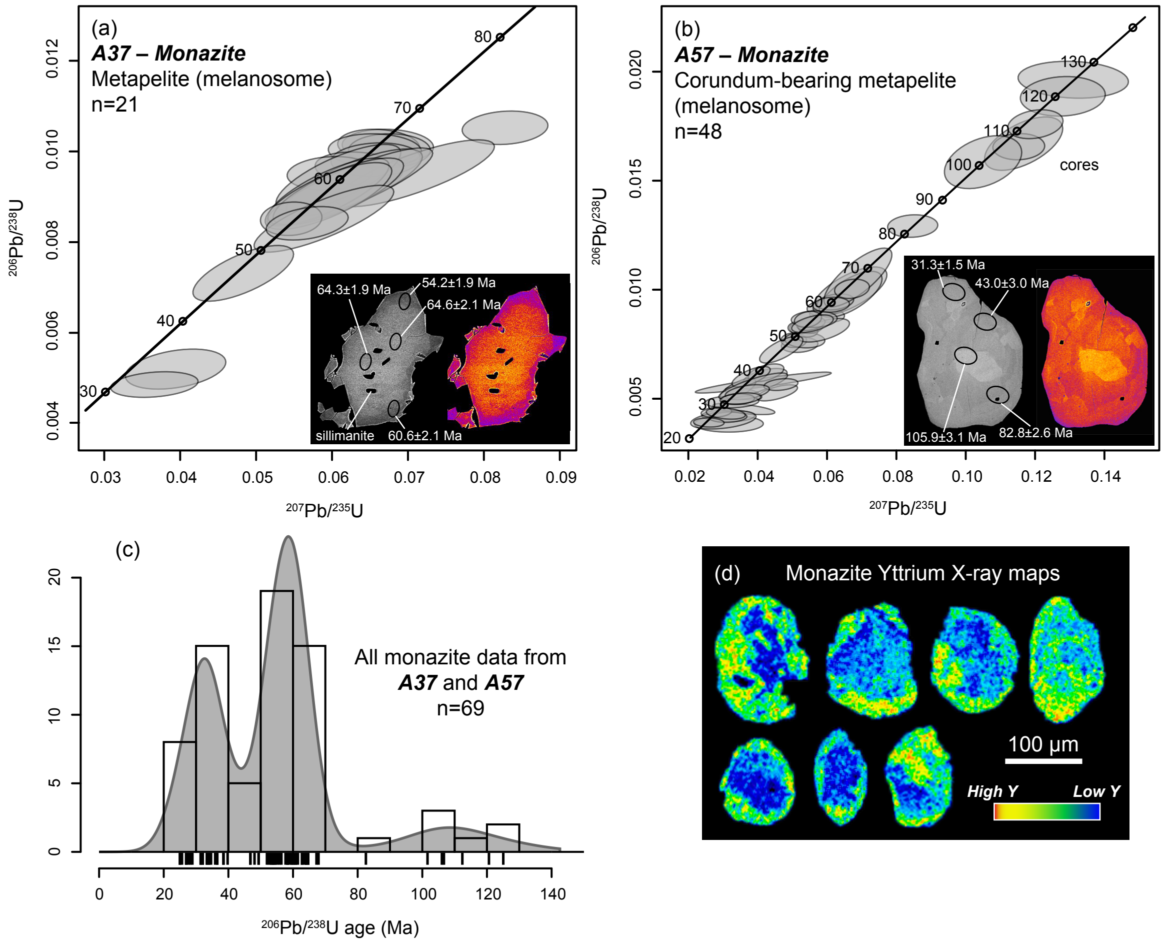


Figure 8. Monazite reults from central Xolapa Complex metapelites. (a, b) Wetherill concordia diagrams for samples A37 and A57, respectively, plotted with 2σ error ellipses. Insets show examples (BSE images) of typical grain morphologies and zoning patterns, as well as locations of laser spots (black ellipses) over different internal domains and their corresponding age. (c) Kernel density estimate (KDE) plot for all monazite data, which suggest three main age populations for the studied metapelites. (d) X-ray maps showing the distribution of Y in monazite from the studied samples. Note that Y concentration correlates inversely with BSE emission in (a) and (b).

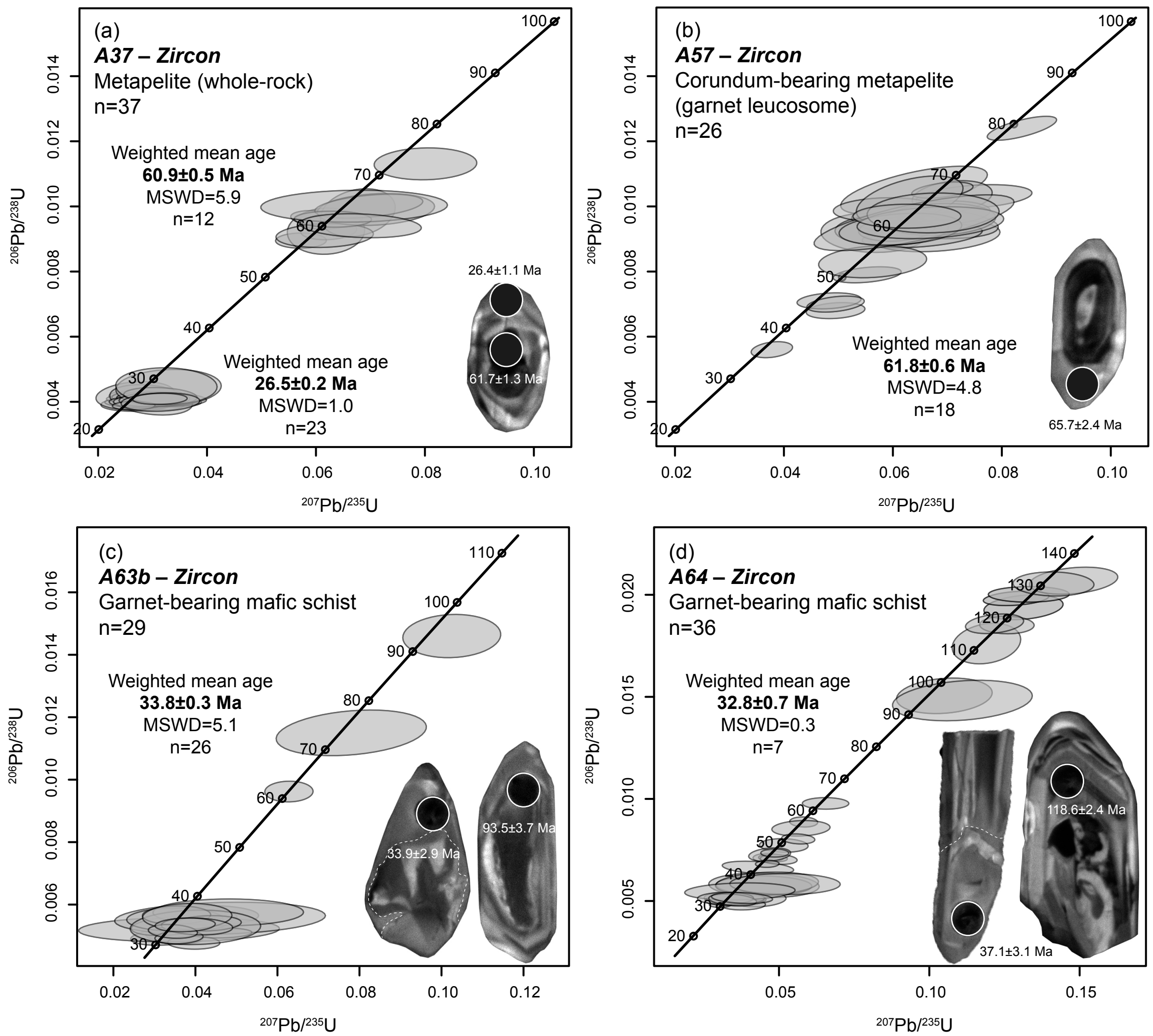


Figure 9. Zircon reults from central Xolapa Complex metapelites and associated garnet-bearing mafic schist. (a–d) Wetherill concordia diagrams for metapelites A37 (a) and A57 (b), and mafic schist A63b (c) and A64 (d) plotted with 2σ error ellipses. Insets show examples (CL images) of typical grain morphologies and zoning patterns, as well as locations of laser spots (white rings) over different internal domains together with their corresponding age.

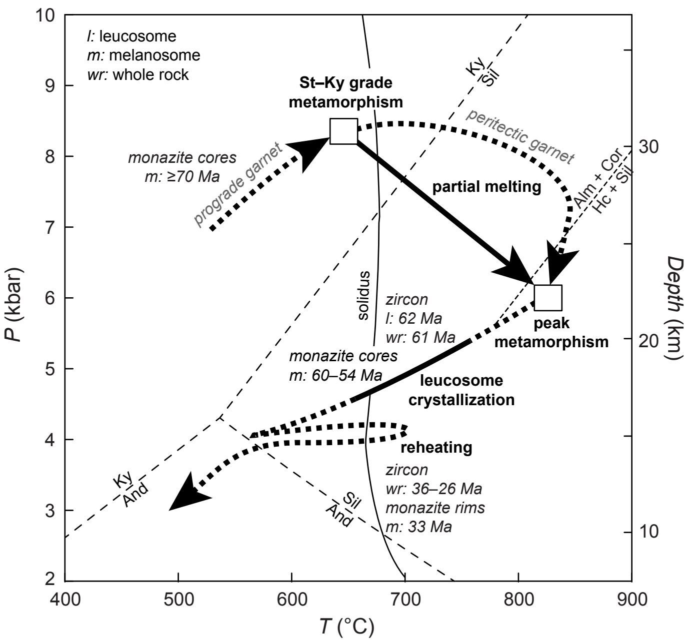


Figure 10. *P–T*–t path for central Xolapa Complex. Dashed portions of the path are not well constrained. Squares represent *P–T* estimates from relic prograde (A37) and peak (A57, A64) assemblages. Age ranges given are based on density peaks (KDE) shown in Fig. 11. Leucosome crystallization stage is based on Ti-in-zircon thermometry. Possible Eocene–Oligocene reheating event is shown according to recalculated Al-in-hornblende barometry after Morán-Zenteno et al. (1996). Relevant mineral stability limits and solidus estimate are also shown as reference.

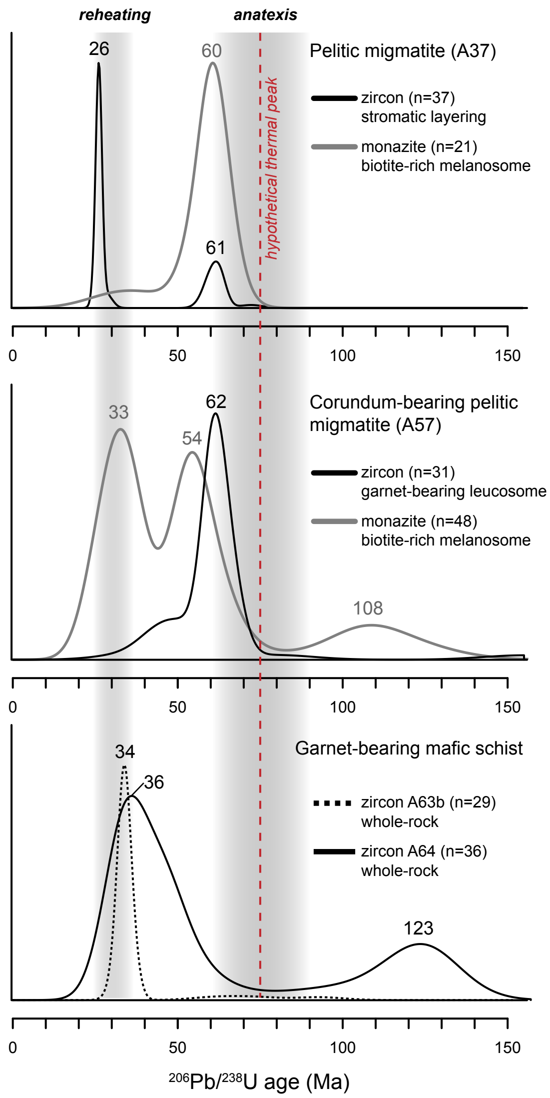


Figure 11. Comparative KDE diagrams from zircon and monazite in alternating metapelites and metabasites from the central Xolapa Complex. Metapelite data shows density peak heights of zircon attributed to the neosome crystallization stage, followed by a large peak on the retrograde path as new zircon grows/reset during a subsequent reheating event. Monazite shows both late-anatectic and retrograde growth, as well as a probable prograde generation. Metabasites show density peak heights of zircon related to late-stage growth/modification and variable resetting of protolith grains. Interpretative satages of anatexis, thermal peak and reheating are also shown.

Table 1. Representative mineral compositions from the studied samples. Alm=$Fe^{2+}$/($Fe^{2+}$+Mn+Mg+Ca); Sps=Mn/($Fe^{2+}$+Mn+Mg+Ca); Prp=Mg/($Fe^{2+}$+Mn
$X_{Mg}$=Mg/(Mg+$Fe^{2+}$); An=Ca/(Na+Ca+K); Ab=Na/(Na+Ca+K); Or=K/(Na+Ca+K). Staurolite data correspond to energy-dispersive X-ray spectroscopy (EDS

| **Sample** | A37-56 | A37-92 | A57-106 | A57-201 | A37-2 | A37-3 | A57-2 | A57-3 | A37-1 | A37-19 | A57-9 | A57-15 | A37-3 | A37-16 | A57-3 | A57-9 |
|---|---|---|---|---|---|---|---|---|---|---|---|---|---|---|---|---|
| **Mineral** | Grt | Grt | Grt | Grt | Hc | Hc | Hc | Hc | Bt | Bt | Bt | Bt | Pl | Pl | Pl | Pl |
| **Location** | core | rim | core | rim | matrix | matrix | matrix | matrix | matrix | matrix | matrix | matrix | matrix | matrix | matrix | matrix |
| **Oxides (wt. %)** | | | | | | | | | | | | | | | | |
| **$SiO_2$** | 38.56 | 37.88 | 36.84 | 37.70 | 0.00 | 0.04 | 0.02 | 0.02 | 34.19 | 34.60 | 34.11 | 34.61 | 65.03 | 56.19 | 49.40 | 59.64 |
| **$TiO_2$** | 0.01 | 0.00 | 0.00 | 0.01 | 0.04 | 0.08 | 0.02 | 0.05 | 2.34 | 3.21 | 3.54 | 2.06 | 0.09 | 0.00 | 0.00 | 0.00 |
| **$Al_2O_3$** | 21.99 | 22.11 | 22.89 | 21.39 | 58.59 | 58.17 | 59.22 | 59.56 | 19.04 | 19.63 | 20.42 | 20.74 | 21.10 | 27.99 | 31.15 | 25.95 |
| **FeO** | 33.67 | 31.33 | 31.49 | 32.10 | 37.10 | 37.06 | 36.41 | 36.44 | 22.49 | 22.73 | 20.81 | 21.48 | 0.16 | 0.26 | 0.24 | 0.03 |
| **MnO** | 1.93 | 8.21 | 3.23 | 6.41 | 1.06 | 1.01 | 0.77 | 0.85 | 0.34 | 0.33 | 0.30 | 0.42 | 0.02 | 0.00 | 0.01 | 0.00 |
| **MgO** | 5.03 | 2.92 | 4.32 | 2.40 | 2.82 | 2.96 | 3.06 | 2.97 | 7.51 | 7.30 | 6.95 | 6.56 | 0.00 | 0.00 | 0.00 | 0.00 |
| **CaO** | 1.64 | 1.09 | 1.35 | 1.51 | 0.01 | 0.03 | 0.01 | 0.01 | 0.02 | 0.02 | 0.00 | 0.29 | 3.03 | 9.34 | 15.46 | 7.27 |
| **$Na_2O$** | 0.00 | 0.00 | 0.00 | 0.00 | 0.00 | 0.00 | 0.00 | 0.00 | 0.29 | 0.25 | 0.18 | 0.50 | 9.67 | 6.01 | 2.86 | 7.11 |
| **$K_2O$** | 0.00 | 0.00 | 0.00 | 0.00 | 0.00 | 0.00 | 0.00 | 0.00 | 9.32 | 9.28 | 9.73 | 9.23 | 0.08 | 0.10 | 0.04 | 0.42 |
| **ZnO** | 0.00 | 0.00 | 0.00 | 0.00 | 1.10 | 1.01 | 1.96 | 2.15 | 0.00 | 0.00 | 0.00 | 0.00 | 0.00 | 0.00 | 0.00 | 0.00 |
| **Total** | 102.83 | 103.54 | 100.12 | 101.52 | 100.72 | 100.35 | 101.47 | 102.05 | 95.54 | 97.35 | 96.04 | 95.89 | 99.17 | 99.89 | 99.15 | 100.42 |
| | | | | | | | | | | | | | | | | |
| **Cations (pfu)** | | | | | | | | | | | | | | | | |
| **Si** | 5.97 | 5.92 | 5.85 | 6.00 | 0.00 | 0.00 | 0.00 | 0.00 | 2.70 | 2.68 | 2.69 | 2.73 | 11.55 | 9.79 | 9.12 | 10.26 |
| **Ti** | 0.00 | 0.00 | 0.00 | 0.00 | 0.00 | 0.00 | 0.00 | 0.00 | 0.14 | 0.19 | 0.21 | 0.12 | 0.00 | 0.00 | 0.00 | 0.00 |
| **Al** | 4.01 | 4.07 | 4.29 | 4.01 | 1.96 | 1.96 | 1.94 | 1.96 | 1.77 | 1.79 | 1.90 | 1.93 | 4.42 | 5.75 | 6.77 | 5.26 |
| **$Fe^{3+}$** | 0.02 | 0.00 | 0.00 | 0.00 | 0.04 | 0.05 | 0.00 | 0.00 | 0.00 | 0.00 | 0.00 | 0.00 | 0.00 | 0.00 | 0.00 | 0.00 |
| **$Fe^{2+}$** | 4.36 | 4.10 | 4.18 | 4.27 | 0.84 | 0.84 | 0.85 | 0.85 | 1.48 | 1.47 | 1.37 | 1.42 | 0.02 | 0.04 | 0.04 | 0.00 |
| **Mn** | 0.25 | 1.09 | 0.44 | 0.86 | 0.03 | 0.02 | 0.02 | 0.02 | 0.02 | 0.02 | 0.02 | 0.03 | 0.00 | 0.00 | 0.00 | 0.00 |
| **Mg** | 1.16 | 0.68 | 1.02 | 0.57 | 0.12 | 0.13 | 0.13 | 0.12 | 0.88 | 0.84 | 0.82 | 0.77 | 0.00 | 0.00 | 0.00 | 0.00 |
| **Ca** | 0.27 | 0.18 | 0.23 | 0.26 | 0.00 | 0.00 | 0.00 | 0.00 | 0.00 | 0.00 | 0.00 | 0.02 | 0.58 | 1.74 | 3.06 | 1.34 |
| **Na** | 0.00 | 0.00 | 0.00 | 0.00 | 0.00 | 0.00 | 0.00 | 0.00 | 0.04 | 0.04 | 0.03 | 0.08 | 3.33 | 2.03 | 1.02 | 2.37 |
| **K** | 0.00 | 0.00 | 0.00 | 0.00 | 0.00 | 0.00 | 0.00 | 0.00 | 0.94 | 0.92 | 0.98 | 0.93 | 0.02 | 0.02 | 0.01 | 0.09 |
| **Zn** | 0.00 | 0.00 | 0.00 | 0.00 | 0.02 | 0.02 | 0.04 | 0.04 | 0.00 | 0.00 | 0.00 | 0.00 | 0.00 | 0.00 | 0.00 | 0.00 |
| **Sum** | 16.02 | 16.04 | 16.01 | 15.99 | 3.02 | 3.02 | 2.98 | 2.99 | 7.99 | 7.96 | 8.01 | 8.03 | 19.91 | 19.37 | 20.01 | 19.34 |
| **Oxygens** | 24 | 24 | 24 | 24 | 4 | 4 | 4 | 4 | 11 | 11 | 11 | 11 | 32 | 32 | 32 | 32 |
| | | | | | | | | | | | | | | | | |
| **Alm** | 0.19 | 0.11 | 0.17 | 0.10 | – | – | – | – | – | – | – | – | – | – | – | – |
| **Sps** | 0.72 | 0.68 | 0.71 | 0.72 | – | – | – | – | – | – | – | – | – | – | – | – |
| **Prp** | 0.04 | 0.03 | 0.04 | 0.04 | – | – | – | – | – | – | – | – | – | – | – | – |
| **Grs** | 0.04 | 0.18 | 0.07 | 0.14 | – | – | – | – | – | – | – | – | – | – | – | – |
| **$X_{Mg}$** | – | – | – | – | 0.12 | 0.13 | 0.13 | 0.13 | 0.37 | 0.36 | 0.37 | 0.35 | – | – | – | – |
| **An** | – | – | – | – | – | – | – | – | – | – | – | – | 14.70 | 45.92 | 74.75 | 35.23 |
| **Ab** | – | – | – | – | – | – | – | – | – | – | – | – | 84.87 | 53.47 | 25.02 | 62.35 |
| **Or** | – | – | – | – | – | – | – | – | – | – | – | – | 0.43 | 0.61 | 0.23 | 2.41 |

ı+Mg+Ca); Grs=Ca/($Fe^{2+}$+Mn+Mg+Ca);
3) analys

| A37-4 | A37-1 | A37-3 | A37-4 |
|---|---|---|---|
| Kfs | St | St | St |
| matrix | inclusior | nclusior | inclusion |
| | | | |
| 64.82 | 29.12 | 29.35 | 29.85 |
| 0.00 | 0.00 | 1.21 | 0.00 |
| 18.60 | 53.17 | 52.38 | 54.39 |
| 0.05 | 14.21 | 13.85 | 12.98 |
| 0.00 | 0.00 | 0.00 | 0.00 |
| 0.00 | 2.09 | 2.06 | 2.28 |
| 0.03 | 0.00 | 0.00 | 0.00 |
| 0.84 | 0.95 | 0.44 | 0.00 |
| 14.76 | 0.46 | 0.71 | 0.50 |
| 0.00 | 0.00 | 0.00 | 0.00 |
| 99.10 | 100.00 | 100.00 | 100.00 |
| | | | |
| 12.00 | 3.98 | 4.00 | 4.03 |
| 0.00 | 0.00 | 0.12 | 0.00 |
| 4.06 | 8.56 | 8.42 | 8.65 |
| 0.00 | 0.00 | 0.00 | 0.00 |
| 0.01 | 1.62 | 1.58 | 1.46 |
| 0.00 | 0.00 | 0.00 | 0.00 |
| 0.00 | 0.43 | 0.42 | 0.46 |
| 0.01 | 0.00 | 0.00 | 0.00 |
| 0.30 | 0.25 | 0.12 | 0.00 |
| 3.49 | 0.08 | 0.12 | 0.09 |
| 0.00 | 0.00 | 0.00 | 0.00 |
| 19.86 | 14.91 | 14.78 | 14.69 |
| 32 | 23 | 23 | 23 |
| | | | |
| – | – | – | – |
| – | – | – | – |
| – | – | – | – |
| – | – | – | – |
| – | 0.21 | 0.21 | 0.24 |
| 0.13 | – | – | – |
| 7.96 | – | – | – |
| 91.91 | – | – | – |

Table 1. (Continued)

| **Sample** | B63b-1 | B63b-3 | A64-1 | A64-4 | A63b-1 | A64-2 | A64-4 | A64-5 | A63b-1 | A63b-5 | 64-5 |
|---|---|---|---|---|---|---|---|---|---|---|---|
| **Mineral** | Grt | Grt | Grt | Grt | Bt | Bt | Bt | Bt | Pl | Pl | Pl |
| **Location** | rim | core | rim | core | matrix | matrix | matrix | matrix | matrix | matrix | matrix |
| **Oxides (wt. %)** | | | | | | | | | | | |
| **$SiO_2$** | 38.53 | 38.69 | 38.82 | 38.78 | 34.73 | 36.32 | 36.35 | 37.95 | 55.85 | 57.00 | 52.97 |
| **$TiO_2$** | 0.00 | 0.10 | 0.03 | 0.03 | 3.99 | 3.07 | 3.81 | 2.37 | 0.00 | 0.08 | 0.00 |
| **$Al_2O_3$** | 22.02 | 22.16 | 21.62 | 21.72 | 15.94 | 15.01 | 14.62 | 16.67 | 27.80 | 28.17 | 30.15 |
| **FeO** | 28.13 | 27.88 | 30.14 | 29.93 | 24.22 | 24.76 | 24.28 | 22.09 | 0.12 | 0.07 | 0.47 |
| **MnO** | 3.50 | 3.50 | 1.89 | 2.03 | 0.29 | 0.19 | 0.18 | 0.12 | 0.00 | 0.00 | 0.08 |
| **MgO** | 3.30 | 3.21 | 2.73 | 2.77 | 8.96 | 8.01 | 8.05 | 10.11 | 0.00 | 0.02 | 0.02 |
| **CaO** | 6.56 | 7.07 | 7.50 | 7.30 | 0.94 | 0.07 | 0.05 | 0.12 | 10.38 | 9.12 | 13.12 |
| **$Na_2O$** | 0.00 | 0.00 | 0.00 | 0.00 | 0.21 | 0.12 | 0.21 | 0.14 | 5.81 | 6.32 | 4.05 |
| **$K_2O$** | 0.00 | 0.00 | 0.00 | 0.00 | 7.08 | 9.22 | 9.07 | 7.40 | 0.15 | 0.16 | 0.05 |
| **ZnO** | 0.00 | 0.00 | 0.00 | 0.00 | 0.00 | 0.00 | 0.00 | 0.00 | 0.02 | 0.00 | 0.04 |
| **Total** | 102.04 | 102.61 | 102.73 | 102.56 | 96.36 | 96.77 | 96.62 | 96.97 | 100.12 | 100.93 | 100.95 |
| | | | | | | | | | | | |
| **Cations (pfu)** | | | | | | | | | | | |
| **Si** | 5.99 | 5.98 | 6.02 | 6.02 | 2.69 | 2.85 | 2.86 | 2.86 | 9.95 | 10.14 | 9.54 |
| **Ti** | 0.00 | 0.01 | 0.00 | 0.00 | 0.23 | 0.18 | 0.23 | 0.13 | 0.00 | 0.00 | 0.00 |
| **Al** | 4.03 | 4.03 | 3.95 | 3.97 | 1.46 | 1.39 | 1.36 | 1.48 | 6.05 | 5.91 | 6.40 |
| **$Fe^{3+}$** | 0.00 | 0.00 | 0.05 | 0.03 | 0.00 | 0.00 | 0.00 | 0.00 | 0.00 | 0.00 | 0.00 |
| **$Fe^{2+}$** | 3.66 | 3.60 | 3.91 | 3.88 | 1.57 | 1.63 | 1.60 | 1.39 | 0.02 | 0.01 | 0.07 |
| **Mn** | 0.46 | 0.46 | 0.25 | 0.27 | 0.02 | 0.01 | 0.01 | 0.01 | 0.00 | 0.00 | 0.00 |
| **Mg** | 0.76 | 0.74 | 0.63 | 0.64 | 1.03 | 0.94 | 0.94 | 1.13 | 0.00 | 0.00 | 0.00 |
| **Ca** | 1.09 | 1.17 | 1.25 | 1.21 | 0.08 | 0.01 | 0.00 | 0.01 | 1.98 | 1.74 | 2.53 |
| **Na** | 0.00 | 0.00 | 0.00 | 0.00 | 0.03 | 0.02 | 0.03 | 0.02 | 2.01 | 2.18 | 1.41 |
| **K** | 0.00 | 0.00 | 0.00 | 0.00 | 0.70 | 0.92 | 0.91 | 0.71 | 0.03 | 0.04 | 0.01 |
| **Zn** | 0.00 | 0.00 | 0.00 | 0.00 | 0.00 | 0.00 | 0.00 | 0.00 | 0.00 | 0.00 | 0.00 |
| **Sum** | 15.99 | 15.99 | 16.00 | 15.99 | 7.81 | 7.95 | 7.95 | 7.74 | 20.04 | 20.01 | 19.97 |
| **Oxygens** | 24 | 24 | 24 | 24 | 11 | 11 | 11 | 11 | 32 | 32 | 32 |
| | | | | | | | | | | | |
| **Alm** | 0.13 | 0.12 | 0.10 | 0.11 | – | – | – | – | – | – | – |
| **Sps** | 0.61 | 0.60 | 0.65 | 0.65 | – | – | – | – | – | – | – |
| **Prp** | 0.18 | 0.20 | 0.21 | 0.20 | – | – | – | – | – | – | – |
| **Grs** | 0.08 | 0.08 | 0.04 | 0.04 | – | – | – | – | – | – | – |
| **$X_{Mg}$** | – | – | – | – | 0.40 | 0.37 | 0.37 | 0.45 | – | – | – |
| **An** | – | – | – | – | – | – | – | – | 49.27 | 43.96 | 63.98 |
| **Ab** | – | – | – | – | – | – | – | – | 49.90 | 55.13 | 35.74 |
| **Or** | – | – | – | – | – | – | – | – | 0.83 | 0.91 | 0.28 |

| 64-6 | A63b-1 | A63b-3 | A63b-2 | A64-4 | A64-5 | A63b-1 | A63b-2 | A63b-3 |
|---|---|---|---|---|---|---|---|---|
| Pl | Kfs | Amp | Amp | Amp | Amp | Opx | Opx | Opx |
| matrix | matrix | core | rim | core | rim | mbayme | mbayme | mbayment |
| 57.50 | 64.69 | 45.83 | 51.41 | 42.19 | 47.07 | 52.62 | 52.58 | 53.14 |
| 0.07 | 0.00 | 0.87 | 0.00 | 1.62 | 0.68 | 0.15 | 0.08 | 0.06 |
| 25.62 | 19.02 | 10.30 | 4.54 | 11.92 | 7.94 | 1.38 | 1.37 | 0.74 |
| 0.08 | 0.63 | 19.75 | 19.14 | 22.02 | 21.84 | 28.53 | 29.24 | 28.23 |
| 0.00 | 0.00 | 0.64 | 0.62 | 0.31 | 0.40 | 1.48 | 1.36 | 1.19 |
| 0.00 | 0.00 | 9.07 | 11.38 | 6.86 | 8.50 | 12.57 | 12.77 | 13.94 |
| 9.31 | 0.01 | 10.70 | 11.31 | 10.78 | 10.80 | 1.55 | 1.33 | 1.10 |
| 6.06 | 0.18 | 1.18 | 0.32 | 1.59 | 0.92 | 0.16 | 0.13 | 0.08 |
| 0.16 | 16.07 | 0.40 | 0.10 | 1.11 | 0.38 | 0.03 | 0.03 | 0.00 |
| 0.00 | 0.00 | 0.00 | 0.00 | 0.00 | 0.00 | 0.00 | 0.00 | 0.00 |
| 98.81 | 100.60 | 98.74 | 98.82 | 98.40 | 98.53 | 98.48 | 98.89 | 98.49 |
| 10.44 | 11.90 | 6.85 | 7.69 | 6.31 | 7.04 | 2.06 | 2.05 | 2.07 |
| 0.00 | 0.00 | 0.10 | 0.00 | 0.18 | 0.08 | 0.00 | 0.00 | 0.00 |
| 5.48 | 4.12 | 1.82 | 0.80 | 2.10 | 1.40 | 0.06 | 0.06 | 0.03 |
| 0.00 | 0.00 | 1.48 | 1.99 | 0.00 | 0.96 | 0.00 | 0.00 | 0.00 |
| 0.01 | 0.10 | 0.99 | 0.40 | 2.75 | 1.77 | 0.93 | 0.95 | 0.91 |
| 0.00 | 0.00 | 0.08 | 0.08 | 0.04 | 0.05 | 0.05 | 0.04 | 0.04 |
| 0.00 | 0.00 | 2.02 | 2.54 | 1.53 | 1.89 | 0.73 | 0.74 | 0.81 |
| 1.81 | 0.00 | 1.71 | 1.81 | 1.73 | 1.73 | 0.06 | 0.06 | 0.05 |
| 2.13 | 0.06 | 0.34 | 0.09 | 0.46 | 0.27 | 0.01 | 0.01 | 0.01 |
| 0.04 | 3.77 | 0.08 | 0.02 | 0.21 | 0.07 | 0.00 | 0.00 | 0.00 |
| 0.00 | 0.00 | 0.00 | 0.00 | 0.00 | 0.00 | 0.00 | 0.00 | 0.00 |
| 19.91 | 19.96 | 15.47 | 15.42 | 15.31 | 15.26 | 3.91 | 3.92 | 3.92 |
| 32 | 32 | 23 | 23 | 23 | 23 | 6 | 6 | 6 |
| – | – | – | – | – | – | – | – | – |
| – | – | – | – | – | – | – | – | – |
| – | – | – | – | – | – | – | – | – |
| – | – | – | – | – | – | – | – | – |
| – | – | 0.67 | 0.86 | 0.36 | 0.52 | 0.44 | 0.44 | 0.47 |
| 45.48 | 0.08 | – | – | – | – | – | – | – |
| 53.57 | 1.68 | – | – | – | – | – | – | – |
| 0.94 | 98.25 | – | – | – | – | – | – | – |

Table 2. Bulk-rock major-element compositions of the studied samples. LOI: loss on ignition

| X ray fluorescence analyses | | | | | | | | | | | | |
|---|---|---|---|---|---|---|---|---|---|---|---|---|
| **Oxide wt%** | **$SiO_2$** | **$TiO_2$** | **$Al_2O_3$** | **$Fe_2O_3$(t)** | **MnO** | **MgO** | **CaO** | **$Na_2O$** | **$K_2O$** | **$P_2O_5$** | **LOI** | **Total** |
| **A37** | 52.26 | 1.37 | 25.43 | 10.22 | 0.26 | 2.55 | 0.59 | 1.47 | 5.45 | 0.05 | 0.49 | 100.13 |
| **A57** | 38.75 | 1.88 | 28.67 | 15.23 | 0.30 | 3.93 | 2.95 | 1.35 | 4.86 | 0.04 | 1.50 | 99.46 |
| **A64** | 49.00 | 1.41 | 19.91 | 12.73 | 0.18 | 4.94 | 8.05 | 0.79 | 2.16 | 0.32 | 0.85 | 100.32 |

| Modified compostions used for phase equilibria modelling | | | | | | | | | | | | |
|---|---|---|---|---|---|---|---|---|---|---|---|---|
| **Oxide mol%** | **$SiO_2$** | **$TiO_2$** | **$Al_2O_3$** | **FeO** | **$Fe_2O_3$** | **MnO** | **MgO** | **CaO** | **$Na_2O$** | **$K_2O$** | **$H_2O$** | **Total** |
| **A37** | 60.09 | 1.19 | 17.23 | 8.41 | 0.22 | 0.26 | 4.37 | 0.72 | 1.63 | 4.00 | 1.88 | 100.00 |
| **A57** | 44.70 | 1.63 | 19.49 | 12.58 | 0.33 | 0.00 | 6.77 | 3.64 | 1.51 | 3.58 | 5.77 | 100.00 |
| **A64** | 53.34 | 1.15 | 12.77 | 9.39 | 0.52 | 0.00 | 8.01 | 9.39 | 0.83 | 1.50 | 3.09 | 100.00 |

## Methods and analytical procedures

To constrain the *P–T–t* evolution at central Xolapa Complex, 68 outcrops of the metasedimentary unit were sampled in the study area. Multiple thin sections were examined using a petrographic microscope to determine diagnostic mineral assemblages and microstructures for the sequencing of mineral growth. Mineral compositions were obtained using wavelength-dispersive X-ray spectroscopy (WDS) on a JEOL JXA-8200 Super Probe at the Dipartimento di Scienze della Terra, Università degli Studi di Milano, Italy. Operating parameters were held constant for all mineral phases, with an accelerating voltage of 15 kV, a beam current of 15 nA, and a beam diameter of 2 µm. The calibration was performed using a set of natural and synthetic standards, and a ZAF matrix correction was automatically applied to all analyses. Backscattered electron (BSE) imaging was performed with a Zeiss EVO MA10 scanning electron microscope (SEM) at the Instituto de Geología, Universidad Nacional Autónoma de México (UNAM) in high vacuum mode at 15 kV. Mineral compositions were recalculated to standard numbers of oxygen per formula unit (pfu), with $H_2O$ assumed to be present in stoichiometric amounts. Bulk-rock major-element compositions were obtained via X-ray fluorescence (XRF) using a Siemens SRS 3000 spectrometer at the Instituto de Geología, UNAM.

For U–Pb geochronology, monazite was analyzed *in situ*, so individual grains were previously identified in thin section by energy-dispersive X-ray spectroscopy (EDS) and then studied using X-ray element composition maps and BSE images to distinguish homogeneous compositional domains within each one. X-ray compositional maps of Th, U and Y in monazite were acquired with a JEOL JXA-8900R Superprobe at the Laboratorio Universitario de Petrología (LUP), UNAM employing an accelerating voltage of 15 kV, a beam current of 200 nA, and a dwell time of 20 ms. Seven X-ray maps of random monazite crystals were first obtained and revealed an inverse relationship between the Y content and the shades of gray on BSE images, so these images were subsequent used to target the laser spots during the U–Pb analyses. Zircon was analyzed using crystal separates from whole-rock (A37, A63b, A64) and garnet-bearing leucosome (A57) portions. Crystals were separated by routinely used techniques of crushing, sieving, magnetic and handpicking separation, and then embedded in epoxy. Cathodoluminescence (CL) images were acquired in order to select areas to be ablated. CL imaging was performed with a Hitachi S-3100H SEM equipped with a Centaurus CL detector at the Centro de Geociencias (CGEO), UNAM.

U–Pb isotope data were acquired by laser ablation-inductively coupled plasma-mass spectrometry (LA-ICP-MS) using a Resonetics M-50 excimer laser ablation system coupled to a Thermo ICap Qc ICP-MS at the Laboratorio de Estudios Isotópicos (LEI), CGEO, UNAM. U–Pb zircon data was obtained employing a 23-µm analytical spot and an energy density (fluency) of 6 $J/cm^2$. Zircon 91500 (Wiedenbeck et al., 1995) was used as the primary bracketing standard with measurements at the beginning, end and twice each 10 unknown analyses, while Plešovice zircon (Sláma et al., 2008) was employed as a quality control reference, repeating its measurement each 10 unknown analyses. Monazite was analyzed using a 17-µm spot with 4 $J/cm^2$ fluency, and sample 44069 (Aleinikoff et al., 2006) was used as primary standard. Standard monazite was measured at the beginning, end and twice each 10 unknowns during the analytical routine. U–Pb isotope data reduction and error propagation were performed offline using Iolite (Paton et al., 2011) and employing the VizualAge data reduction scheme of Petrus and Kamber (2012). The online version of IsoplotR (Vermeesch, 2018) was used to calculate weighted mean ages, as well as to plot Wetherill concordia and kernel density estimate (KDE) diagrams. $^{204}Pb$ was not measured, because it is highly imprecise in a quadrupole-based mass spectrometer, and its signal is swamped by the $^{204}Hg$ isobaric interference. We assume that none or insignificant amount of Pb was incorporated during crystallization, so the results of both zircon and monazite have not been corrected by common lead. Accuracy and precision are granted by the analysis of Plešovice zircon secondary standard that yielded, for the current analysis, a mean $^{206}Pb/^{238}U$ age of 338.7±1.4 Ma (n=13, MSWD= 1.85).

## References


Aleinikoff JN, Schenck WS, Plank MO, et al (2006) Deciphering igneous and metamorphic events in high-grade rocks of the Wilmington Complex, Delaware: Morphology, cathodoluminescence and backscattered electron zoning, and SHRIMP U-Pb geochronology of zircon and monazite. Geological Society of America Bulletin.

Paton C, Hellstrom J, Paul B, et al (2011) Iolite: Freeware for the visualisation and processing of mass spectrometric data. Journal of Analytical Atomic Spectrometry 26:2508.

Petrus JA, Kamber BS (2012) VizualAge: A Novel Approach to Laser Ablation ICP-MS U-Pb Geochronology Data Reduction. Geostandards and Geoanalytical Research 36:247–270.

Sláma J, Košler J, Condon DJ, et al (2008) Plešovice zircon — A new natural reference material for U–Pb and Hf isotopic microanalysis. Chemical Geology 249:1–35.

Vermeesch P (2018) IsoplotR: A free and open toolbox for geochronology. Geoscience Frontiers 9:1479–1493.

Wiedenbeck M, Allé P, Corfu F, et al (1995) Three natural zircon standards for U-Th-Pb, Lu-Hf, trace element and REE analyses. Geostandards and Geoanalytical Research 19:1–23.

Table 3. U-Pb isotopic data

| | | | | | Isotope ratios | | | | | | | | |
|---|---|---|---|---|---|---|---|---|---|---|---|---|---|
| **Label** | **Ti (ppm)** | **U (ppm)** | **Th (ppm)** | **Th/U** | **$^{207}$Pb/$^{206}$Pb** | **±2s abs** | **$^{207}$Pb/$^{235}$U** | **±2s abs** | **$^{206}$Pb/$^{238}$U** | **±2s abs** | **Rho** | **$^{206}$Pb/$^{238}$U** | **±2s** |
| ***Pelitic migmatite A37–Monazite*** | | | | | | | | | | | | | |
| **WGS84 UTM coordinates: 14Q 590357 1831385** | | | | | | | | | | | | | |
| A37_Mnz-01 | – | 2970 | 34200 | 11.52 | 0.0492 | 0.0036 | 0.0568 | 0.0044 | 0.0084 | 0.0003 | 0.44 | 54.2 | 1.9 |
| A37_Mnz-02 | – | 3170 | 45800 | 14.45 | 0.0486 | 0.0037 | 0.0662 | 0.0044 | 0.0101 | 0.0003 | 0.48 | 64.6 | 2.1 |
| A37_Mnz-03 | – | 3490 | 49300 | 14.13 | 0.0490 | 0.0035 | 0.0676 | 0.0044 | 0.0100 | 0.0003 | 0.46 | 64.3 | 1.9 |
| A37_Mnz-04 | – | 3360 | 45900 | 13.66 | 0.0467 | 0.0037 | 0.0598 | 0.0046 | 0.0095 | 0.0003 | 0.44 | 60.6 | 2.1 |
| A37_Mnz-06 | – | 4640 | 38000 | 8.19 | 0.0478 | 0.0032 | 0.0547 | 0.0033 | 0.0085 | 0.0003 | 0.51 | 54.5 | 1.6 |
| A37_Mnz-07 | – | 4020 | 29600 | 7.36 | 0.0562 | 0.0033 | 0.0828 | 0.0046 | 0.0105 | 0.0003 | 0.50 | 67.5 | 1.8 |
| A37_Mnz-08 | – | 2940 | 43100 | 14.66 | 0.0484 | 0.0039 | 0.0674 | 0.0049 | 0.0101 | 0.0003 | 0.42 | 64.9 | 2.0 |
| A37_Mnz-09 | – | 3070 | 43400 | 14.14 | 0.0479 | 0.0040 | 0.0657 | 0.0050 | 0.0100 | 0.0003 | 0.41 | 64.0 | 2.0 |
| A37_Mnz-10 | – | 3490 | 44500 | 12.75 | 0.0486 | 0.0037 | 0.0658 | 0.0048 | 0.0098 | 0.0003 | 0.42 | 63.0 | 1.9 |
| A37_Mnz-11 | – | 3260 | 43500 | 13.34 | 0.0472 | 0.0040 | 0.0636 | 0.0047 | 0.0096 | 0.0003 | 0.39 | 61.6 | 1.8 |
| A37_Mnz-12 | – | 2301 | 27500 | 11.95 | 0.0530 | 0.0069 | 0.0394 | 0.0054 | 0.0052 | 0.0004 | 0.51 | 33.4 | 2.3 |
| A37_Mnz-13 | – | 1720 | 25100 | 14.59 | 0.0590 | 0.0074 | 0.0366 | 0.0047 | 0.0049 | 0.0002 | 0.37 | 31.2 | 1.4 |
| A37_Mnz-02 | – | 3171 | 67200 | 21.19 | 0.0488 | 0.0038 | 0.0596 | 0.0068 | 0.0090 | 0.0006 | 0.11 | 57.7 | 3.5 |
| A37_Mnz-04 | – | 3750 | 62700 | 16.72 | 0.0502 | 0.0041 | 0.0590 | 0.0075 | 0.0085 | 0.0006 | 0.35 | 54.7 | 3.6 |
| A37_Mnz-06 | – | 5090 | 79900 | 15.70 | 0.0512 | 0.0044 | 0.0624 | 0.0089 | 0.0092 | 0.0007 | -0.02 | 59.0 | 4.2 |
| A37_Mnz-07 | – | 4530 | 64200 | 14.17 | 0.0480 | 0.0036 | 0.0609 | 0.0067 | 0.0094 | 0.0006 | 0.05 | 60.1 | 3.7 |
| A37_Mnz-08 | – | 5760 | 65400 | 11.35 | 0.0477 | 0.0034 | 0.0596 | 0.0065 | 0.0091 | 0.0006 | 0.06 | 58.5 | 3.6 |
| A37_Mnz-10 | – | 3510 | 58800 | 16.75 | 0.0503 | 0.0041 | 0.0484 | 0.0054 | 0.0073 | 0.0005 | 0.27 | 46.7 | 3.0 |
| A37_Mnz-12 | – | 5220 | 67400 | 12.91 | 0.0498 | 0.0039 | 0.0630 | 0.0073 | 0.0093 | 0.0006 | -0.08 | 59.5 | 3.7 |
| A37_Mnz-14 | – | 5240 | 62400 | 11.91 | 0.0543 | 0.0043 | 0.0710 | 0.0085 | 0.0095 | 0.0006 | -0.20 | 61.1 | 3.8 |
| A37_Mnz-15 | – | 2863 | 64400 | 22.49 | 0.0482 | 0.0037 | 0.0609 | 0.0070 | 0.0091 | 0.0006 | 0.34 | 58.2 | 3.7 |
| ***Corundum-bearing pelitic migmatite A57–Monazite*** | | | | | | | | | | | | | |
| **WGS84 UTM coordinates: 14Q 599519 1833143** | | | | | | | | | | | | | |
| A57_Mnz-01 | – | 1701 | 52400 | 30.81 | 0.0645 | 0.0053 | 0.0456 | 0.0048 | 0.0053 | 0.0003 | 0.54 | 33.9 | 1.9 |
| A57_Mnz-02 | – | 1815 | 46800 | 25.79 | 0.0511 | 0.0054 | 0.0421 | 0.0052 | 0.0060 | 0.0003 | 0.46 | 38.4 | 2.2 |
| A57_Mnz-03 | – | 1389 | 39400 | 28.37 | 0.0516 | 0.0044 | 0.0521 | 0.0043 | 0.0075 | 0.0003 | 0.45 | 48.0 | 1.8 |
| A57_Mnz-04 | – | 2770 | 42900 | 15.49 | 0.0511 | 0.0040 | 0.0600 | 0.0041 | 0.0088 | 0.0003 | 0.45 | 56.7 | 1.7 |
| A57_Mnz-06 | – | 408 | 33400 | 81.86 | 0.0600 | 0.0160 | 0.0317 | 0.0081 | 0.0039 | 0.0003 | 0.32 | 24.8 | 2.0 |
| A57_Mnz-11 | – | 3950 | 35500 | 8.99 | 0.0463 | 0.0032 | 0.0504 | 0.0030 | 0.0077 | 0.0003 | 0.59 | 49.3 | 1.7 |
| A57_Mnz-12 | – | 1140 | 42800 | 37.54 | 0.0525 | 0.0170 | 0.0416 | 0.0160 | 0.0057 | 0.0004 | 0.18 | 36.9 | 2.5 |
| A57_Mnz-13 | – | 1200 | 34900 | 29.08 | 0.0490 | 0.0073 | 0.0359 | 0.0043 | 0.0052 | 0.0002 | 0.38 | 33.7 | 1.6 |
| A57_Mnz-15 | – | 770 | 38500 | 50.00 | 0.0540 | 0.0110 | 0.0315 | 0.0062 | 0.0042 | 0.0002 | 0.26 | 27.1 | 1.4 |
| A57_Mnz-16 | – | 3880 | 39000 | 10.05 | 0.0511 | 0.0050 | 0.0536 | 0.0047 | 0.0077 | 0.0003 | 0.43 | 49.4 | 1.9 |
| A57_Mnz-17 | – | 777 | 52160 | 67.13 | 0.0600 | 0.0140 | 0.0360 | 0.0073 | 0.0045 | 0.0002 | 0.23 | 29.2 | 1.4 |
| A57_Mnz-18 | – | 5790 | 39500 | 6.82 | 0.0471 | 0.0036 | 0.0533 | 0.0033 | 0.0082 | 0.0003 | 0.55 | 52.4 | 1.8 |
| A57_Mnz-19 | – | 5110 | 35300 | 6.91 | 0.0453 | 0.0027 | 0.0523 | 0.0029 | 0.0083 | 0.0002 | 0.52 | 53.1 | 1.5 |
| A57_Mnz-20 | – | 5580 | 34300 | 6.15 | 0.0476 | 0.0027 | 0.0553 | 0.0029 | 0.0083 | 0.0003 | 0.57 | 53.3 | 1.6 |
| A57_Mnz-21 | – | 2760 | 29900 | 10.83 | 0.0472 | 0.0033 | 0.0589 | 0.0038 | 0.0091 | 0.0003 | 0.47 | 58.7 | 1.8 |
| A57_Mnz-22 | – | 1120 | 26800 | 23.93 | 0.0543 | 0.0047 | 0.0424 | 0.0042 | 0.0062 | 0.0003 | 0.54 | 39.8 | 2.1 |
| A57_Mnz-23 | – | 2984 | 37000 | 12.40 | 0.0508 | 0.0030 | 0.1153 | 0.0061 | 0.0166 | 0.0005 | 0.56 | 105.9 | 3.1 |
| A57_Mnz-24 | – | 1472 | 66100 | 44.90 | 0.0521 | 0.0044 | 0.0590 | 0.0061 | 0.0081 | 0.0004 | 0.52 | 52.3 | 2.8 |
| A57_Mnz-26 | – | 2738 | 37380 | 13.65 | 0.0508 | 0.0034 | 0.1167 | 0.0092 | 0.0167 | 0.0010 | 0.76 | 106.7 | 6.6 |
| A57_Mnz-27 | – | 1049 | 38900 | 37.08 | 0.0495 | 0.0095 | 0.0326 | 0.0063 | 0.0049 | 0.0002 | 0.24 | 31.3 | 1.5 |
| A57_Mnz-28 | – | 1900 | 34100 | 17.95 | 0.0471 | 0.0035 | 0.0847 | 0.0059 | 0.0129 | 0.0004 | 0.47 | 82.8 | 2.6 |
| A57_Mnz-29 | – | 2404 | 49800 | 20.72 | 0.0467 | 0.0041 | 0.0343 | 0.0042 | 0.0054 | 0.0004 | 0.62 | 34.9 | 2.6 |
| A57_Mnz-30 | – | 839 | 4340 | 5.17 | 0.0488 | 0.0042 | 0.1050 | 0.0091 | 0.0159 | 0.0010 | 0.72 | 101.3 | 6.3 |
| A57_Mnz-32 | – | 441 | 45200 | 102.49 | 0.0590 | 0.0140 | 0.0301 | 0.0077 | 0.0040 | 0.0003 | 0.33 | 25.9 | 2.2 |
| A57_Mnz-33 | – | 5930 | 11900 | 2.01 | 0.0478 | 0.0027 | 0.0554 | 0.0033 | 0.0084 | 0.0002 | 0.48 | 54.1 | 1.6 |
| A57_Mnz-34 | – | 1513 | 13700 | 9.05 | 0.0476 | 0.0046 | 0.0666 | 0.0087 | 0.0099 | 0.0009 | 0.69 | 63.8 | 5.7 |
| A57_Mnz-35 | – | 2326 | 24200 | 10.40 | 0.0479 | 0.0040 | 0.0668 | 0.0074 | 0.0098 | 0.0009 | 0.79 | 62.8 | 5.5 |
| A57_Mnz-37 | – | 1600 | 11450 | 7.16 | 0.0485 | 0.0048 | 0.0563 | 0.0054 | 0.0087 | 0.0003 | 0.37 | 55.5 | 2.0 |
| A57_Mnz-42 | – | 1615 | 36000 | 22.29 | 0.0540 | 0.0076 | 0.0315 | 0.0044 | 0.0042 | 0.0002 | 0.33 | 26.7 | 1.2 |
| A57_Mnz-43 | – | 1622 | 36300 | 22.38 | 0.0484 | 0.0061 | 0.0281 | 0.0036 | 0.0044 | 0.0002 | 0.34 | 28.1 | 1.2 |
| A57_Mnz-44 | – | 1732 | 40800 | 23.56 | 0.0495 | 0.0084 | 0.0308 | 0.0046 | 0.0043 | 0.0002 | 0.33 | 27.8 | 1.3 |
| A57_Mnz-46 | – | 4020 | 21500 | 5.35 | 0.0462 | 0.0028 | 0.0545 | 0.0032 | 0.0086 | 0.0003 | 0.59 | 55.4 | 1.9 |
| A57_Mnz-47 | – | 2220 | 32950 | 14.84 | 0.0481 | 0.0042 | 0.0381 | 0.0045 | 0.0060 | 0.0004 | 0.54 | 38.6 | 2.4 |
| A57_Mnz-48 | – | 1670 | 22700 | 13.59 | 0.0489 | 0.0073 | 0.0259 | 0.0036 | 0.0039 | 0.0002 | 0.31 | 25.2 | 1.1 |
| A57_Mnz-49 | – | 4130 | 28900 | 7.00 | 0.0474 | 0.0032 | 0.0624 | 0.0043 | 0.0094 | 0.0003 | 0.46 | 60.6 | 1.9 |
| A57_Mnz-50 | – | 3890 | 38900 | 10.00 | 0.0492 | 0.0037 | 0.0558 | 0.0049 | 0.0084 | 0.0003 | 0.45 | 54.2 | 2.1 |
| A57_Mnz-51 | – | 2220 | 32800 | 14.77 | 0.0494 | 0.0072 | 0.0387 | 0.0081 | 0.0056 | 0.0005 | 0.42 | 35.9 | 3.1 |
| A57_Mnz-52 | – | 952 | 2400 | 2.52 | 0.0469 | 0.0051 | 0.1310 | 0.0130 | 0.0196 | 0.0007 | 0.35 | 125.3 | 4.4 |
| A57_Mnz-53 | – | 4500 | 9350 | 2.08 | 0.0481 | 0.0036 | 0.0689 | 0.0080 | 0.0106 | 0.0011 | 0.90 | 67.7 | 6.8 |
| A57_Mnz-54 | – | 1141 | 2894 | 2.54 | 0.0499 | 0.0042 | 0.1280 | 0.0100 | 0.0189 | 0.0007 | 0.50 | 120.5 | 4.7 |
| A57_Mnz-55 | – | 6530 | 8580 | 1.31 | 0.0480 | 0.0031 | 0.0672 | 0.0041 | 0.0100 | 0.0004 | 0.59 | 64.4 | 2.3 |
| A57_Mnz-56 | – | 4020 | 14900 | 3.71 | 0.0502 | 0.0028 | 0.1201 | 0.0065 | 0.0176 | 0.0005 | 0.57 | 112.4 | 3.5 |
| A57_Mnz-58 | – | 1939 | 44400 | 22.90 | 0.0599 | 0.0050 | 0.0467 | 0.0040 | 0.0057 | 0.0002 | 0.45 | 36.3 | 1.4 |
| A57_Mnz-59 | – | 1816 | 45700 | 25.17 | 0.0519 | 0.0066 | 0.0370 | 0.0052 | 0.0053 | 0.0003 | 0.38 | 34.1 | 1.8 |
| A57_Mnz-65 | – | 1950 | 35200 | 18.05 | 0.0478 | 0.0055 | 0.0343 | 0.0039 | 0.0050 | 0.0002 | 0.35 | 32.0 | 1.3 |
| A57_Mnz-66 | – | 2120 | 40700 | 19.20 | 0.0504 | 0.0066 | 0.0350 | 0.0048 | 0.0050 | 0.0002 | 0.31 | 32.2 | 1.3 |
| A57_Mnz-71 | – | 2199 | 33100 | 15.05 | 0.0466 | 0.0036 | 0.0468 | 0.0051 | 0.0073 | 0.0005 | 0.63 | 46.6 | 3.2 |
| A57_Mnz-72 | – | 4080 | 31500 | 7.72 | 0.0483 | 0.0035 | 0.0612 | 0.0043 | 0.0093 | 0.0003 | 0.43 | 59.7 | 1.8 |

***Pelitic migmatite A37 (whole-rock)–Zircon***

**WGS84 UTM coordinates: 14Q 590357 1831385**

| | | | | | | | | | | | | | |
|---|---|---|---|---|---|---|---|---|---|---|---|---|---|
| A37_Zm-01 | 5.0 | 948 | 12 | 0.01 | 0.0460 | 0.0032 | 0.0572 | 0.0038 | 0.0090 | 0.0002 | 0.02 | 57.8 | 1.2 |
| A37_Zm-03 | 7.4 | 792 | 10 | 0.01 | 0.0497 | 0.0034 | 0.0623 | 0.0042 | 0.0093 | 0.0002 | 0.15 | 59.8 | 1.4 |
| A37_Zm-04 | 3.4 | 300 | 113 | 0.38 | 0.0486 | 0.0089 | 0.0272 | 0.0043 | 0.0042 | 0.0002 | -0.08 | 27.0 | 1.1 |
| A37_Zm-05 | 3.6 | 356 | 102 | 0.29 | 0.0570 | 0.0082 | 0.0302 | 0.0045 | 0.0040 | 0.0002 | -0.29 | 25.8 | 1.0 |
| A37_Zm-06 | 1.8 | 204 | 35 | 0.17 | 0.0464 | 0.0100 | 0.0271 | 0.0054 | 0.0040 | 0.0002 | 0.11 | 25.6 | 1.2 |
| A37_Zm-07 | 4.3 | 312 | 61 | 0.20 | 0.0533 | 0.0082 | 0.0296 | 0.0049 | 0.0040 | 0.0002 | 0.34 | 25.9 | 1.1 |
| A37_Zm-08 | 1.5 | 284 | 111 | 0.39 | 0.0520 | 0.0110 | 0.0283 | 0.0058 | 0.0041 | 0.0001 | 0.15 | 26.1 | 0.9 |
| A37_Zm-12 | 1.9 | 820 | 9 | 0.01 | 0.0491 | 0.0047 | 0.0618 | 0.0058 | 0.0093 | 0.0006 | 0.06 | 59.6 | 3.7 |
| A37_Zm-14 | 3.6 | 219 | 78 | 0.36 | 0.0480 | 0.0110 | 0.0297 | 0.0067 | 0.0042 | 0.0002 | 0.19 | 26.8 | 1.0 |
| A37_Zm-17 | 7.5 | 982 | 8 | 0.01 | 0.0460 | 0.0031 | 0.0601 | 0.0039 | 0.0097 | 0.0002 | -0.20 | 62.2 | 1.2 |
| A37_Zm-18 | 4.3 | 1017 | 10 | 0.01 | 0.0482 | 0.0033 | 0.0630 | 0.0045 | 0.0096 | 0.0002 | 0.33 | 61.7 | 1.3 |
| A37_Zm-20 | 4.3 | 269 | 70 | 0.26 | 0.0590 | 0.0110 | 0.0322 | 0.0055 | 0.0041 | 0.0002 | -0.20 | 26.2 | 1.0 |
| A37_Zm-21 | 3.0 | 300 | 92 | 0.31 | 0.0460 | 0.0080 | 0.0268 | 0.0059 | 0.0042 | 0.0004 | 0.19 | 27.3 | 2.2 |
| A37_Zm-22 | 7.9 | 349 | 123 | 0.35 | 0.0540 | 0.0100 | 0.0314 | 0.0056 | 0.0041 | 0.0002 | 0.09 | 26.4 | 1.0 |
| A37_Zm-23 | 3.7 | 284 | 105 | 0.37 | 0.0461 | 0.0080 | 0.0285 | 0.0049 | 0.0042 | 0.0002 | 0.26 | 27.3 | 1.0 |
| A37_Zm-24 | 4.3 | 278 | 78 | 0.28 | 0.0560 | 0.0100 | 0.0307 | 0.0058 | 0.0041 | 0.0001 | -0.10 | 26.6 | 0.9 |
| A37_Zm-26 | 3.0 | 269 | 92 | 0.34 | 0.0493 | 0.0085 | 0.0286 | 0.0043 | 0.0041 | 0.0002 | -0.25 | 26.3 | 1.1 |
| A37_Zm-28 | 2.9 | 338 | 108 | 0.32 | 0.0530 | 0.0110 | 0.0297 | 0.0062 | 0.0041 | 0.0004 | -0.28 | 26.5 | 2.4 |
| A37_Zm-30 | 5.9 | 325 | 111 | 0.34 | 0.0514 | 0.0087 | 0.0295 | 0.0050 | 0.0042 | 0.0002 | 0.09 | 26.9 | 1.0 |
| A37_Zm-32 | 2.2 | 332 | 70 | 0.21 | 0.0512 | 0.0084 | 0.0269 | 0.0040 | 0.0040 | 0.0001 | -0.18 | 25.9 | 0.9 |
| A37_Zm-33 | 4.4 | 260 | 79 | 0.30 | 0.0580 | 0.0120 | 0.0319 | 0.0065 | 0.0041 | 0.0002 | -0.07 | 26.5 | 1.1 |
| A37_Zm-34 | 5.7 | 318 | 114 | 0.36 | 0.0519 | 0.0081 | 0.0277 | 0.0040 | 0.0041 | 0.0002 | 0.17 | 26.2 | 1.1 |
| A37_Zm-38 | 3.1 | 211 | 51 | 0.24 | 0.0530 | 0.0088 | 0.0329 | 0.0079 | 0.0045 | 0.0005 | 0.11 | 28.8 | 2.9 |
| A37_Zm-42 | 4.9 | 338 | 118 | 0.35 | 0.0540 | 0.0098 | 0.0303 | 0.0053 | 0.0041 | 0.0002 | 0.13 | 26.5 | 1.1 |
| A37_Zm-43 | 3.4 | 327 | 106 | 0.32 | 0.0570 | 0.0093 | 0.0314 | 0.0055 | 0.0042 | 0.0002 | -0.18 | 27.2 | 1.4 |
| A37_Zm-50 | 4.5 | 503 | 184 | 0.37 | 0.0487 | 0.0054 | 0.0265 | 0.0032 | 0.0039 | 0.0001 | 0.07 | 25.3 | 0.7 |
| A37_Zm-51 | 6.5 | 468 | 143 | 0.31 | 0.0550 | 0.0064 | 0.0325 | 0.0076 | 0.0045 | 0.0005 | -0.04 | 29.2 | 3.0 |
| A37_Zm-54 | 4.3 | 344 | 88 | 0.26 | 0.0550 | 0.0079 | 0.0314 | 0.0059 | 0.0040 | 0.0002 | 0.14 | 26.0 | 1.5 |
| A37_Zm-55 | 5.9 | 317 | 59 | 0.19 | 0.0520 | 0.0082 | 0.0313 | 0.0041 | 0.0041 | 0.0001 | 0.09 | 26.6 | 0.9 |
| A63_Zm-52 | 8.4 | 577 | 5 | 0.01 | 0.0493 | 0.0051 | 0.0677 | 0.0056 | 0.0098 | 0.0006 | 0.22 | 62.6 | 3.5 |
| A63_Zm-58 | 12.0 | 699 | 6 | 0.01 | 0.0485 | 0.0056 | 0.0616 | 0.0073 | 0.0091 | 0.0003 | 0.13 | 58.4 | 2.2 |
| A63_Zm-65 | 1.4 | 588 | 4 | 0.01 | 0.0515 | 0.0062 | 0.0710 | 0.0088 | 0.0099 | 0.0004 | 0.19 | 63.7 | 2.6 |
| A63_Zm-43 | 8.9 | 852 | 8 | 0.01 | 0.0514 | 0.0044 | 0.0697 | 0.0081 | 0.0100 | 0.0003 | 0.40 | 64.0 | 1.8 |
| A63_Zm-47 | 2.0 | 996 | 115 | 0.12 | 0.0487 | 0.0038 | 0.0631 | 0.0058 | 0.0096 | 0.0002 | -0.04 | 61.6 | 1.4 |
| A63_Zm-54 | 2.5 | 213 | 30 | 0.14 | 0.0512 | 0.0098 | 0.0670 | 0.0140 | 0.0100 | 0.0004 | 0.07 | 64.0 | 2.7 |
| A63_Zm-70 | 11.1 | 1387 | 23 | 0.02 | 0.0516 | 0.0034 | 0.0801 | 0.0077 | 0.0113 | 0.0004 | 0.06 | 72.5 | 2.3 |
| A63_Zm-74 | 8.3 | 260 | 50 | 0.19 | 0.0591 | 0.0070 | 0.0682 | 0.0091 | 0.0094 | 0.0003 | -0.18 | 60.2 | 2.1 |

***Corundum-bearing pelitic migmatite A57 (garnet leucosome)–Zircon***

**WGS84 UTM coordinates: 14Q 599519 1833143**

| | | | | | | | | | | | | | |
|---|---|---|---|---|---|---|---|---|---|---|---|---|---|
| A57_Zm-66 | 2.1 | 1240 | 12 | 0.01 | 0.0489 | 0.0041 | 0.0710 | 0.0060 | 0.0103 | 0.0004 | 0.35 | 65.7 | 2.4 |
| A57_Zm-67 | 5.3 | 657 | 26 | 0.04 | 0.0540 | 0.0047 | 0.0496 | 0.0044 | 0.0068 | 0.0002 | -0.09 | 43.9 | 1.1 |
| A57_Zm-70 | 4.6 | 117 | 47 | 0.40 | 0.0734 | 0.0033 | 1.7590 | 0.0980 | 0.1721 | 0.0032 | 0.17 | 1023.0 | 18.0 |
| A57_Zm-74 | 4.9 | 764 | 27 | 0.04 | 0.0506 | 0.0049 | 0.0484 | 0.0048 | 0.0071 | 0.0002 | 0.21 | 45.4 | 1.3 |
| A57_Zm-77 | 5.7 | 383 | 42 | 0.11 | 0.0525 | 0.0058 | 0.0750 | 0.0087 | 0.0103 | 0.0003 | 0.19 | 65.8 | 2.1 |
| A57_Zm-78 | 4.1 | 313 | 95 | 0.30 | 0.0531 | 0.0068 | 0.0655 | 0.0090 | 0.0091 | 0.0003 | 0.33 | 58.4 | 2.2 |
| A57_Zm-79 | 0.7 | 861 | 22 | 0.03 | 0.0501 | 0.0043 | 0.0554 | 0.0051 | 0.0079 | 0.0002 | -0.01 | 50.6 | 1.1 |
| A57_Zm-80 | 3.9 | 185 | 47 | 0.25 | 0.0465 | 0.0067 | 0.0599 | 0.0085 | 0.0093 | 0.0004 | 0.09 | 59.5 | 2.7 |
| A57_Zm-81 | 3.0 | 181 | 42 | 0.23 | 0.0548 | 0.0083 | 0.0675 | 0.0099 | 0.0098 | 0.0005 | 0.17 | 62.6 | 3.2 |
| A57_Zm-82 | 3.1 | 174 | 34 | 0.20 | 0.0509 | 0.0081 | 0.0670 | 0.0110 | 0.0095 | 0.0004 | -0.12 | 60.7 | 2.5 |
| A57_Zm-83 | 2.4 | 204 | 40 | 0.20 | 0.0488 | 0.0091 | 0.0640 | 0.0150 | 0.0095 | 0.0007 | 0.39 | 61.1 | 4.6 |
| A57_Zm-84 | 2.5 | 235 | 43 | 0.18 | 0.0544 | 0.0076 | 0.0679 | 0.0097 | 0.0091 | 0.0004 | 0.10 | 58.5 | 2.8 |
| A57_Zm-85 | 3.9 | 1283 | 40 | 0.03 | 0.0498 | 0.0024 | 0.0838 | 0.0052 | 0.0124 | 0.0003 | 0.54 | 79.5 | 1.6 |
| A57_Zm-86 | 3.6 | 231 | 61 | 0.26 | 0.0445 | 0.0068 | 0.0567 | 0.0080 | 0.0092 | 0.0005 | -0.23 | 59.2 | 2.9 |
| A57_Zm-87 | 5.3 | 326 | 85 | 0.26 | 0.0541 | 0.0054 | 0.1740 | 0.0190 | 0.0243 | 0.0012 | 0.50 | 154.9 | 7.5 |
| A57_Zm-88 | 3.3 | 286 | 33 | 0.11 | 0.0489 | 0.0070 | 0.0564 | 0.0081 | 0.0083 | 0.0004 | 0.56 | 53.2 | 2.5 |
| A57_Zm-89 | 3.6 | 216 | 52 | 0.24 | 0.0426 | 0.0056 | 0.0586 | 0.0077 | 0.0099 | 0.0003 | -0.10 | 63.6 | 2.1 |
| A57_Zm-90 | 4.2 | 733 | 23 | 0.03 | 0.0509 | 0.0041 | 0.0496 | 0.0043 | 0.0070 | 0.0002 | 0.06 | 44.9 | 1.3 |
| A57_Zm-91 | 5.3 | 203 | 50 | 0.25 | 0.0469 | 0.0068 | 0.0615 | 0.0092 | 0.0093 | 0.0004 | 0.12 | 59.6 | 2.6 |
| A57_Zm-92 | 3.0 | 278 | 53 | 0.19 | 0.1768 | 0.0046 | 11.7000 | 0.5300 | 0.4900 | 0.0140 | 0.67 | 2568.0 | 59.0 |
| A57_Zm-93 | 14.9 | 259 | 174 | 0.67 | 0.1872 | 0.0046 | 13.0700 | 0.5300 | 0.5052 | 0.0060 | 0.47 | 2636.0 | 26.0 |
| A57_Zm-95 | 2.6 | 545 | 31 | 0.06 | 0.0638 | 0.0021 | 0.8420 | 0.0430 | 0.0975 | 0.0019 | 0.61 | 599.8 | 11.0 |
| A57_Zm-96 | 3.7 | 235 | 53 | 0.22 | 0.0483 | 0.0064 | 0.0627 | 0.0081 | 0.0097 | 0.0003 | -0.18 | 62.2 | 2.0 |
| A57_Zm-97 | 2.2 | 418 | 16 | 0.04 | 0.0512 | 0.0052 | 0.0693 | 0.0071 | 0.0098 | 0.0003 | -0.05 | 62.7 | 1.9 |
| A57_Zm-98 | 1.8 | 801 | 5 | 0.01 | 0.0480 | 0.0029 | 0.0692 | 0.0046 | 0.0105 | 0.0002 | 0.19 | 67.6 | 1.5 |
| A57_Zm-99 | 4.9 | 520 | 72 | 0.14 | 0.0470 | 0.0044 | 0.0608 | 0.0057 | 0.0093 | 0.0003 | 0.17 | 59.5 | 2.0 |
| A57_Zm-100 | 3.7 | 954 | 21 | 0.02 | 0.0482 | 0.0038 | 0.0379 | 0.0031 | 0.0056 | 0.0002 | -0.20 | 36.0 | 1.0 |
| A57_Zm-101 | 6.8 | 1110 | 13 | 0.01 | 0.0452 | 0.0050 | 0.0632 | 0.0080 | 0.0102 | 0.0006 | 0.41 | 65.2 | 3.6 |
| A57_Zm-102 | 4.0 | 235 | 40 | 0.17 | 0.0518 | 0.0065 | 0.0686 | 0.0085 | 0.0096 | 0.0004 | 0.03 | 61.4 | 2.5 |
| A57_Zm-103 | 6.6 | 209 | 37 | 0.18 | 0.0458 | 0.0065 | 0.0640 | 0.0110 | 0.0105 | 0.0006 | -0.03 | 67.3 | 3.8 |
| A57_Zm-104 | 3.0 | 165 | 48 | 0.29 | 0.0503 | 0.0092 | 0.0660 | 0.0110 | 0.0095 | 0.0004 | -0.24 | 60.7 | 2.7 |

***Garnet-bearing mafic schist A63b–Zircon***

**WGS84 UTM coordinates: 14Q 602946 1839331**

| | | | | | | | | | | | | | |
|---|---|---|---|---|---|---|---|---|---|---|---|---|---|
| A63b_Zm-01 | 6.7 | 425 | 377 | 0.89 | 0.0494 | 0.0074 | 0.0368 | 0.0053 | 0.0054 | 0.0002 | -0.09 | 34.5 | 1.4 |
| A63b_Zm-02 | 4.6 | 354 | 33 | 0.09 | 0.0534 | 0.0092 | 0.0356 | 0.0058 | 0.0051 | 0.0002 | 0.01 | 32.5 | 1.4 |
| A63b_Zm-03 | 7.9 | 728 | 817 | 1.12 | 0.0594 | 0.0077 | 0.0437 | 0.0055 | 0.0053 | 0.0002 | -0.12 | 34.2 | 1.1 |

| | | | | | | | | | | | | | |
|---|---|---|---|---|---|---|---|---|---|---|---|---|---|
| A63b_Zm-04 | 12.9 | 685 | 873 | 1.27 | 0.0502 | 0.0082 | 0.0349 | 0.0057 | 0.0050 | 0.0002 | -0.25 | 32.0 | 1.3 |
| A63b_Zm-05 | 9.2 | 635 | 772 | 1.22 | 0.0560 | 0.0077 | 0.0402 | 0.0056 | 0.0052 | 0.0002 | -0.27 | 33.6 | 1.1 |
| A63b_Zm-06 | 6.6 | 386 | 373 | 0.97 | 0.0542 | 0.0097 | 0.0386 | 0.0068 | 0.0054 | 0.0002 | 0.06 | 34.4 | 1.4 |
| A63b_Zm-07 | 7.8 | 282 | 250 | 0.89 | 0.0590 | 0.0120 | 0.0439 | 0.0094 | 0.0057 | 0.0003 | -0.04 | 36.4 | 1.6 |
| A63b_Zm-08 | 8.4 | 342 | 299 | 0.87 | 0.0500 | 0.0110 | 0.0335 | 0.0076 | 0.0050 | 0.0002 | 0.30 | 32.0 | 1.5 |
| A63b_Zm-09 | 9.2 | 420 | 473 | 1.13 | 0.0540 | 0.0079 | 0.0423 | 0.0064 | 0.0056 | 0.0002 | 0.11 | 35.9 | 1.2 |
| A63b_Zm-10 | 13.9 | 210 | 144 | 0.68 | 0.0490 | 0.0230 | 0.0360 | 0.0200 | 0.0052 | 0.0003 | 0.08 | 33.4 | 2.1 |
| A63b_Zm-11 | 6.3 | 92 | 28 | 0.31 | 0.0660 | 0.0290 | 0.0460 | 0.0210 | 0.0056 | 0.0004 | 0.17 | 35.7 | 2.7 |
| A63b_Zm-13 | 10.5 | 136 | 47 | 0.35 | 0.0495 | 0.0100 | 0.0780 | 0.0150 | 0.0115 | 0.0006 | -0.14 | 73.7 | 3.7 |
| A63b_Zm-14 | 6.0 | 618 | 203 | 0.33 | 0.0476 | 0.0039 | 0.0628 | 0.0048 | 0.0096 | 0.0003 | 0.02 | 61.7 | 1.7 |
| A63b_Zm-15 | 6.8 | 238 | 160 | 0.67 | 0.0460 | 0.0100 | 0.0334 | 0.0074 | 0.0053 | 0.0002 | 0.24 | 34.1 | 1.5 |
| A63b_Zm-16 | 2.5 | 499 | 26 | 0.05 | 0.0590 | 0.0082 | 0.0396 | 0.0052 | 0.0048 | 0.0002 | -0.04 | 30.7 | 1.1 |
| A63b_Zm-17 | 7.4 | 524 | 567 | 1.08 | 0.0660 | 0.0084 | 0.0463 | 0.0061 | 0.0051 | 0.0001 | 0.11 | 32.7 | 0.9 |
| A63b_Zm-21 | 12.6 | 704 | 866 | 1.23 | 0.0461 | 0.0054 | 0.0333 | 0.0038 | 0.0052 | 0.0001 | 0.11 | 33.5 | 0.9 |
| A63b_Zm-22 | 5.1 | 156 | 110 | 0.70 | 0.0470 | 0.0140 | 0.0350 | 0.0096 | 0.0055 | 0.0003 | 0.02 | 35.5 | 1.9 |
| A63b_Zm-23 | 10.2 | 679 | 761 | 1.12 | 0.0554 | 0.0069 | 0.0419 | 0.0047 | 0.0054 | 0.0002 | 0.05 | 34.7 | 1.1 |
| A63b_Zm-24 | 5.5 | 86 | 48 | 0.56 | 0.0700 | 0.0200 | 0.0480 | 0.0150 | 0.0058 | 0.0004 | 0.02 | 37.0 | 2.3 |
| A63b_Zm-25 | 4.6 | 125 | 34 | 0.27 | 0.0570 | 0.0210 | 0.0400 | 0.0130 | 0.0053 | 0.0005 | 0.08 | 33.9 | 2.9 |
| A63b_Zm-26 | 5.6 | 241 | 256 | 1.06 | 0.0472 | 0.0089 | 0.0354 | 0.0068 | 0.0057 | 0.0002 | 0.05 | 36.4 | 1.6 |
| A63b_Zm-27 | 3.6 | 504 | 40 | 0.08 | 0.0525 | 0.0073 | 0.0360 | 0.0048 | 0.0050 | 0.0002 | 0.15 | 31.9 | 1.1 |
| A63b_Zm-29 | 8.3 | 312 | 326 | 1.04 | 0.0563 | 0.0088 | 0.0431 | 0.0066 | 0.0054 | 0.0002 | 0.13 | 34.7 | 1.3 |
| A63b_Zm-30 | 4.2 | 209 | 57 | 0.27 | 0.0440 | 0.0110 | 0.0380 | 0.0089 | 0.0056 | 0.0003 | 0.09 | 36.1 | 2.2 |
| A63b_Zm-35 | 4.6 | 397 | 209 | 0.53 | 0.0508 | 0.0049 | 0.1025 | 0.0097 | 0.0146 | 0.0006 | -0.21 | 93.5 | 3.7 |
| A63b_Zm-38 | 8.8 | 272 | 222 | 0.82 | 0.0540 | 0.0110 | 0.0404 | 0.0071 | 0.0053 | 0.0002 | -0.14 | 34.1 | 1.4 |
| A63b_Zm-39 | 8.4 | 640 | 809 | 1.26 | 0.0497 | 0.0073 | 0.0345 | 0.0049 | 0.0051 | 0.0002 | -0.19 | 33.1 | 1.2 |
| A63b_Zm-40 | 8.1 | 556 | 578 | 1.04 | 0.0531 | 0.0086 | 0.0375 | 0.0060 | 0.0054 | 0.0002 | 0.14 | 34.4 | 1.1 |
| ***Garnet-bearing mafic schist A64–Zircon*** | | | | | | | | | | | | | |
| **WGS84 UTM coordinates: 14Q 599934 1837297** | | | | | | | | | | | | | |
| A64_Zm-01 | 4.2 | 125 | 20 | 0.16 | 0.0590 | 0.0180 | 0.0450 | 0.0130 | 0.0058 | 0.0004 | -0.06 | 37.0 | 2.5 |
| A64_Zm-02 | 4.1 | 249 | 45 | 0.18 | 0.0540 | 0.0065 | 0.1050 | 0.0130 | 0.0151 | 0.0007 | 0.18 | 96.3 | 4.5 |
| A64_Zm-03 | 8.8 | 366 | 277 | 0.76 | 0.0500 | 0.0088 | 0.0370 | 0.0065 | 0.0050 | 0.0002 | 0.08 | 32.4 | 1.4 |
| A64_Zm-04 | 10.2 | 242 | 134 | 0.56 | 0.0510 | 0.0120 | 0.0354 | 0.0084 | 0.0051 | 0.0003 | -0.13 | 32.9 | 1.7 |
| A64_Zm-05 | 4.7 | 1630 | 286 | 0.18 | 0.0480 | 0.0043 | 0.0464 | 0.0041 | 0.0071 | 0.0002 | -0.01 | 45.7 | 1.1 |
| A64_Zm-06 | 5.7 | 97 | 44 | 0.46 | 0.0500 | 0.0190 | 0.0460 | 0.0140 | 0.0059 | 0.0005 | 0.17 | 37.6 | 2.9 |
| A64_Zm-07 | 5.1 | 401 | 100 | 0.25 | 0.0610 | 0.0090 | 0.0379 | 0.0062 | 0.0048 | 0.0002 | 0.04 | 31.0 | 1.4 |
| A64_Zm-08 | 7.3 | 205 | 99 | 0.48 | 0.0510 | 0.0120 | 0.0377 | 0.0083 | 0.0052 | 0.0002 | -0.23 | 33.1 | 1.4 |
| A64_Zm-09 | 14.3 | 594 | 41 | 0.07 | 0.0532 | 0.0042 | 0.1480 | 0.0120 | 0.0207 | 0.0005 | 0.27 | 132.0 | 3.4 |
| A64_Zm-10 | 4.9 | 1220 | 59 | 0.05 | 0.0484 | 0.0043 | 0.0480 | 0.0039 | 0.0071 | 0.0002 | -0.18 | 45.6 | 1.0 |
| A64_Zm-12 | 4.9 | 1980 | 1107 | 0.56 | 0.0489 | 0.0031 | 0.1258 | 0.0074 | 0.0185 | 0.0004 | -0.03 | 118.3 | 2.2 |
| A64_Zm-15 | 15.6 | 296 | 143 | 0.48 | 0.0440 | 0.0100 | 0.0322 | 0.0076 | 0.0051 | 0.0002 | 0.04 | 33.0 | 1.6 |
| A64_Zm-16 | 9.3 | 608 | 636 | 1.05 | 0.0502 | 0.0056 | 0.0499 | 0.0050 | 0.0070 | 0.0002 | -0.16 | 45.2 | 1.3 |
| A64_Zm-18 | 8.4 | 101 | 47 | 0.47 | 0.0520 | 0.0200 | 0.0370 | 0.0150 | 0.0055 | 0.0003 | 0.14 | 35.2 | 2.2 |
| A64_Zm-19 | 7.9 | 146 | 68 | 0.47 | 0.0540 | 0.0087 | 0.1110 | 0.0190 | 0.0148 | 0.0008 | 0.23 | 94.9 | 5.1 |
| A64_Zm-20 | 4.8 | 1035 | 128 | 0.12 | 0.0483 | 0.0049 | 0.0655 | 0.0063 | 0.0098 | 0.0002 | -0.01 | 62.7 | 1.5 |
| A64_Zm-21 | 10.1 | 2430 | 311 | 0.13 | 0.0477 | 0.0034 | 0.0582 | 0.0038 | 0.0089 | 0.0002 | -0.09 | 56.9 | 1.3 |
| A64_Zm-22 | 17.8 | 430 | 111 | 0.26 | 0.0483 | 0.0066 | 0.0573 | 0.0079 | 0.0086 | 0.0003 | 0.13 | 54.9 | 2.0 |
| A64_Zm-23 | 14.6 | 286 | 167 | 0.59 | 0.0520 | 0.0110 | 0.0346 | 0.0065 | 0.0051 | 0.0002 | -0.29 | 32.5 | 1.5 |
| A64_Zm-24 | 4.3 | 82 | 15 | 0.19 | 0.0530 | 0.0200 | 0.0450 | 0.0150 | 0.0058 | 0.0005 | -0.10 | 37.1 | 3.1 |
| A64_Zm-25 | 6.4 | 447 | 12 | 0.03 | 0.0489 | 0.0065 | 0.0516 | 0.0066 | 0.0077 | 0.0003 | -0.08 | 49.6 | 1.8 |
| A64_Zm-26 | 6.3 | 1146 | 84 | 0.07 | 0.0462 | 0.0050 | 0.0305 | 0.0030 | 0.0048 | 0.0001 | 0.05 | 31.1 | 0.7 |
| A64_Zm-27 | 9.2 | 902 | 433 | 0.48 | 0.0475 | 0.0032 | 0.1217 | 0.0079 | 0.0186 | 0.0004 | 0.29 | 118.6 | 2.4 |
| A64_Zm-28 | 4.9 | 855 | 28 | 0.03 | 0.0467 | 0.0056 | 0.0469 | 0.0057 | 0.0073 | 0.0003 | 0.24 | 46.7 | 1.7 |
| A64_Zm-29 | 8.0 | 1570 | 910 | 0.58 | 0.0476 | 0.0039 | 0.0486 | 0.0038 | 0.0074 | 0.0002 | -0.01 | 47.2 | 1.0 |
| A64_Zm-30 | 13.9 | 103 | 59 | 0.58 | 0.0630 | 0.0210 | 0.0520 | 0.0150 | 0.0058 | 0.0004 | -0.02 | 37.5 | 2.7 |
| A64_Zm-31 | 8.9 | 210 | 113 | 0.54 | 0.0470 | 0.0110 | 0.0353 | 0.0081 | 0.0051 | 0.0002 | 0.20 | 32.7 | 1.5 |
| A64_Zm-32 | 4.1 | 3270 | 543 | 0.17 | 0.0497 | 0.0035 | 0.0461 | 0.0032 | 0.0068 | 0.0001 | 0.06 | 43.8 | 0.9 |
| A64_Zm-33 | 4.3 | 184 | 98 | 0.53 | 0.0500 | 0.0110 | 0.0430 | 0.0097 | 0.0066 | 0.0003 | -0.35 | 42.6 | 1.7 |
| A64_Zm-34 | 5.4 | 239 | 18 | 0.08 | 0.0592 | 0.0100 | 0.0434 | 0.0073 | 0.0051 | 0.0003 | 0.18 | 32.6 | 1.8 |
| A64_Zm-35 | 4.6 | 785 | 37 | 0.05 | 0.0512 | 0.0044 | 0.0564 | 0.0045 | 0.0080 | 0.0002 | -0.16 | 51.6 | 1.3 |
| A64_Zm-36 | 4.8 | 796 | 39 | 0.05 | 0.0497 | 0.0047 | 0.1190 | 0.0093 | 0.0176 | 0.0008 | 0.21 | 112.5 | 5.1 |
| A64_Zm-37 | 9.1 | 518 | 198 | 0.38 | 0.0506 | 0.0042 | 0.1413 | 0.0110 | 0.0205 | 0.0005 | -0.05 | 131.0 | 3.0 |
| A64_Zm_01 | 8.4 | 1206 | 666 | 0.55 | 0.0484 | 0.0041 | 0.1311 | 0.0099 | 0.0193 | 0.0005 | 0.19 | 123.4 | 3.1 |
| A64_Zm_02 | 4.6 | 693 | 324 | 0.47 | 0.0486 | 0.0043 | 0.1333 | 0.0100 | 0.0199 | 0.0004 | -0.42 | 127.0 | 2.7 |
| A64_Zm_06 | 10.9 | 1114 | 686 | 0.62 | 0.0484 | 0.0034 | 0.1293 | 0.0082 | 0.0198 | 0.0003 | 0.08 | 126.6 | 2.0 |

| Apparent ages (Ma) | | | | | | |
|---|---|---|---|---|---|---|
| $^{207}Pb/^{235}U$ | ±2s | $^{207}Pb/^{206}P$ | ±2s | Best age (Ma) | ±2s | Disc % |
| | | | | | | |
| 56.0 | 4.2 | 160.0 | 150.0 | 54.2 | 1.9 | 3.2 |
| 65.0 | 4.2 | 120.0 | 160.0 | 64.6 | 2.1 | 0.6 |
| 66.3 | 4.2 | 120.0 | 140.0 | 64.3 | 1.9 | 3.0 |
| 58.9 | 4.5 | 30.0 | 160.0 | 60.6 | 2.1 | -2.9 |
| 54.1 | 3.2 | 70.0 | 140.0 | 54.5 | 1.6 | -0.7 |
| 80.6 | 4.3 | 450.0 | 120.0 | 67.5 | 1.8 | 16.3 |
| 66.8 | 4.9 | 90.0 | 160.0 | 64.9 | 2.0 | 2.8 |
| 64.5 | 4.8 | 70.0 | 170.0 | 64.0 | 2.0 | 0.8 |
| 64.6 | 4.5 | 150.0 | 140.0 | 63.0 | 1.9 | 2.5 |
| 62.5 | 4.5 | 60.0 | 180.0 | 61.6 | 1.8 | 1.4 |
| 39.1 | 5.2 | 370.0 | 220.0 | 33.4 | 2.3 | 14.6 |
| 36.4 | 4.6 | 360.0 | 230.0 | 31.2 | 1.4 | 14.3 |
| 58.7 | 6.5 | 120.0 | 170.0 | 57.7 | 3.5 | 1.7 |
| 58.2 | 7.1 | 200.0 | 180.0 | 54.7 | 3.6 | 6.0 |
| 61.4 | 8.4 | 260.0 | 170.0 | 59.0 | 4.2 | 3.9 |
| 60.0 | 6.4 | 88.0 | 160.0 | 60.1 | 3.7 | -0.2 |
| 58.8 | 6.2 | 94.0 | 150.0 | 58.5 | 3.6 | 0.5 |
| 48.0 | 5.3 | 170.0 | 180.0 | 46.7 | 3.0 | 2.7 |
| 62.0 | 6.9 | 190.0 | 160.0 | 59.5 | 3.7 | 4.0 |
| 69.6 | 8.0 | 350.0 | 150.0 | 61.1 | 3.8 | 12.2 |
| 60.0 | 6.7 | 130.0 | 160.0 | 58.2 | 3.7 | 3.0 |
| | | | | | | |
| 45.2 | 4.6 | 760.0 | 180.0 | 33.9 | 1.9 | 25.0 |
| 41.8 | 5.0 | 200.0 | 220.0 | 38.4 | 2.2 | 8.1 |
| 51.4 | 4.1 | 200.0 | 180.0 | 48.0 | 1.8 | 6.6 |
| 59.1 | 3.9 | 220.0 | 160.0 | 56.7 | 1.7 | 4.1 |
| 31.4 | 8.0 | 210.0 | 540.0 | 24.8 | 2.0 | 21.0 |
| 49.9 | 2.9 | 80.0 | 140.0 | 49.3 | 1.7 | 1.2 |
| 41.2 | 14.0 | 310.0 | 390.0 | 36.9 | 2.5 | 10.4 |
| 35.7 | 4.2 | 150.0 | 260.0 | 33.7 | 1.6 | 5.6 |
| 31.4 | 6.1 | 270.0 | 380.0 | 27.1 | 1.4 | 13.7 |
| 52.9 | 4.5 | 300.0 | 180.0 | 49.4 | 1.9 | 6.6 |
| 35.0 | 7.0 | 420.0 | 340.0 | 29.2 | 1.4 | 16.6 |
| 52.7 | 3.2 | 100.0 | 150.0 | 52.4 | 1.8 | 0.6 |
| 51.7 | 2.8 | -30.0 | 120.0 | 53.1 | 1.5 | -2.7 |
| 54.6 | 2.8 | 90.0 | 120.0 | 53.3 | 1.6 | 2.4 |
| 58.1 | 3.7 | 50.0 | 140.0 | 58.7 | 1.8 | -1.0 |
| 42.1 | 4.1 | 280.0 | 180.0 | 39.8 | 2.1 | 5.5 |
| 110.7 | 5.5 | 220.0 | 120.0 | 105.9 | 3.1 | 4.3 |
| 58.1 | 5.8 | 230.0 | 180.0 | 52.3 | 2.8 | 10.0 |
| 112.0 | 8.5 | 240.0 | 160.0 | 106.7 | 6.6 | 4.7 |
| 32.5 | 6.1 | 90.0 | 320.0 | 31.3 | 1.5 | 3.7 |
| 82.4 | 5.5 | 100.0 | 160.0 | 82.8 | 2.6 | -0.5 |
| 34.2 | 4.1 | 0.0 | 180.0 | 34.9 | 2.6 | -2.0 |
| 101.0 | 8.5 | 170.0 | 170.0 | 101.3 | 6.3 | -0.3 |
| 29.8 | 7.5 | 160.0 | 470.0 | 25.9 | 2.2 | 13.1 |
| 54.8 | 3.2 | 80.0 | 120.0 | 54.1 | 1.6 | 1.2 |
| 65.3 | 8.1 | 50.0 | 200.0 | 63.8 | 5.7 | 2.3 |
| 66.6 | 7.0 | 140.0 | 170.0 | 62.8 | 5.5 | 5.7 |
| 55.5 | 5.2 | 80.0 | 200.0 | 55.5 | 2.0 | 0.0 |
| 31.4 | 4.3 | 200.0 | 260.0 | 26.7 | 1.2 | 15.0 |
| 28.1 | 3.5 | 80.0 | 240.0 | 28.1 | 1.2 | 0.0 |
| 30.7 | 4.5 | 150.0 | 280.0 | 27.8 | 1.3 | 9.4 |
| 53.9 | 3.0 | 10.0 | 120.0 | 55.4 | 1.9 | -2.8 |
| 38.0 | 4.4 | 70.0 | 180.0 | 38.6 | 2.4 | -1.6 |
| 25.9 | 3.6 | 20.0 | 280.0 | 25.2 | 1.1 | 2.8 |
| 61.4 | 4.1 | 80.0 | 140.0 | 60.6 | 1.9 | 1.3 |
| 55.1 | 4.7 | 160.0 | 160.0 | 54.2 | 2.1 | 1.6 |
| 38.5 | 6.4 | 270.0 | 220.0 | 35.9 | 3.1 | 6.8 |
| 126.0 | 12.0 | 80.0 | 200.0 | 125.3 | 4.4 | 0.6 |
| 67.6 | 7.4 | 90.0 | 150.0 | 67.7 | 6.8 | -0.1 |
| 121.9 | 9.1 | 200.0 | 170.0 | 120.5 | 4.7 | 1.1 |
| 65.9 | 3.9 | 90.0 | 130.0 | 64.4 | 2.3 | 2.3 |
| 115.9 | 5.8 | 189.0 | 120.0 | 112.4 | 3.5 | 3.0 |
| 46.2 | 3.9 | 620.0 | 180.0 | 36.3 | 1.4 | 21.4 |
| 36.8 | 5.0 | 290.0 | 260.0 | 34.1 | 1.8 | 7.3 |
| 34.1 | 3.8 | 30.0 | 220.0 | 32.0 | 1.3 | 6.2 |
| 34.9 | 4.7 | 170.0 | 220.0 | 32.2 | 1.3 | 7.7 |
| 46.4 | 4.8 | 50.0 | 170.0 | 46.6 | 3.2 | -0.4 |
| 60.3 | 4.1 | 90.0 | 150.0 | 59.7 | 1.8 | 1.0 |

| | | | | | | |
|---|---|---|---|---|---|---|
| 56.4 | 3.7 | 30.0 | 140.0 | 57.8 | 1.2 | -2.4 |
| 61.3 | 4.0 | 150.0 | 140.0 | 59.8 | 1.4 | 2.4 |
| 27.1 | 4.3 | 110.0 | 320.0 | 27.0 | 1.1 | 0.4 |
| 30.1 | 4.4 | 450.0 | 280.0 | 25.8 | 1.0 | 14.3 |
| 27.1 | 5.4 | 100.0 | 370.0 | 25.6 | 1.2 | 5.5 |
| 29.4 | 4.8 | 160.0 | 290.0 | 25.9 | 1.1 | 11.9 |
| 28.1 | 5.7 | 100.0 | 370.0 | 26.1 | 0.9 | 7.0 |
| 60.8 | 5.6 | 120.0 | 190.0 | 59.6 | 3.7 | 2.0 |
| 29.4 | 6.6 | 0.0 | 370.0 | 26.8 | 1.0 | 8.8 |
| 59.2 | 3.7 | -10.0 | 140.0 | 62.2 | 1.2 | -5.1 |
| 61.9 | 4.3 | 130.0 | 150.0 | 61.7 | 1.3 | 0.3 |
| 31.9 | 5.4 | 350.0 | 380.0 | 26.2 | 1.0 | 17.9 |
| 26.7 | 5.8 | -70.0 | 310.0 | 27.3 | 2.2 | -2.2 |
| 31.2 | 5.5 | 400.0 | 310.0 | 26.4 | 1.0 | 15.4 |
| 28.4 | 4.8 | 70.0 | 340.0 | 27.3 | 1.0 | 3.9 |
| 30.5 | 5.7 | 310.0 | 340.0 | 26.6 | 0.9 | 12.7 |
| 28.5 | 4.3 | 150.0 | 320.0 | 26.3 | 1.1 | 7.7 |
| 29.5 | 6.0 | 350.0 | 350.0 | 26.5 | 2.4 | 10.2 |
| 29.4 | 4.9 | 120.0 | 330.0 | 26.9 | 1.0 | 8.4 |
| 26.9 | 4.0 | 140.0 | 320.0 | 25.9 | 0.9 | 3.8 |
| 31.7 | 6.3 | 280.0 | 330.0 | 26.5 | 1.1 | 16.4 |
| 27.6 | 4.0 | 150.0 | 300.0 | 26.2 | 1.1 | 5.0 |
| 32.7 | 7.7 | 240.0 | 330.0 | 28.8 | 2.9 | 11.9 |
| 30.2 | 5.2 | 290.0 | 320.0 | 26.5 | 1.1 | 12.3 |
| 31.3 | 5.4 | 250.0 | 340.0 | 27.2 | 1.4 | 13.1 |
| 26.5 | 3.2 | 90.0 | 200.0 | 25.3 | 0.7 | 4.5 |
| 32.4 | 7.3 | 260.0 | 250.0 | 29.2 | 3.0 | 9.9 |
| 31.3 | 5.7 | 260.0 | 300.0 | 26.0 | 1.5 | 17.0 |
| 31.2 | 4.0 | 240.0 | 280.0 | 26.6 | 0.9 | 14.7 |
| 66.4 | 5.4 | 390.0 | 150.0 | 62.6 | 3.5 | 5.7 |
| 60.6 | 7.0 | 250.0 | 130.0 | 58.4 | 2.2 | 3.6 |
| 69.4 | 8.3 | 300.0 | 120.0 | 63.7 | 2.6 | 8.2 |
| 68.3 | 7.5 | 377.0 | 96.0 | 64.0 | 1.8 | 6.3 |
| 62.1 | 5.5 | 215.0 | 73.0 | 61.6 | 1.4 | 0.8 |
| 65.0 | 13.0 | 550.0 | 170.0 | 64.0 | 2.7 | 1.5 |
| 78.1 | 7.1 | 407.0 | 62.0 | 72.5 | 2.3 | 7.2 |
| 66.6 | 8.5 | 934.0 | 97.0 | 60.2 | 2.1 | 9.6 |
| | | | | | | |
| 69.6 | 5.7 | 276.0 | 72.0 | 65.7 | 2.4 | 5.6 |
| 49.0 | 4.3 | 502.0 | 78.0 | 43.9 | 1.1 | 10.4 |
| 1033.0 | 38.0 | 1022.0 | 51.0 | 1023.0 | 18.0 | 1.0 |
| 47.9 | 4.6 | 550.0 | 130.0 | 45.4 | 1.3 | 5.2 |
| 73.2 | 8.2 | 353.0 | 76.0 | 65.8 | 2.1 | 10.1 |
| 64.0 | 8.6 | 650.0 | 120.0 | 58.4 | 2.2 | 8.8 |
| 54.7 | 4.9 | 351.0 | 64.0 | 50.6 | 1.1 | 7.5 |
| 58.7 | 8.2 | 520.0 | 150.0 | 59.5 | 2.7 | -1.4 |
| 67.6 | 9.8 | 560.0 | 130.0 | 62.6 | 3.2 | 7.4 |
| 65.2 | 10.0 | 690.0 | 200.0 | 60.7 | 2.5 | 6.9 |
| 63.0 | 14.0 | 560.0 | 210.0 | 61.1 | 4.6 | 3.0 |
| 67.8 | 9.6 | 730.0 | 140.0 | 58.5 | 2.8 | 13.7 |
| 81.6 | 4.9 | 252.0 | 57.0 | 79.5 | 1.6 | 2.6 |
| 55.8 | 7.6 | 500.0 | 210.0 | 59.2 | 2.9 | -6.1 |
| 162.0 | 17.0 | 395.0 | 90.0 | 154.9 | 7.5 | 4.4 |
| 55.4 | 7.8 | 440.0 | 130.0 | 53.2 | 2.5 | 4.0 |
| 57.4 | 7.4 | 570.0 | 140.0 | 63.6 | 2.1 | -10.8 |
| 49.0 | 4.1 | 454.0 | 100.0 | 44.9 | 1.3 | 8.4 |
| 60.2 | 8.8 | 610.0 | 140.0 | 59.6 | 2.6 | 1.0 |
| 2580.0 | 42.0 | 2629.0 | 30.0 | 2629.0 | 30.0 | 0.5 |
| 2684.0 | 38.0 | 2719.8 | 21.0 | 2719.8 | 21.0 | 1.8 |
| 620.0 | 24.0 | 760.0 | 58.0 | 599.8 | 11.0 | 3.3 |
| 61.4 | 7.7 | 470.0 | 120.0 | 62.2 | 2.0 | -1.3 |
| 67.8 | 6.8 | 520.0 | 110.0 | 62.7 | 1.9 | 7.5 |
| 67.9 | 4.4 | 268.0 | 78.0 | 67.6 | 1.5 | 0.4 |
| 59.8 | 5.5 | 319.0 | 79.0 | 59.5 | 2.0 | 0.5 |
| 37.8 | 3.0 | 395.0 | 79.0 | 36.0 | 1.0 | 4.7 |
| 62.1 | 7.6 | 173.0 | 81.0 | 65.2 | 3.6 | -5.0 |
| 67.2 | 8.1 | 420.0 | 110.0 | 61.4 | 2.5 | 8.6 |
| 62.0 | 10.0 | 430.0 | 110.0 | 67.3 | 3.8 | -8.5 |
| 64.0 | 11.0 | 680.0 | 170.0 | 60.7 | 2.7 | 5.2 |
| | | | | | | |
| 36.6 | 5.2 | 120.0 | 290.0 | 34.5 | 1.4 | 5.7 |
| 35.4 | 5.7 | 300.0 | 320.0 | 32.5 | 1.4 | 8.2 |
| 43.4 | 5.3 | 510.0 | 290.0 | 34.2 | 1.1 | 21.2 |

| | | | | | | |
|---|---|---|---|---|---|---|
| 34.8 | 5.5 | 110.0 | 280.0 | 32.0 | 1.3 | 8.0 |
| 41.0 | 5.4 | 410.0 | 280.0 | 33.6 | 1.1 | 18.1 |
| 38.2 | 7.0 | 370.0 | 340.0 | 34.4 | 1.4 | 9.9 |
| 44.8 | 9.0 | 320.0 | 390.0 | 36.4 | 1.6 | 18.8 |
| 33.2 | 7.4 | 40.0 | 360.0 | 32.0 | 1.5 | 3.6 |
| 41.8 | 6.2 | 230.0 | 300.0 | 35.9 | 1.2 | 14.1 |
| 36.1 | 18.0 | 320.0 | 450.0 | 33.4 | 2.1 | 7.5 |
| 44.0 | 20.0 | 390.0 | 600.0 | 35.7 | 2.7 | 18.9 |
| 77.0 | 15.0 | 70.0 | 370.0 | 73.7 | 3.7 | 4.3 |
| 61.7 | 4.6 | 80.0 | 170.0 | 61.7 | 1.7 | 0.0 |
| 33.1 | 7.3 | -180.0 | 400.0 | 34.1 | 1.5 | -3.0 |
| 39.3 | 5.2 | 570.0 | 270.0 | 30.7 | 1.1 | 21.9 |
| 45.8 | 5.9 | 750.0 | 260.0 | 32.7 | 0.9 | 28.6 |
| 33.2 | 3.8 | 10.0 | 230.0 | 33.5 | 0.9 | -0.8 |
| 36.0 | 9.6 | -250.0 | 470.0 | 35.5 | 1.9 | 1.4 |
| 41.6 | 4.5 | 370.0 | 230.0 | 34.7 | 1.1 | 16.6 |
| 47.0 | 15.0 | 230.0 | 590.0 | 37.0 | 2.3 | 21.3 |
| 40.0 | 13.0 | 240.0 | 570.0 | 33.9 | 2.9 | 15.3 |
| 35.1 | 6.7 | 150.0 | 340.0 | 36.4 | 1.6 | -3.7 |
| 35.8 | 4.9 | 260.0 | 260.0 | 31.9 | 1.1 | 10.9 |
| 42.6 | 6.5 | 380.0 | 320.0 | 34.7 | 1.3 | 18.5 |
| 37.5 | 8.7 | -60.0 | 430.0 | 36.1 | 2.2 | 3.7 |
| 98.9 | 8.8 | 210.0 | 200.0 | 93.5 | 3.7 | 5.5 |
| 39.9 | 6.9 | 150.0 | 350.0 | 34.1 | 1.4 | 14.5 |
| 34.4 | 4.8 | 240.0 | 260.0 | 33.1 | 1.2 | 3.8 |
| 37.2 | 5.8 | 240.0 | 310.0 | 34.4 | 1.1 | 7.5 |

| | | | | | | |
|---|---|---|---|---|---|---|
| 44.0 | 12.0 | 230.0 | 550.0 | 37.0 | 2.5 | 15.9 |
| 101.0 | 12.0 | 360.0 | 260.0 | 96.3 | 4.5 | 4.7 |
| 36.7 | 6.4 | 350.0 | 320.0 | 32.4 | 1.4 | 11.7 |
| 35.0 | 8.2 | 130.0 | 420.0 | 32.9 | 1.7 | 6.0 |
| 46.0 | 4.0 | 100.0 | 190.0 | 45.7 | 1.1 | 0.7 |
| 44.0 | 14.0 | 20.0 | 610.0 | 37.6 | 2.9 | 14.5 |
| 38.9 | 6.1 | 410.0 | 280.0 | 31.0 | 1.4 | 20.3 |
| 37.3 | 8.0 | 220.0 | 410.0 | 33.1 | 1.4 | 11.3 |
| 139.9 | 10.0 | 320.0 | 170.0 | 132.0 | 3.4 | 5.6 |
| 47.6 | 3.8 | 120.0 | 190.0 | 45.6 | 1.0 | 4.2 |
| 120.2 | 6.7 | 132.0 | 140.0 | 118.3 | 2.2 | 1.6 |
| 31.8 | 7.4 | -190.0 | 400.0 | 33.0 | 1.6 | -3.8 |
| 49.3 | 4.8 | 200.0 | 230.0 | 45.2 | 1.3 | 8.3 |
| 43.0 | 15.0 | -240.0 | 620.0 | 35.2 | 2.2 | 18.1 |
| 105.0 | 17.0 | 210.0 | 310.0 | 94.9 | 5.1 | 9.6 |
| 64.2 | 6.0 | 80.0 | 200.0 | 62.7 | 1.5 | 2.3 |
| 57.4 | 3.7 | 90.0 | 160.0 | 56.9 | 1.3 | 0.9 |
| 56.3 | 7.6 | 130.0 | 260.0 | 54.9 | 2.0 | 2.5 |
| 34.3 | 6.3 | 60.0 | 370.0 | 32.5 | 1.5 | 5.2 |
| 44.0 | 14.0 | 30.0 | 580.0 | 37.1 | 3.1 | 15.7 |
| 52.1 | 6.3 | 200.0 | 250.0 | 49.6 | 1.8 | 4.8 |
| 30.5 | 3.0 | 60.0 | 220.0 | 31.1 | 0.7 | -1.9 |
| 116.5 | 7.1 | 60.0 | 140.0 | 118.6 | 2.4 | -1.8 |
| 46.4 | 5.5 | 50.0 | 240.0 | 46.7 | 1.7 | -0.6 |
| 48.1 | 3.7 | 60.0 | 170.0 | 47.2 | 1.0 | 1.9 |
| 50.0 | 14.0 | 360.0 | 570.0 | 37.5 | 2.7 | 25.0 |
| 34.9 | 7.9 | -70.0 | 380.0 | 32.7 | 1.5 | 6.3 |
| 45.7 | 3.1 | 180.0 | 160.0 | 43.8 | 0.9 | 4.1 |
| 42.0 | 9.4 | 230.0 | 370.0 | 42.6 | 1.7 | -1.4 |
| 42.8 | 7.1 | 670.0 | 330.0 | 32.6 | 1.8 | 23.8 |
| 55.7 | 4.3 | 270.0 | 160.0 | 51.6 | 1.3 | 7.4 |
| 114.3 | 8.5 | 170.0 | 160.0 | 112.5 | 5.1 | 1.6 |
| 133.9 | 9.4 | 230.0 | 170.0 | 131.0 | 3.0 | 2.2 |
| 125.0 | 8.9 | 203.0 | 84.0 | 123.4 | 3.1 | 1.3 |
| 126.9 | 9.2 | 293.0 | 110.0 | 127.0 | 2.7 | -0.1 |
| 123.3 | 7.4 | 222.0 | 70.0 | 126.6 | 2.0 | -2.7 |